

University of Montana

ScholarWorks at University of Montana

Graduate Student Theses, Dissertations, &
Professional Papers

Graduate School

1997

Understanding anomalously large isotope effects dealing with hydrogen transfer reactions in transition metal chemistry

Kirk Robert Hash

The University of Montana

Follow this and additional works at: <https://scholarworks.umt.edu/etd>

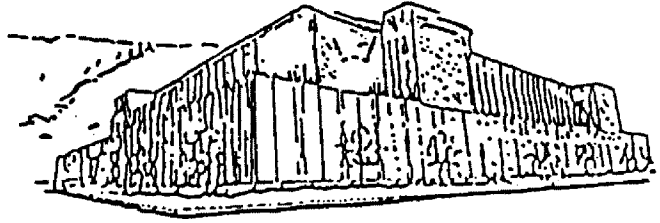
Let us know how access to this document benefits you.

Recommended Citation

Hash, Kirk Robert, "Understanding anomalously large isotope effects dealing with hydrogen transfer reactions in transition metal chemistry" (1997). *Graduate Student Theses, Dissertations, & Professional Papers*. 8224.

<https://scholarworks.umt.edu/etd/8224>

This Thesis is brought to you for free and open access by the Graduate School at ScholarWorks at University of Montana. It has been accepted for inclusion in Graduate Student Theses, Dissertations, & Professional Papers by an authorized administrator of ScholarWorks at University of Montana. For more information, please contact scholarworks@mso.umt.edu.



Maureen and Mike
MANSFIELD LIBRARY

The University of **MONTANA**

Permission is granted by the author to reproduce this material in its entirety,
provided that this material is used for scholarly purposes and is properly cited in
published works and reports.

*** Please check "Yes" or "No" and provide signature ***

Yes, I grant permission _____
No, I do not grant permission _____

Author's Signature Kirk Robert Haskins

Date 4/29/97

Any copying for commercial purposes or financial gain may be undertaken only with
the author's explicit consent.

UNDERSTANDING ANOMALOUSLY LARGE ISOTOPE EFFECTS
DEALING WITH HYDROGEN TRANSFER REACTIONS
IN TRANSITION METAL CHEMISTRY

by

Kirk Robert Hash, Sr.

B.S. , The University of Montana, 1990

Presented in partial fulfillment of the requirement

for the degree of

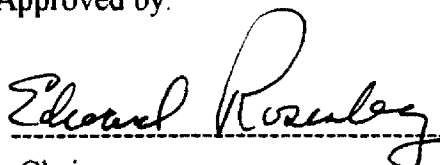
Master of Science

in Chemistry

The University of Montana

1997

Approved by:



Chairperson



Dean, Graduate School

5-1-97

Date

UMI Number: EP39025

All rights reserved

INFORMATION TO ALL USERS

The quality of this reproduction is dependent upon the quality of the copy submitted.

In the unlikely event that the author did not send a complete manuscript and there are missing pages, these will be noted. Also, if material had to be removed, a note will indicate the deletion.



UMI EP39025

Published by ProQuest LLC (2013). Copyright in the Dissertation held by the Author.


Microform Edition © ProQuest LLC.

All rights reserved. This work is protected against unauthorized copying under Title 17, United States Code



ProQuest LLC.
789 East Eisenhower Parkway
P.O. Box 1346
Ann Arbor, MI 48106 - 1346

Understanding Anomalously Large Isotope Effects Dealing with Hydrogen Transfer Reactions in Transition Metal Chemistry

Director: Edward Rosenberg 

Fluorine-19 NMR spectroscopy and UV-Vis spectrophotometry were used to investigate the kinetics and isotope effects observed in the reaction of $\text{H}_2\text{Os}_3(\text{CO})_{10}$ with trifluoroacetonitrile (CF_3CN). Two major goals were pursued. The first was to perform careful kinetic isotopic substitution experiments and to determine the origin of these large isotope effects which would assist in quantifying why such anomalously large isotope effects are observed. Second, to elucidate a plausible mechanism for this reaction which takes into account these anomalously large kinetic isotope effects.

Recent kinetic studies on the reaction of $(\mu\text{-H(D)})_2\text{Os}_3(\text{CO})_{10}$ and CF_3CN to form $(\mu\text{-H(D)})\text{Os}_3(\text{CO})_{10}(\mu\text{-NC(H(D)CF}_3))$ (**4**) and $\text{H(D)Os}_3(\text{CO})_{10}(\mu\text{-}\eta^2\text{-H(D)NCCF}_3)$ (**5**) are reported. Multiple isotopic experiments were conducted over a range of temperatures which provided data for determining isotope effects for this reaction and for constructing Arrhenius and Eyring kinetic plots. Increasing isotope effects at lower temperatures were observed in the formation of **5**, but remained fairly constant for **4**. The formation of the initial isomeric adduct $(\mu\text{-H(D)})\text{Os}_3(\text{H(D)})(\text{CF}_3\text{CN})$ was not directly observed but its formation was found to be the rate determining step for the reaction. Therefore, the rate constants for the hydrogen transfer step which occurs when the adduct decomposes into **4** and **5** could not be determined directly. Studies did reveal that the formation of **5** (protic case) is favored at decreasing temperatures whereas when deuterium is substituted for hydrogen the reaction slows down considerably. The formation of **4** is less favored at decreasing temperatures regardless of which analog (protic or deuterated) is used. These results provide information on determining a plausible mechanism for the reaction which provides an explanation to the observed isotope effects and supports the conclusion that a significant proton barrier tunneling component is associated with the formation of **4** and **5**.

Another proton transfer reaction studied was the protonation of $\text{Ru}_3(\text{CO})_{10}(\mu\text{-NO})^-$ (**1**) with $\text{CF}_3\text{CO}_2\text{X}$ and $\text{CF}_3\text{SO}_3\text{X}$ ($\text{X}=\text{H}$ or D) in the temperature range of -80 to 25°C using ^{13}C NMR techniques. The oxygen in the nitrosyl group was determined to be the kinetic site of protonation regardless of which acid was used, producing $\text{Ru}_3(\text{CO})_9(\mu_3\text{-CO})(\mu_3\text{-NOH(D)})$ (**2**). The proton being transferred to the metal core, producing $\text{Ru}_3(\text{CO})_{10}(\mu\text{-NO})(\mu\text{-H(D)})$ (**3**) for both the protic and deuterated species had approximately the same rate of transfer. The results tentatively conclude that the isotope effects are associated with an intramolecular hydrogen transfer rather than an anion assisted intermolecular process.

DEDICATION

To my wife, Lynn

and to my four children

Kirk Jr., Katherine, Michael, Christine

TABLE OF CONTENTS

ABSTRACT	ii
DEDICATION	iii
LIST OF TABLES	v
LIST OF FIGURES	vi
CHAPTER	
1. INTRODUCTION	1
2. RESULTS AND DISCUSSION	14
2.1 The reaction of $\text{H}_2\text{Os}_3(\text{CO})_{10}$ with trifluoroacetonitrile followed by ^{19}F NMR	14
2.2 Simplified mathematical treatment	29
2.3 The reaction of $\text{H}_2\text{Os}_3(\text{CO})_{10}$ with trifluoroacetonitrile followed by UV-Vis Spectroscopy	33
2.4 The reaction of $\text{PPN}[\text{Ru}_3(\text{CO})_{10}(\mu\text{-NO})]$, 1 , with $\text{CF}_3\text{SO}_3\text{X}$ and $\text{CF}_3\text{CO}_2\text{X}$ ($\text{X}=\text{H}$ or D) followed by ^{13}C NMR spectroscopy	38
3. CONCLUSIONS / FUTURE WORK	45
4. EXPERIMENTAL	49
REFERENCES	107

LIST OF TABLES

TABLE	PAGE
1. Protonations of transition metal complexes that exhibit large kinetic deuterium isotope effects	3
2. Rate constants and errors for the formation of 4 , (μ -H)Os ₃ (CO) ₁₀ (μ -NC(H)CF ₃) and 5 , (μ -H)Os ₃ (CO) ₁₀ (μ - η^2 -HNCCF ₃)	16
3. Average rate constants and Kinetic Deuterium Isotope Effects for the formation of 4 , (μ -H)Os ₃ (CO) ₁₀ (μ -NC(H)CF ₃) and 5 , (μ -H)Os ₃ (CO) ₁₀ (μ - η^2 -HNCCF ₃)	17
4. Average product ratios and Kinetic Deuterium Isotope Effects for the formation of 4 , (μ -H)Os ₃ (CO) ₁₀ (μ -NC(H)CF ₃) and 5 , (μ -H)Os ₃ (CO) ₁₀ (μ - η^2 -HNCCF ₃)	19
5. Rate constants and errors measured by UV-Vis Spectroscopy for the formation of 4 , (μ -H)Os ₃ (CO) ₁₀ (μ -NC(H)CF ₃) and 5 , (μ -H)Os ₃ (CO) ₁₀ (μ - η^2 -HNCCF ₃)	33
6. Fluorine-19 NMR data for 4 , (μ -H)Os ₃ (CO) ₁₀ (μ -NC(H)CF ₃) and 5 , (μ -H)Os ₃ (CO) ₁₀ (μ - η^2 -HNCCF ₃)	55
7. ¹ H NMR data for 4 , (μ -H)Os ₃ (CO) ₁₀ (μ -NC(H)CF ₃) and 5 , (μ -H)Os ₃ (CO) ₁₀ (μ - η^2 -HNCCF ₃) and the starting complex, H ₂ Os ₃ (CO) ₁₀	55

LIST OF FIGURES

FIGURE	PAGE
1. ^{19}F NMR stack plot of the formation of 4 , ($\mu\text{-H}$) $\text{Os}_3(\text{CO})_{10}(\mu\text{-NC}(\text{H})\text{CF}_3)$ and 5 , ($\mu\text{-H}$) $\text{Os}_3(\text{CO})_{10}(\mu\text{-}\eta^2\text{-HNCCF}_3)$	15
2. ^{19}F NMR spectrum showing product ratios and integrated peak areas of 4 , ($\mu\text{-H}$) $\text{Os}_3(\text{CO})_{10}(\mu\text{-NC}(\text{H})\text{CF}_3)$ and 5 , ($\mu\text{-H}$) $\text{Os}_3(\text{CO})_{10}(\mu\text{-}\eta^2\text{-HNCCF}_3)$	18
3. ^1H NMR stack plot of the disappearance of reactant, $\text{H}_2\text{Os}_3(\text{CO})_{10}$ and the formation of 4 , ($\mu\text{-H}$) $\text{Os}_3(\text{CO})_{10}(\mu\text{-NC}(\text{H})\text{CF}_3)$ and 5 , ($\mu\text{-H}$) $\text{Os}_3(\text{CO})_{10}(\mu\text{-}\eta^2\text{-HNCCF}_3)$ with time at 25 °C	20
4. Arrhenius plot of the formation of 4 , ($\mu\text{-H}$) $\text{Os}_3(\text{CO})_{10}(\mu\text{-NC}(\text{H})\text{CF}_3)$	22
5. Arrhenius plot of the formation of 5 , ($\mu\text{-H}$) $\text{Os}_3(\text{CO})_{10}(\mu\text{-}\eta^2\text{-HNCCF}_3)$	23
6. Eyring plot of the formation of 4 , ($\mu\text{-H}$) $\text{Os}_3(\text{CO})_{10}(\mu\text{-NC}(\text{H})\text{CF}_3)$	25
7. Eyring plot of the formation of 5 , ($\mu\text{-H}$) $\text{Os}_3(\text{CO})_{10}(\mu\text{-}\eta^2\text{-HNCCF}_3)$	26
8. Arrhenius plots of product ratios obtained from ^{19}F NMR spectra	28
9. UV-Vis kinetic plot of the formation of both 4 and 5 with variable gas volumes	34
10. UV-Vis kinetic plot of rate constants versus volume of gas (CF_3CN) used	35
11. UV-Vis kinetic spectrum where two isosbestic points are evident, performed at 25 °C, and with 4 ml of gas (CF_3CN)	36

12.	VT- ¹³ C NMR spectra of 1 in CD ₂ Cl ₂ /CH ₂ Cl ₂ , focusing on the carbonyl region at 100MHz	38
13.	a) ¹³ C NMR spectrum of the carbonyls of 2 in CD ₂ Cl ₂ /CH ₂ Cl ₂ at -80°C and at 100 MHz (where 1 is protonated with 1 eq. CF ₃ SO ₃ H) b) ¹³ C NMR spectrum of 2 at 25°C c) ¹³ C NMR spectrum of 2 converted to 3 after the addition of 0.4 eq. of PPNCF ₃ CO ₂ at 25°C	41
14.	a) ¹³ C NMR spectrum of 1 after the addition of 1 eq. of CF ₃ CO ₂ H or CF ₃ CO ₂ D at -80°C. b) ¹³ C NMR spectrum of 1 after the addition of 1 eq. of CF ₃ CO ₂ H or CF ₃ CO ₂ D at -80°C which is heated to 10°C showing the partial conversion of 2 to 3	42
15.	Variable temperature ¹³ C NMR spectra of 1 after the addition of 0.3 eq. of CF ₃ CO ₂ H in CD ₂ Cl ₂ /CH ₂ Cl ₂ at 100 MHz	44
16.	Specially designed glassware to inject gas compounds into NMR tubes	51
17.	Kinetic plot of the formation of 4 , (μ-H)Os ₃ (CO) ₁₀ (μ-NC(H)CF ₃) at 55 °C	56
18.	Kinetic plot of the formation of 4 , (μ-H)Os ₃ (CO) ₁₀ (μ-NC(H)CF ₃) at 55 °C	57
19.	Kinetic plot of the formation of 5 , (μ-H)Os ₃ (CO) ₁₀ (μ-η ² -HNCCF ₃) at 55 °C	58
20.	Kinetic plot of the formation of 5 , (μ-H)Os ₃ (CO) ₁₀ (μ-η ² -HNCCF ₃) at 55 °C	59
21.	Kinetic plot of the formation of 4 , (μ-H)Os ₃ (CO) ₁₀ (μ-NC(H)CF ₃) at 40 °C	60
22.	Kinetic plot of the formation of 4 , (μ-H)Os ₃ (CO) ₁₀ (μ-NC(H)CF ₃) at 40 °C	61
23.	Kinetic plot of the formation of 5 , (μ-H)Os ₃ (CO) ₁₀ (μ-η ² -HNCCF ₃) at 40 °C	62

24. Kinetic plot of the formation of 5 , (μ -H)Os ₃ (CO) ₁₀ (μ - η^2 -HNCCF ₃) at 40 °C	63
25. Kinetic plot of the formation of 4 , (μ -H)Os ₃ (CO) ₁₀ (μ -NC(H)CF ₃) at 25 °C	64
26. Kinetic plot of the formation of 4 , (μ -H)Os ₃ (CO) ₁₀ (μ -NC(H)CF ₃) at 25 °C	65
27. Kinetic plot of the formation of 5 , (μ -H)Os ₃ (CO) ₁₀ (μ - η^2 -HNCCF ₃) at 25 °C	66
28. Kinetic plot of the formation of 5 , (μ -H)Os ₃ (CO) ₁₀ (μ - η^2 -HNCCF ₃) at 25 °C	67
29. Kinetic plot of the formation of 4 , (μ -H)Os ₃ (CO) ₁₀ (μ -NC(H)CF ₃) at 10 °C	68
30. Kinetic plot of the formation of 4 , (μ -H)Os ₃ (CO) ₁₀ (μ -NC(H)CF ₃) at 10 °C	69
31. Kinetic plot of the formation of 5 , (μ -H)Os ₃ (CO) ₁₀ (μ - η^2 -HNCCF ₃) at 10 °C	70
32. Kinetic plot of the formation of 5 , (μ -H)Os ₃ (CO) ₁₀ (μ - η^2 -HNCCF ₃) at 10 °C	71
33. Kinetic plot of the formation of 4 , (μ -H)Os ₃ (CO) ₁₀ (μ -NC(H)CF ₃) at -5 °C	72
34. Kinetic plot of the formation of 4 , (μ -H)Os ₃ (CO) ₁₀ (μ -NC(H)CF ₃) at -5 °C	73
35. Kinetic plot of the formation of 5 , (μ -H)Os ₃ (CO) ₁₀ (μ - η^2 -HNCCF ₃) at -5 °C	74
36. Kinetic plot of the formation of 5 , (μ -H)Os ₃ (CO) ₁₀ (μ - η^2 -HNCCF ₃) at -5 °C	75

37.	Kinetic plot of the formation of 4 , (μ -H)Os ₃ (CO) ₁₀ (μ -NC(H)CF ₃) at -20 °C	76
38.	Kinetic plot of the formation of 4 , (μ -H)Os ₃ (CO) ₁₀ (μ -NC(H)CF ₃) at -20 °C	77
39.	Kinetic plot of the formation of 5 , (μ -H)Os ₃ (CO) ₁₀ (μ - η^2 -HNCCF ₃) at -20 °C	78
40.	Kinetic plot of the formation of 5 , (μ -H)Os ₃ (CO) ₁₀ (μ - η^2 -HNCCF ₃) at -20 °C	79
41.	Deuterated kinetic plot of the formation of 4 , (μ -D)Os ₃ (CO) ₁₀ (μ -NC(D)CF ₃) at 25 °C	80
42.	Deuterated kinetic plot of the formation of 4 , (μ -D)Os ₃ (CO) ₁₀ (μ -NC(D)CF ₃) at 25 °C	81
43.	Deuterated kinetic plot of the formation of 5 , (μ -D)Os ₃ (CO) ₁₀ (μ - η^2 -DNCCF ₃) at 25 °C	82
44.	Deuterated kinetic plot of the formation of 5 , (μ -D)Os ₃ (CO) ₁₀ (μ - η^2 -DNCCF ₃) at 25 °C	83
45.	Deuterated kinetic plot of the formation of 4 , (μ -D)Os ₃ (CO) ₁₀ (μ -NC(D)CF ₃) at 10 °C	84
46.	Deuterated kinetic plot of the formation of 4 , (μ -D)Os ₃ (CO) ₁₀ (μ -NC(D)CF ₃) at 10 °C	85
47.	Deuterated kinetic plot of the formation of 5 , (μ -D)Os ₃ (CO) ₁₀ (μ - η^2 -DNCCF ₃) at 10 °C	86
48.	Deuterated kinetic plot of the formation of 5 , (μ -D)Os ₃ (CO) ₁₀ (μ - η^2 -DNCCF ₃) at 10 °C	87
49.	Deuterated kinetic plot of the formation of 4 , (μ -D)Os ₃ (CO) ₁₀ (μ -NC(D)CF ₃) at -5 °C	88
50.	Deuterated kinetic plot of the formation of 4 , (μ -D)Os ₃ (CO) ₁₀ (μ -NC(D)CF ₃) at -5 °C	89

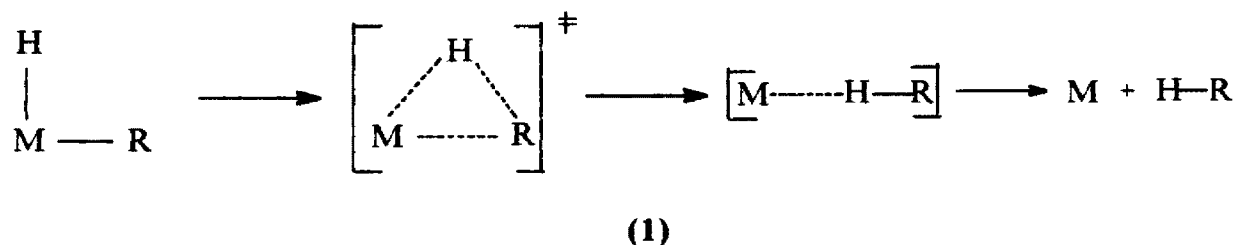
51. Deuterated kinetic plot of the formation of 5 , (μ -D)Os ₃ (CO) ₁₀ (μ - η^2 -DNCCF ₃) at -5 °C	90
52. Deuterated kinetic plot of the formation of 5 , (μ -D)Os ₃ (CO) ₁₀ (μ - η^2 -DNCCF ₃) at -5 °C	91
53. Deuterated kinetic plot of the formation of 4 , (μ -D)Os ₃ (CO) ₁₀ (μ -NC(D)CF ₃) at -20 °C	92
54. Deuterated kinetic plot of the formation of 4 , (μ -D)Os ₃ (CO) ₁₀ (μ -NC(D)CF ₃) at -20 °C	93
55. Deuterated kinetic plot of the formation of 5 , (μ -D)Os ₃ (CO) ₁₀ (μ - η^2 -DNCCF ₃) at -20 °C	94
56. Deuterated kinetic plot of the formation of 5 , (μ -D)Os ₃ (CO) ₁₀ (μ - η^2 -DNCCF ₃) at -20 °C	95
57. ¹ H kinetic plot of the disappearance of the starting material, H ₂ Os ₃ (CO) ₁₀ at 25 °C	96
58. ¹ H kinetic plot of the disappearance of the starting material, H ₂ Os ₃ (CO) ₁₀ at 25 °C	97
59. UV-Vis kinetic plot of the disappearance of the starting material, H ₂ Os ₃ (CO) ₁₀ , at 25 °C, and 552 nm., with 4 ml of gas (CF ₃ CN)	98
60. UV-Vis kinetic plot of the formation of 4 , (μ -H)Os ₃ (CO) ₁₀ (μ -NC(H)CF ₃) and 5 , (μ -H)Os ₃ (CO) ₁₀ (μ - η^2 -HNCCF ₃) at 25 °C, and 390 nm., with 4 ml of gas (CF ₃ CN)	99
61. UV-Vis kinetic plot of the formation of 4 , (μ -H)Os ₃ (CO) ₁₀ (μ -NC(H)CF ₃) and 5 , (μ -H)Os ₃ (CO) ₁₀ (μ - η^2 -HNCCF ₃) at 25 °C, and 392 nm., with 10 ml of gas (CF ₃ CN)	100
62. UV-Vis kinetic plot of the formation of 4 , (μ -H)Os ₃ (CO) ₁₀ (μ -NC(H)CF ₃) and 5 , (μ -H)Os ₃ (CO) ₁₀ (μ - η^2 -HNCCF ₃) at 25 °C, and 392 nm., with 1 ml of gas (CF ₃ CN)	101

63. UV-Vis kinetic plot of the formation of **4**, $(\mu\text{-H})\text{Os}_3(\text{CO})_{10}$
 $(\mu\text{-NC(H)CF}_3)$ and **5**, $(\mu\text{-H})\text{Os}_3(\text{CO})_{10}(\mu\text{-}\eta^2\text{-HNCCF}_3)$
 at 25 °C, and 392 nm., with 8 ml of gas (CF_3CN) 102
64. UV-Vis kinetic plot of the formation of **4**, $(\mu\text{-H})\text{Os}_3(\text{CO})_{10}$
 $(\mu\text{-NC(H)CF}_3)$ and **5**, $(\mu\text{-H})\text{Os}_3(\text{CO})_{10}(\mu\text{-}\eta^2\text{-HNCCF}_3)$
 at 25 °C, and 390 nm., with 1 ml of gas (CF_3CN) 103
65. UV-Vis kinetic plot of the formation of **4**, $(\mu\text{-H})\text{Os}_3(\text{CO})_{10}$
 $(\mu\text{-NC(H)CF}_3)$ and **5**, $(\mu\text{-H})\text{Os}_3(\text{CO})_{10}(\mu\text{-}\eta^2\text{-HNCCF}_3)$
 at 25 °C, and 392 nm., with 6 ml of gas (CF_3CN) 104
66. UV-Vis kinetic plot of the formation of **4**, $(\mu\text{-H})\text{Os}_3(\text{CO})_{10}$
 $(\mu\text{-NC(H)CF}_3)$ and **5**, $(\mu\text{-H})\text{Os}_3(\text{CO})_{10}(\mu\text{-}\eta^2\text{-HNCCF}_3)$
 at 25 °C, and 392 nm., with 10 ml of gas (CF_3CN) 105
67. UV-Vis kinetic plot of the formation of **4**, $(\mu\text{-H})\text{Os}_3(\text{CO})_{10}$
 $(\mu\text{-NC(H)CF}_3)$ and **5**, $(\mu\text{-H})\text{Os}_3(\text{CO})_{10}(\mu\text{-}\eta^2\text{-HNCCF}_3)$
 at 25 °C, and 390 nm., with 6 ml of gas (CF_3CN) 106

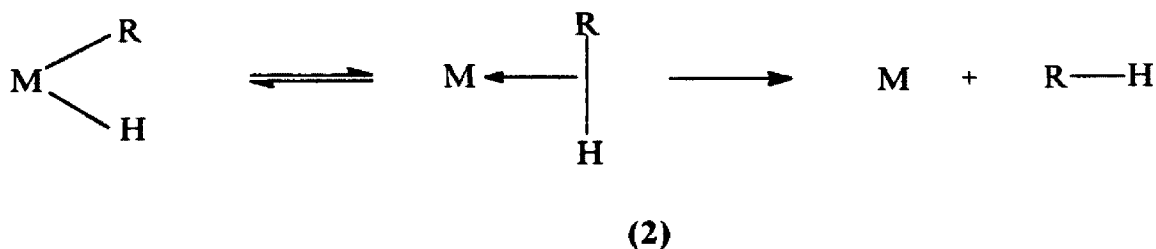
CHAPTER 1

INTRODUCTION

Every important catalytic process has a key step, and in most cases this step involves a metal-to-ligand or ligand-to-metal hydrogen transfer.¹⁻³ The significance of these transfers has opened an active area of research in recent years in trying to understand the mechanism by which hydrogen transfer takes place. Researchers have proposed that more than one mechanism could be responsible when a hydrogen transfer has occurred.⁴⁻¹⁶ These different mechanistic routes are often very close in energy. Therefore, small deviations in reaction conditions or in the electronic or steric properties of the reactants could result in favoring one mechanistic pathway over another pathway or a complete change in product distribution.^{16,17} The activation of carbon-hydrogen bonds provide an excellent example of the different pathways hydrogen transfers can occur. Two different reaction intermediates have been proposed and in some cases characterized. The first intermediate proposed was the metal-hydrogen-carbon agostic interaction (eq. 1).^{9-12,18-20}



The second intermediate is the carbon-hydrogen sigma bond complex (eq. 2).¹⁴



Studies involving both monometallic and polymetallic complexes have led to the identification of ground state agostic interactions.⁹⁻¹² Kinetic studies have provided substantial evidence that reveal the existence of the C-H sigma bond complex in the

thermal elimination of methane.¹⁴ However, hydrogen transfers involving oxygen or nitrogen metal bound ligands and their associated transition states or intermediates have not been isolated readily but are believed to have intermediates or transition states where the hydrogen behaves more like a proton.²¹

In both organic chemistry and organometallic chemistry, the determination of a reaction's mechanism and its rate determining step have been elucidated by kinetic deuterium isotope effects (KDIE).²²⁻²⁷ Generally, the KDIE observed in organometallic chemistry exhibit no abnormalities. For instance, reactions assumed to have linear, symmetrical transition states, illustrated by the proton exchange between $(n\text{-C}_5\text{H}_5)\text{Mo}(\text{CO})_3\text{H}$ and $(n\text{-C}_5\text{H}_5)\text{Mo}(\text{CO})_3^-$, the KDIE²⁸ agrees totally with the calculated KDIE obtained from the Bigeleisen equation (eq. 3).²⁹ This is also a common occurrence in proton exchange between organic acids and their conjugated bases.³⁰

$$\frac{k_{\text{H}}}{k_{\text{D}}} = \frac{hc}{\exp(2kt)} (v_{\text{H}} - v_{\text{D}})$$

(3)

The Bigeleisen equation (eq. 3) yields an idealized, "maximum" isotope effect which corresponds to the difference in the zero point energies between the protic and deuterated species where the transition state energy for both are the same. Two other isotope effects have been documented, the first having either a bent or a linear unsymmetrical transition or where there is an early or late transition state. These types of transition states tend to decrease the isotope effect involving the hydrogen being transferred on and off the transition metal center.²⁶ Another isotope effect encountered is what is referred to as an inverse isotope effect where the metal deuteride appears to react faster than the metal hydride. This effect arises from a larger difference between C-H and C-D stretching

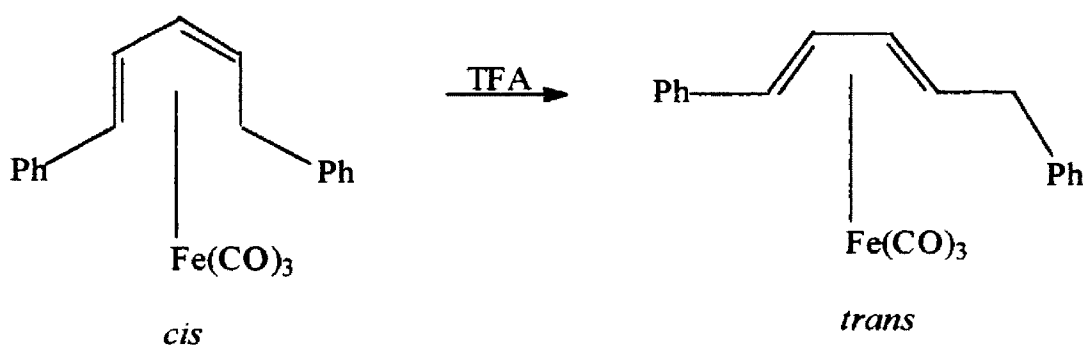
frequencies relative to the M-H and M-D stretching frequencies, which results in a shift in the equilibrium constant.³¹⁻³³ Recently, another inverse isotope effect has been reported where there is a very late transition state involving an irreversible hydrogen transfer in a metal-to-ligand or ligand-to-metal hydrogen transfer.^{34,35}

Generally, the KDIE observed is in the range predicted from the Bigeleisen equation (eq. 3), but many investigators have observed isotope effects that were much larger than the calculated ones. Unusually large KDIE's were first reported in the early 1970's involving transition metal reactions and were associated with the protonation of transition metal centers.³⁶⁻³⁸ Mays *et al.* studied the protonation of many different anionic and neutral transition metal complexes, and found KDIE's ranging from 7 to 17 where the predicted KDIE for the cleavage of an OH bond should be ~10 at 25 °C (Table 1).^{36,37}

Table 1: ^{36,37} Protonations of transition metal complexes that exhibit large kinetic deuterium isotope effects.

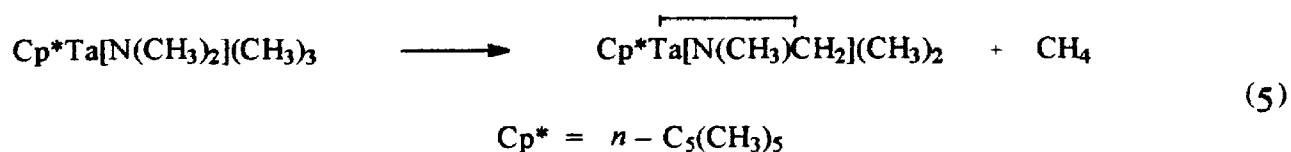
Compound	$k_H \setminus k_D$
$\text{FeCo}(\text{CO})_{12}^-$	16.8 ± 1.0
$\text{RuCo}_3(\text{CO})_{12}^-$	15.4 ± 1.0
$\text{OsCo}_3(\text{CO})_{12}^-$	16.2 ± 1.0
$\text{Os}_3(\text{CO})_{12}$	11 ± 2
$[(\eta\text{-C}_5\text{H}_5)\text{Fe}(\text{CO})_2]_2$	7 ± 1

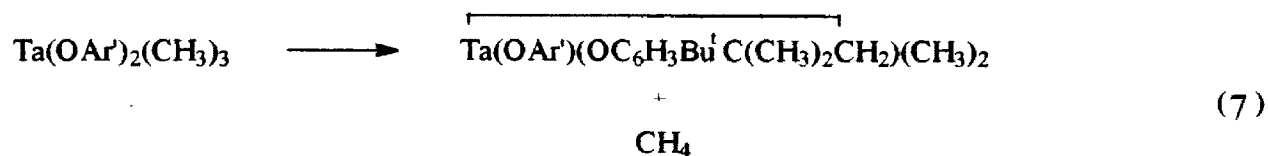
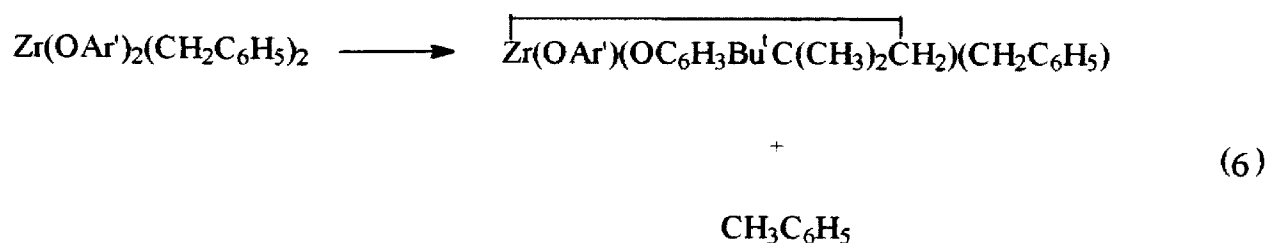
Another example of a very large isotope effect ($k_H/k_D = 27$) was reported by Whitesides and Nielen where acid catalyzed the *cis*-to-*trans* isomerization of the diene iron tricarbonyl compound (eq. 4).³⁸ No convincing reasons were suggested for these extremely large KDIE's at the time. Whitesides attributed these anomalously large isotope effects to the high O-H stretching frequency (3600 cm^{-1}) compared to the M-H stretching frequency ($1800\text{-}2000\text{ cm}^{-1}$) when a proton is transferred to the metal.³⁸



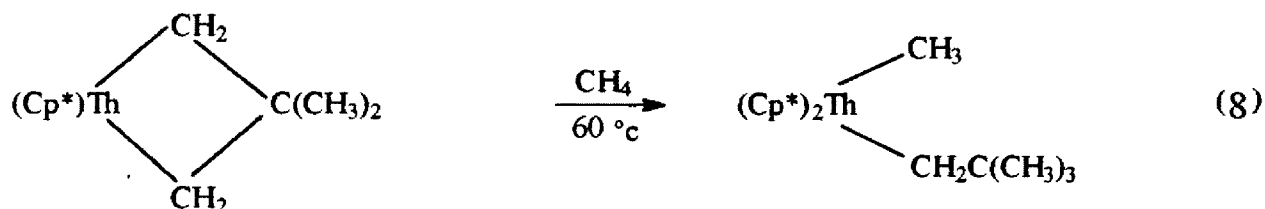
(4)

Other reactions having extremely large KDIE's compared with the calculated values via the Bigeleisen equation are observed in the activation of C-H bonds of various types of metal centers. By activating the C-H bond on the metal bound ligand or the reverse process the elimination of methane or some other type of hydrocarbon is observed (equations 5-8).³⁹⁻⁴¹





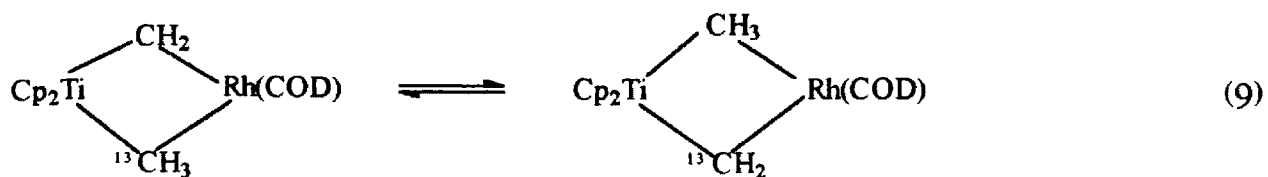
(OAr' = 2,6-di-*t*-butylphenoxide)



Equations 5 and 7 exhibit KDIE's 25 % larger than the calculated "maximum" isotope effects. However, equations 6 and 8 have isotope effects that are in the range of calculated values within experimental error. Since none of these systems are linear or exhibit a totally symmetrical transition state, the observed isotope effect should be considered anomalously large.^{22-26,29}

These anomalously large KDIE's have been observed and documented in both organic and transition metal chemistry.⁴²⁻⁴⁵ These reactions usually exhibit similar ground state geometries for reactant and product and have relatively low activation energies.⁴² If the potential barrier width is narrow and on the same scale as the de Broglie wavelength of the hydrogen being transferred then there is a finite probability that the hydrogen can tunnel

through the barrier or be on either sides of the barrier.⁴²⁻⁴⁷ The basis for proton barrier tunneling and the criteria for determining if tunneling has occurred is documented in organic chemistry.^{42,44} The first criterion is that the difference in activation energy between the protic and deuterated species, $\Delta E_{a_D^H}$, must be greater than the difference in zero point energies, $\Delta E_{o_D^H}$, which would give rise to an anomalously large KDIE.⁴²⁻⁴⁷ The second criterion is that the rate of the reaction becomes less temperature dependent at lower temperatures which results in the KDIE being very temperature dependent. This is illustrated by either an Arrhenius or Eyring plot where deviation from linearity is observed and the slope at this point becomes less negative indicating temperature independence.⁴⁷ The third criterion is associated with anomalously large preexponential factor ratio, A_D/A_H . Preexponential factor ratio should have a value of ~ 1 , a larger value should be considered anomalous. A large A_D/A_H ratio means that $A_D > A_H$ which conflicts with collision theory.⁴⁷ The preexponential factor, A , depends on the number of collisions and spatial orientation, therefore A_D should not be larger than A_H . Similarly, a large negative entropy of activation, ΔS^\ddagger , obtained from an Eyring kinetic plot is indicative of barrier tunneling.⁴²⁻⁴⁴ Such values occur when the reaction's barrier width is narrow which suggests very little change in the geometry of the reactant going to product resulting in a highly ordered transition state.⁴²⁻⁴⁴ Although many documented cases of proton barrier tunneling using the criteria stated above existed in the organic literature, very few existed in organometallic chemistry.²⁵ Therefore the origin of these large KDIE's in transition metal chemistry was not established until the late 1980's when Rosenberg *et. al.* began work in this area. Besides this work, there exists one documented case involving proton barrier tunneling in organometallic chemistry (eq. 9).⁴⁸

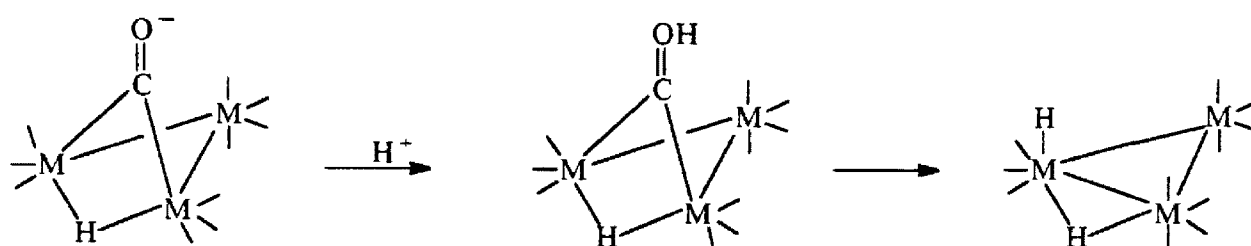


When this equilibrium reaction was studied, a KDIE of 24 at 45 °C was observed which suggests the possibility of tunneling (first criterion of tunneling). An Arrhenius plot showed deviation from linearity at the lower temperatures and an Eyring plot produced a large negative entropy of activation which suggests tunneling is involved. In this system's equilibrium state, the reactant and product geometries are identical, therefore the hydrogen transfer occurs reversibly between the two ligands.⁴⁸ To help explain how the hydrogen is being transferred, an agostic C-H-Ti interaction was proposed which lends credence to the observations made for equations 5-8.

Recent work by Norton *et.al.* reported the temperature dependence of the KDIE for intermolecular proton transfer from monometallic hydrides to nitrogen bases.⁴⁹ Even though an elegant theoretical treatment of the data was presented, experimental data did not meet the criteria for establishing a definitive tunneling mechanism.⁴⁹

We began our understanding of anomalously large KDIE's by investigating the large isotope effects observed by Mays *et al.* in the protonations of anionic clusters.³⁶⁻³⁷ Later, similar types of protonated systems were studied and reported by Shriver⁵⁰ and Keister⁵¹ that exhibited relevance and similarities to the earlier work of Mays. Shriver showed that the site of protonation for the polymetallic complex $(\mu\text{-H})(\mu\text{-CO})\text{Fe}_3(\text{CO})_{10}^-$ at -80 °C was at the oxygen of the bridging carbonyl which yields $(\mu\text{-H})(\mu\text{-COH})\text{Fe}_3(\text{CO})_{10}$. This species upon heating decomposes into $\text{Fe}_3(\text{CO})_{12}$ and hydrogen gas.⁵⁰ Keister reported a similar protonation occurring at -60 °C for the complex $(\mu\text{-H})(\mu\text{-CO})\text{Ru}_3(\text{CO})_{10}$ which produces a mixture of $(\mu\text{-H})(\mu\text{-COH})\text{Ru}_3(\text{CO})_{10}$ and the dihydride, $\text{H}(\mu\text{-H})\text{Ru}_3(\text{CO})_{11}$ which eventually converts only to the dihydride (eq. 10).⁵¹

Rosenberg *et. al.* hypothesized that because protonation occurred at the oxygen for these types of complexes and that the large KDIE's observed Mays³⁶⁻³⁷ may be the result of an intramolecular proton transfer. This conclusion seemed plausible since large isotope



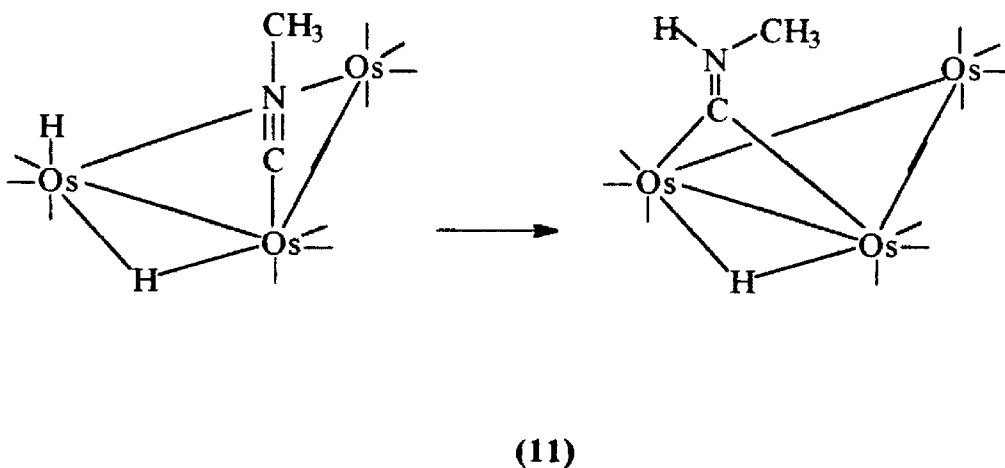
(M = Fe, Ru, Os)

(10)

effects are common in intramolecular proton transfer reactions.⁴¹⁻⁴³ Experiments were conducted using both protic and deuterated acids (FSO₃H and FSO₃D) to verify that proton transfer occurred intramolecularly and not intermolecularly. The reaction was monitored by ¹H NMR (-80 °C, 1 equiv. of FSO₃H, CD₂Cl₂) because protonation of the oxygen was rather slow. Experiments showed that under the same conditions the rate of protonation at the oxygen were the same regardless of which acid was used (FSO₃H or FSO₃D).⁵² The O-protonated complex converts to the dihydride in ~ 48 hours, whereas the O-deuterated complex showed no detectable conversion up to ~ 72 hours. Therefore, using the deuterated acid slows or nearly stops the deuteron from being transferred from oxygen to the metal center which supports our hypothesis. Another study was conducted using an osmium trimetallic cluster, (μ-H)(μ-CO)Os₃(CO)₁₀⁻ which gave similar results.⁵² Both studies provide qualitative support that the large isotope effects are associated with proton transfers from oxygen to the metal center in trimetallic cluster.

A reaction involving proton transfer occurring metal-to-ligand was studied which is just the opposite of the above mentioned reactions (eq. 10). This study should help to determine whether these large isotope effects are not thermodynamic in origin. The system chosen was the conversion of H(μ-H)Os₃(CNCH₃) to (μ-H)(μ-η¹-CH₃(H)NC)

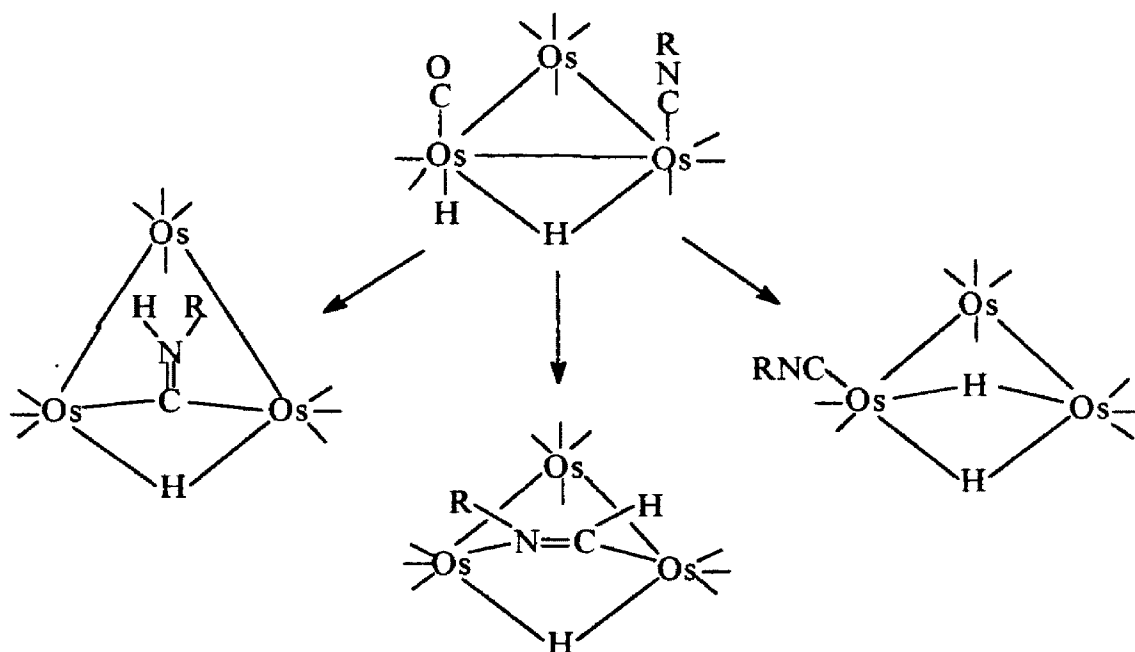
$\text{Os}_3(\text{CO})_{10}$ where the isocyanide adduct has the same geometry as $\text{H}(\mu\text{-H})\text{Os}_3(\text{CO})_{11}$ (eq. 11). Adams and Golembeski had previously studied this reaction and found that the hydrogen transfer occurred via an intermolecular-base catalyzed pathway.¹⁶ However,



when moisture is totally excluded from the system, the reaction proceeded via a much slower intramolecular pathway with an observed isotope effect of 26.9 at 32 °C.³³ Variable temperature kinetic studies (32 - 70 °C) were conducted which resulted in a difference in activation energy ($\Delta E_{\text{aD}}^{\text{H}}$) of 33.4 kJ/mole. This value is much greater than the calculated one involving zero point energies ($\Delta E_{\text{0D}}^{\text{H}}$) whose value was 3.3 kJ/mole.³³ Decreasing isotope effects were observed at higher temperatures or with the addition of base.³³ Another criterion for tunneling was verified when a large negative entropy of activation ($\Delta S_{\text{H}^\ddagger}$) value was observed for the protic reaction. The last criterion for tunneling was to observe a decrease in temperature dependence with decreasing temperature, that is, deviation from linearity at lower temperatures in Arrhenius and Eyring kinetic plots. This last criterion was never verified for the protic reaction, because the reaction was too slow below 10 °C. All these data are consistent with a mechanism involving proton barrier

tunneling.

To explore this tunneling phenomenon, several isocyanide complexes were studied (eq. 12).³³ Reactions using different isocyanide ligands were discovered to directly affect the products being formed.³³ Observations revealed that the type of products formed were dependent on both steric and electronic factors. The product distribution was also profoundly affected when deuterium was substituted for hydrogen.³³

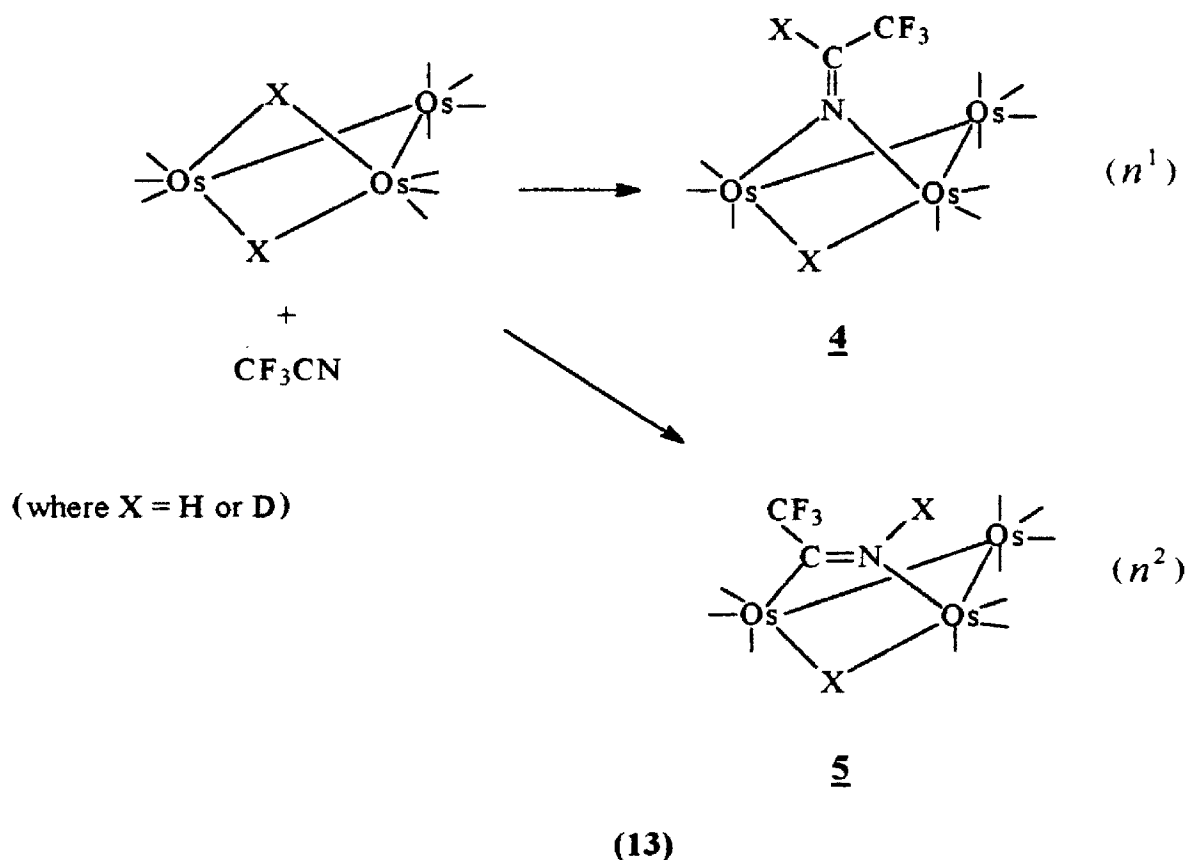


(12)

It was proposed that the dynamical processes within the cluster (axial-radial carbonyl or isocyanide exchange and bridge-terminal hydride exchange), control the intramolecular hydrogen transfers and dictate whether proton barrier tunneling will be observed.³³ These dynamic properties are responsible for making the reactant and product geometries similar, which narrows the barrier width and allows the proton to tunnel through the barrier. In addition, the activation energy for the dynamic processes is comparable to the

reaction's activation energy (~ 60 and ~ 80 kJ/mole, respectively). Therefore, these dynamic processes raise the reactant part way up the barrier, where the barrier is more narrow and tunneling is more likely.

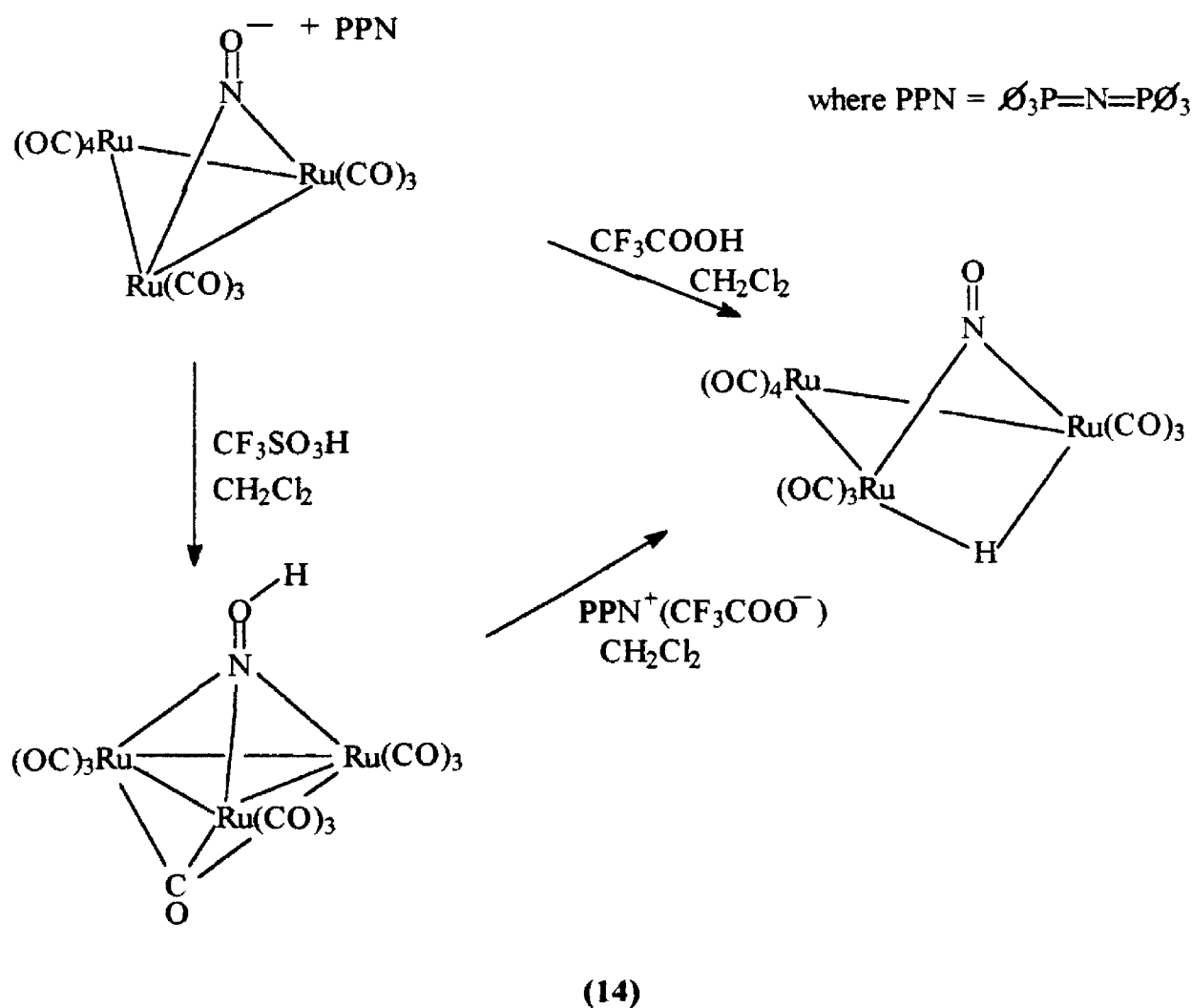
The goals of this thesis are to find the relationship between the structure of the transition metal carbonyl cluster and the magnitude of the KDIE. We also hope to define the relationship between the fluxionality of polynuclear complexes and its effect on proton barrier tunneling. A polynuclear complex where a metal-to-ligand proton transfer occurs was chosen to address these problems. The system studied is the reaction between $(\mu\text{-X})_2\text{Os}_3(\text{CO})_{10}$ ($\text{X}=\text{H}$ or D) and CF_3CN (eq. 13).^{53,54}



This reaction was chosen to determine whether large KDIE's can be attributed to either the nature of the hydrogen transfer (i.e., H^+ vs H^- transfer) or the geometry of the product being formed (i.e., n^1 vs. n^2 ligand geometries). To address these issues, variable temperature kinetic studies for both the protic and deuterated species were conducted

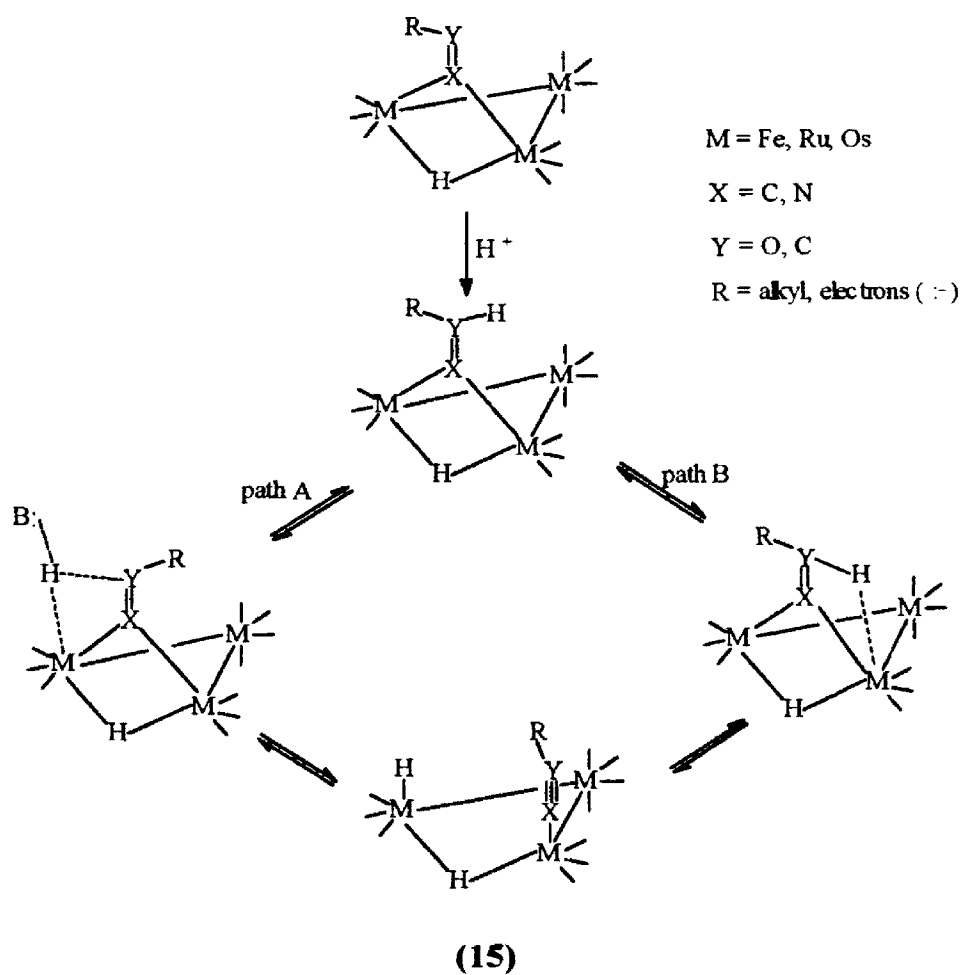
using NMR techniques. This reaction was also studied by UV-Vis spectrophotometry because a color change takes place when going from reactant to products (purple to yellow, respectively). This technique also determined the order of the reaction and whether the coreactant (CF_3CN) was following pseudo-first order conditions.

Another system that will assist in understanding this tunneling phenomena is one dealing with oxygen-to-metal hydrogen transfers. Gladfelter and co-workers reported such a system in the protonation of $[\text{PPN}^+][\text{Ru}_3(\mu\text{-NO})(\text{CO})_{10}]^-$ (**1**) with $\text{CF}_3\text{SO}_3\text{H}$ which resulted in the initial protonation of the nitrosyl oxygen yielding $\text{Ru}_3(\mu\text{-NOH})(\text{CO})_{10}$ (**2**) (eq. 14).^{55,56} However, protonation of **1** with $\text{CF}_3\text{CO}_2\text{H}$ yielded $(\mu\text{-H})\text{Ru}_3(\mu\text{-NO})(\text{CO})_{10}$



(**3**) (eq. 14).^{55,56} The addition of CF_3CO_2^- to compound **2** results in the formation of **3** (eq. 14).^{55,56}

This system will test whether the large KDIE's observed in equations 10 and 11 are indeed proceeding via an intramolecular pathway and not a base assisted intermolecular pathway. An intermolecular pathway is plausible because one can not exclude the possibility of hydrogen transfer being mediated by the base in very tight hydrogen bonded acid-base pairs (eq. 15).⁵⁷ Therefore, the large KDIE's previously observed in equations 10 and 11 could be attributed to the presence of the acid's conjugate base (eq. 10) or trace bases, such as, water (eq. 11).



CHAPTER 2

RESULTS AND DISCUSSION

2.1 The reaction of $\text{H}_2\text{Os}_3(\text{CO})_{10}$ with trifluoroacetonitrile:

When $(\mu\text{-H})_2\text{Os}_3(\text{CO})_{10}$ is treated with CF_3CN in CDCl_3 , a proposed 1 : 1 isomeric adduct $[\text{H}_2\text{Os}_3(\text{CO})_{10}(\text{NCCF}_3)]$ is formed. This adduct then decomposes into two products, $(\mu\text{-H})\text{Os}_3(\text{CO})_{10}(\mu\text{-NC(H)CF}_3)$ (**4**) and $(\mu\text{-H})\text{Os}_3(\text{CO})_{10}(\mu\text{-}\eta^2\text{-HNCCF}_3)$ (**5**) (eq. 13).^{53,54} The formation of these products involve a hydrogen being transferred from the metal to the carbon in case of **4** and to the nitrogen in case of **5**. These metal-to-ligand hydrogen transfer reactions make excellent candidates to perform isotopic substitution experiments which will help in determining isotope effects and perhaps elucidate a mechanism for the reaction.

We have monitored this reaction by ^1H and ^{19}F NMR and found that conversion to **4** and **5** is quantitative. The ^{19}F NMR spectrum is composed of two signals, for **4**, a doublet at 4.9 ppm ($^2J^{19}\text{F-}^1\text{H} = 4.5$ Hz) and for **5**, a doublet at -1.5 ppm ($^2J^{19}\text{F-}^1\text{H} = 2$ Hz). An ^{19}F NMR stack plot shows rate of growth relative to concentration of **4** and **5** with time (Figure 1). The rate constants for the reaction were obtained by integrating each set of doublets and plotting these data versus time using the integrated first-order rate law ($-\ln[A_\infty - A] = kt$).⁵⁸ The kinetic plots (see experimental section figure 17-58) behaved according to first-order kinetics, but the reaction was conducted under pseudo-first order conditions because the gas (CF_3CN) in solution was in such a large excess its concentration was unaffected throughout the course of the reaction.⁵⁸ Each reaction was monitored for at least 2.5 half lives and in most cases 3 half lives. Table 2 provides the rate constants and errors for both the protic and deuterated multiple kinetic runs at each temperature. Good agreement was achieved between duplicate kinetic runs ($\pm 10\%$, Table 2) within this range of temperatures (-20 to 55 °C). The data reveal for the protic

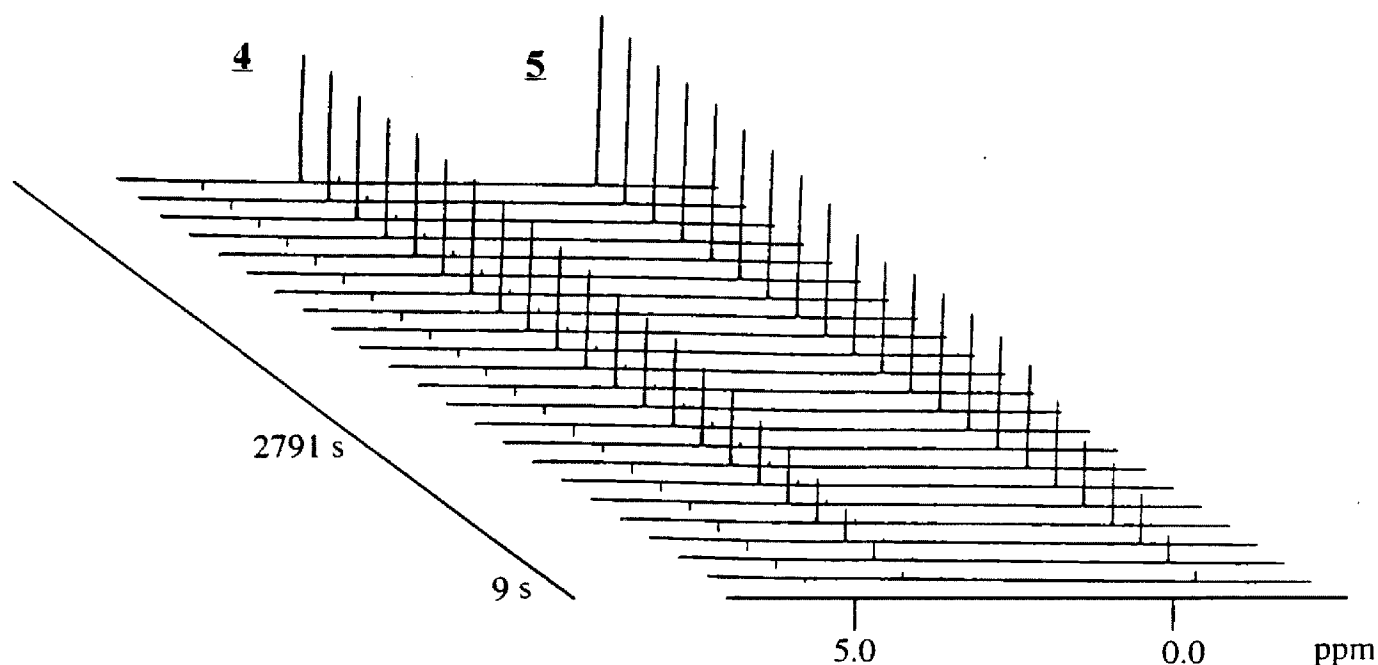


Figure 1 : ^{19}F NMR stack plot of the formation of **4**, $(\mu\text{-H})\text{Os}_3(\text{CO})_{10}(\mu\text{-NC}(\text{H})\text{CF}_3)$ and **5**, $(\mu\text{-H})\text{Os}_3(\text{CO})_{10}(\mu\text{-}\eta^2\text{-HNC}(\text{CF}_3))$ at 25°C .

reactions that the observed rate constants for the two products differ very little, although the product ratios vary significantly over the temperature range studied. This suggests that the rate of formation of the adduct, $\text{Os}_3(\text{CO})_{10}(\mu\text{-H})(\text{H})(\text{CF}_3\text{CN})$ could be the slow step in the reaction. However, this is not the case for the deuterated species where differences in the rate of formation of the two products are observable at -5° and -20°C . This variable temperature study was used to quantify whether proton barrier tunneling was a prominent mechanistic feature in this reaction. The first step in quantifying proton barrier tunneling is to perform isotopic substitution experiments at variable temperatures to determine whether or not an isotope effect is observed. One would expect an increasing KDIE with decreasing temperature if proton barrier tunneling was taking place.

Table 2 : Rate constants and errors for the formation of **4**, (μ -H)Os₃(CO)₁₀
 (μ -NC(H)CF₃) and **5**, (μ -H)Os₃(CO)₁₀(μ - η^2 -HNCCF₃).

Product	T °c	10 ⁴ k _H , sec ⁻¹	10 ⁴ error	10 ⁴ k _D , sec ⁻¹	10 ⁴ error
4	-20	0.13	± 0.0043	0.073	± 0.0022
5	-20	0.16	± 0.0052	0.046	± 0.0029
4	-20	0.11	± 0.0049	0.068	± 0.0014
5	-20	0.16	± 0.012	0.054	± 0.0021
4	-5	0.58	± 0.019	0.54	± 0.013
5	-5	0.55	± 0.016	0.27	± 0.017
4	-5	0.50	± 0.015	0.48	± 0.011
5	-5	0.46	± 0.0098	0.25	± 0.013
4	10	1.36	± 0.011	1.05	± 0.014
5	10	1.42	± 0.0024	1.02	± 0.0024
4	10	1.33	± 0.0017	1.02	± 0.019
5	10	1.34	± 0.0012	1.02	± 0.022
4	25	3.44	± 0.076	2.87	± 0.062
5	25	3.44	± 0.079	2.82	± 0.090
4	25	3.54	± 0.096	3.05	± 0.061
5	25	3.76	± 0.077	2.84	± 0.071
4	40	9.73	± 0.24	X	X
5	40	9.68	± 0.18	X	X
4	40	9.56	± 0.11	X	X
5	40	9.64	± 0.091	X	X
4	55	19.13	± 0.51	X	X
5	55	19.76	± 0.40	X	X
4	55	20.86	± 0.61	X	X
5	55	21.10	± 0.68	X	X

A "maximum" isotope effect without tunneling is determined by the differences in zero-point energies associated with metal-hydrogen or metal-deuterium bond which is lost in the linear symmetrical transition state, so that the activation energy for the deuterium transfer is higher only by the difference in zero-point energies.^{29,47,59} A value larger than the one described above should be considered anomalous and tunneling may explain this anomaly.²⁹

Averaged observed rate constants show increasing isotope effects with decreasing temperature for **5**, but remain fairly constant for **4** (Table 3).

Table 3 : Average rate constants and Kinetic Deuterium Isotope Effects for the formation of **4, ($\mu\text{-H}$)Os₃(CO)₁₀($\mu\text{-NC(H)CF}_3$) and **5**, ($\mu\text{-H}$)Os₃(CO)₁₀($\mu\text{-}\eta^2\text{-HNCCF}_3$).**

Product	T °C	ave. 10 ⁴ k _H , sec ⁻¹	ave. 10 ⁴ k _D , sec ⁻¹	k _H /k _D
4	-20	0.12	0.071	1.70
5	-20	0.16	0.050	3.86*
4	-5	0.54	0.51	1.06
5	-5	0.51	0.26	2.69*
4	10	1.35	1.04	1.30
5	10	1.38	1.02	1.85*
4	25	3.49	2.96	1.18
5	25	3.60	2.83	1.74*

* values corrected using a deuterium correction factor (0.73) as the fraction of deuterium in the final products as measured by ¹ H NMR.

However, this is the overall observed rate constant for the entire reaction without capturing and isolating the adduct. This strongly suggests that the rate of formation of the

adduct is very slow compared to the extremely fast rate of disappearance of the adduct going to the two products as discussed above. Therefore, the KDIE's observed using the observed rate constants may be attenuated for both products. The KDIE for **5** however, is definitely larger.

Because the adduct could not be isolated, the rate constants for the disappearance of the adduct could not be obtained. We decided to use product ratios which are provided in the ^{19}F NMR spectra (Figure 2).

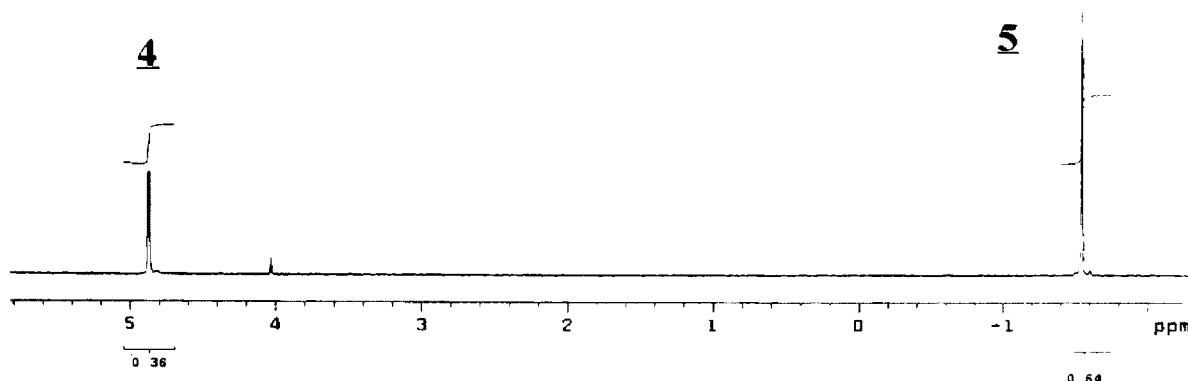


Figure 2: ^{19}F NMR spectrum showing product ratios and integrated peak areas of **4**, $(\mu\text{-H})\text{Os}_3(\text{CO})_{10}(\mu\text{-NC(H)CF}_3)$ and **5**, $(\mu\text{-H})\text{Os}_3(\text{CO})_{10}(\mu\text{-}\eta^2\text{-HNCCF}_3)$.

Product ratios are a function of the two product's rate of formation related to the adduct. These are not the actual rates of formation, but these data will provide a better understanding of the mechanism involved. The protic data in Table 4 reveals that the relative concentration of **4** decreases with decreasing temperature whereas **5** increases with decreasing temperature. The deuterated data in Table 4 show that the relative concentration of both **4** and **5** remain fairly constant at the different temperatures. Table 4 also shows the trend of the observed KDIE's increasing with decreasing temperature.

Table 4 : Average product ratios and Kinetic Deuterium Isotope Effects for the formation of 4, ($\mu\text{-H}$)Os₃(CO)₁₀($\mu\text{-NC(H)CF}_3$) and 5, ($\mu\text{-H}$)Os₃(CO)₁₀($\mu\text{-}\eta^2\text{-HNCCF}_3$).

	T °C	ratio p4	ratio p5	p4/p5= k	k _H /k _D
protic	-20	0.26	0.74	3.40	4.33*
deuterated	-20	0.45	0.56	0.786	
protic	-5	0.29	0.71	2.45	3.94*
deuterated	-5	0.46	0.54	0.852	
protic	10	0.33	0.67	2.03	3.01*
deuterated	10	0.48	0.52	0.923	
protic	25	0.36	0.64	1.78	2.86*
deuterated	25	0.46	0.54	0.852	
protic	40	0.40	0.60	1.5	
protic	55	0.42	0.58	1.38	

* values corrected using a deuterium correction factor (0.73).

However, these isotope effects may be misleading and not reveal their true significance because the actual rate constants in going from adduct to products could not be obtained. Because these data exhibit an increase in the KDIE's with decreasing temperature, this suggests that deuterium substitution had a significant impact on the reaction's mechanism.

To verify that the formation of the product's overall observed rate constants are indeed correct, the reactant's rate of disappearance should be compared to the rate appearance of products. One would expect that the reactant's rate of disappearance to match or be extremely close to the product's rate of appearance. Duplicate experiments using ¹H NMR were conducted at 25 °C to determine the reactant's rate of disappearance for this

reaction. An ^1H NMR stack plot showing the disappearance of reactant and the appearance of **4** and **5** with time is found in Figure 3.

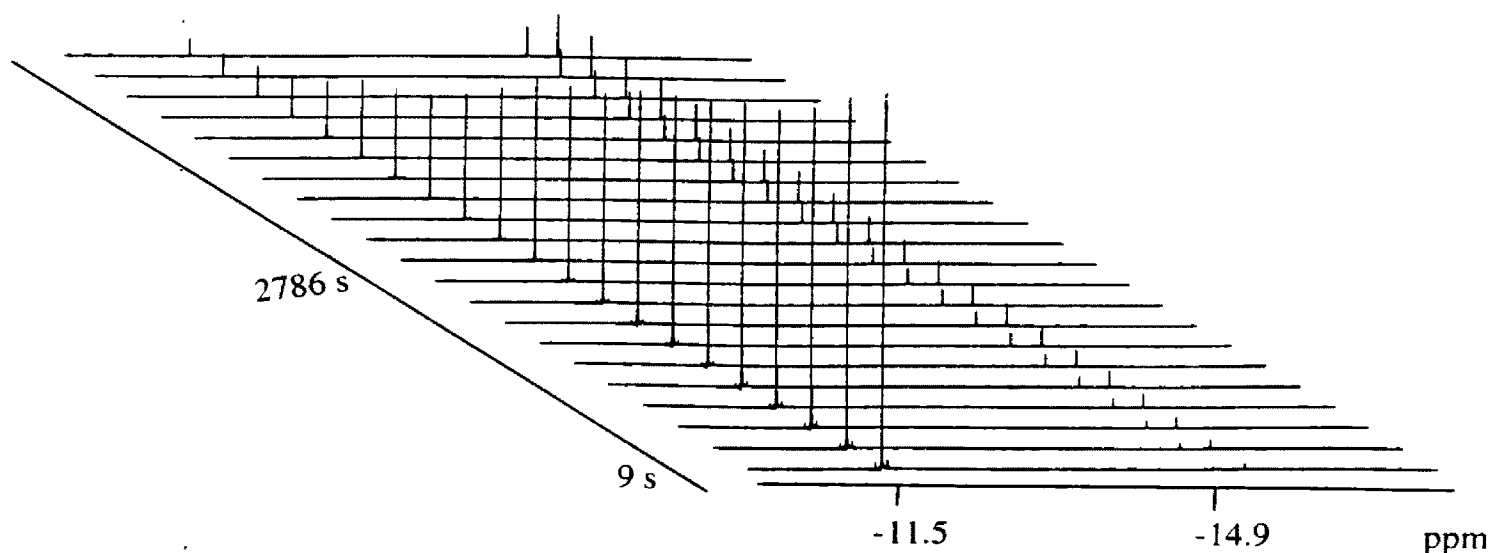


Figure 3: ^1H NMR stack plot of the disappearance of reactant, $\text{H}_2\text{Os}_3(\text{CO})_{10}$ and the formation of **4**, $(\mu\text{-H})\text{Os}_3(\mu\text{-NC}(\text{H})\text{CF}_3)$ and **5**, $(\mu\text{-H})\text{Os}_3(\text{CO})_{10}(\mu\text{-}\eta^2\text{-HNCCF}_3)$ with time at 25°C .

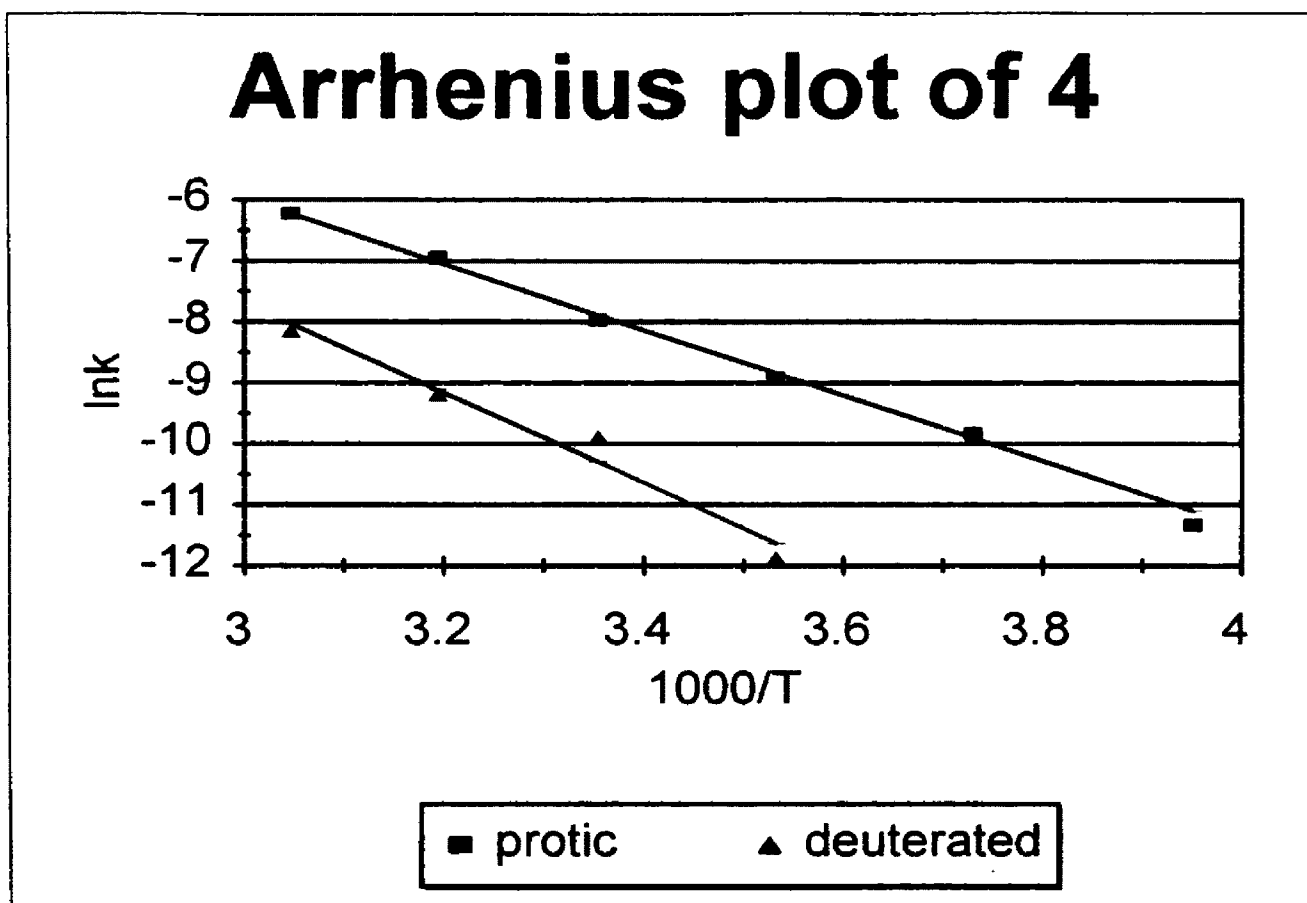
The results obtained from these kinetic experiments ($k_{\text{obsvd}} = 3.58 \times 10^{-4} \pm .04 \times 10^{-4} \text{ sec}^{-1}$) show that the rate of reactant disappearance are in good agreement with the rate of formation of products ($k_{\text{obsvd}} = 3.55 \times 10^{-4} \text{ sec}^{-1}$) (see experimental section Figure 57-58 for individual kinetic plots).

We also attempted to detect the formation of the initial adduct. This was done by cooling solutions of $\text{H}_2\text{Os}_3(\text{CO})_{10}$, exposed to an excess of CF_3CN , to -80°C where exchange of the hydrides should be slow. We could not detect the adduct. This is consistent with its rate of formation being the slow step in the reaction.

Another test to determine proton barrier tunneling is using variable temperature kinetics to obtain an Arrhenius plot. These plots provide valuable pieces of information, such as, the activation energy (E_a) for the reaction, preexponential factor (A), and linearity due to temperature dependence. Deviation from linearity especially at lower temperatures could signify a tunneling component in a reaction where the reaction becomes less temperature dependent. Conversely, at higher temperatures the reaction follows classical mechanics where traversal of the barrier is highly temperature dependent.⁴⁷ This nonlinearity at lower temperatures is very dependent on the width of the potential energy barrier which means that if proton barrier tunneling is occurring the barrier width is narrow.⁴⁷ However, the temperature ranges that would exhibit nonlinear behavior in an Arrhenius plot could be difficult if not impossible to determine especially at lower temperatures where reactions could be extremely slow.⁴⁷

The Arrhenius plot of the overall observed rate constants for **4** is given in Figure 4. This plot is linear for both the protic and deuterated cases. However, these are the overall reaction rate constants which are dominated by the rate of adduct formation and not by the formation of **4**. The activation energies (E_a) of the protic and deuterated reaction were determined from the Arrhenius plots ; $E_{aH} = 11.1$ kcal/mol, $E_{aD} = 12.0$ kcal/mol. The difference in activation energies ($\Delta E_{aD/H}$) is 0.90 kcal/mol. The last piece of information obtained from an Arrhenius plot is the preexponential factor (A). This apparent A factor is useful in determining whether proton barrier tunneling is a viable explanation in certain reactions. Barrier tunneling is suspected when $A^D \gg A^H$, which is anomalous in terms of collision theory.⁴⁷ The A factor is dependent on the number of collisions and spatial orientation which means the protic A should be faster than the deuterated A .⁴⁷ Therefore, proton barrier tunneling should be suspected when the A_{obsd}^D / A_{obsd}^H ratio is greater than one.⁴⁷

The observed protic preexponential factor (A_{obsd}^H) for **4** obtained from the Arrhenius

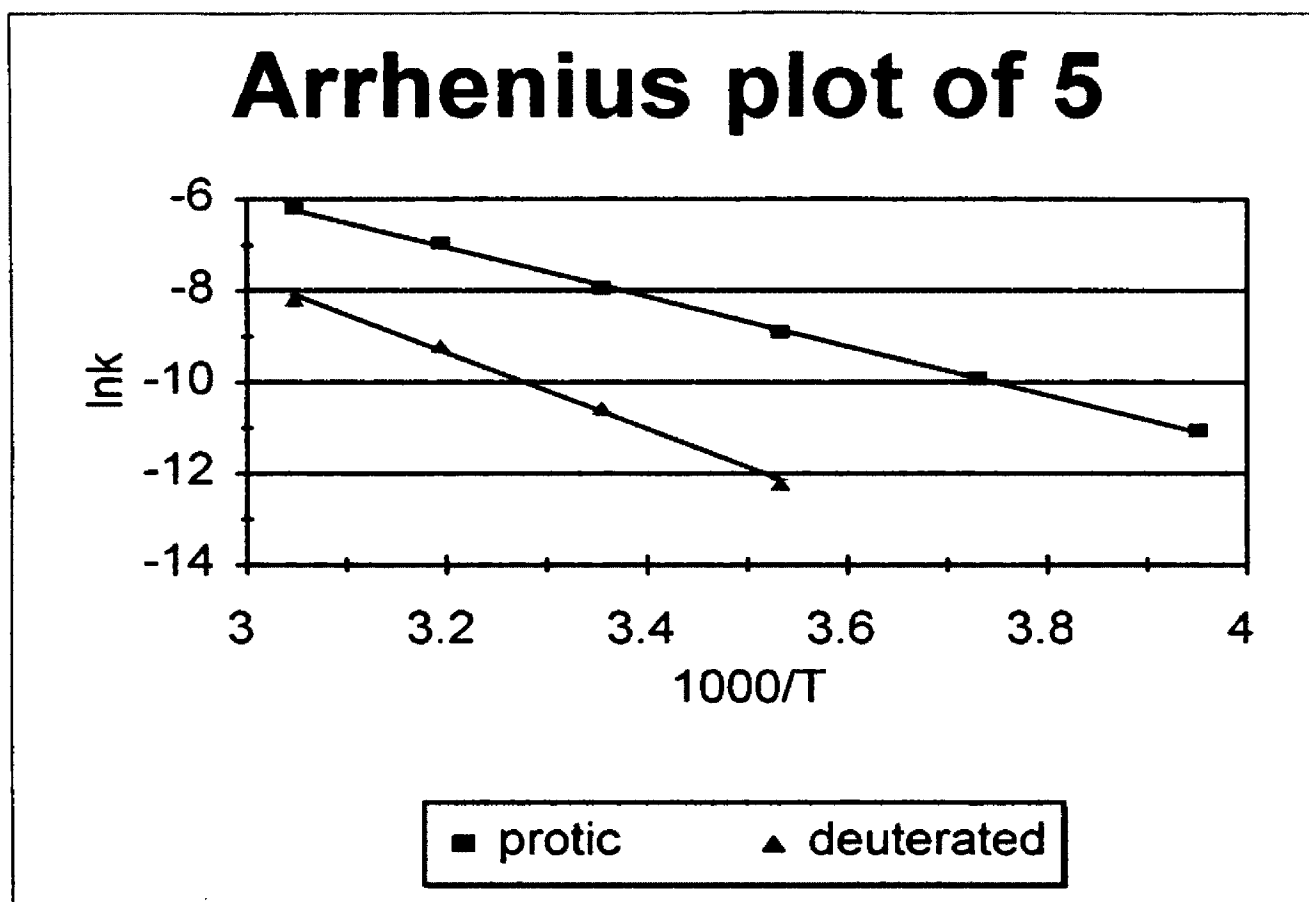


$$E_{a_H} = 11.1 \text{ kcal/mole}$$

$$E_{a_D} = 12.0 \text{ kcal/mole}$$

$$\Delta E_{a_D}^D = 0.90 \text{ kcal/mole}$$

Figure 4: Arrhenius plot of the formation of 4, ($\mu\text{-H}$)Os₃(CO)₁₀($\mu\text{-NC(H)CF}_3$).



$$E_{a_H} = 10.7 \text{ kcal/mole}$$

$$E_{a_D} = 13.5 \text{ kcal/mole}$$

$$\Delta E_{a_D^H} = 2.8 \text{ kcal/mole}$$

Figure 5: Arrhenius plot of the formation of **5**, $(\mu\text{-H})\text{Os}_3(\text{CO})_{10}(\mu\text{-}\eta^2\text{-HNCCF}_3)$.

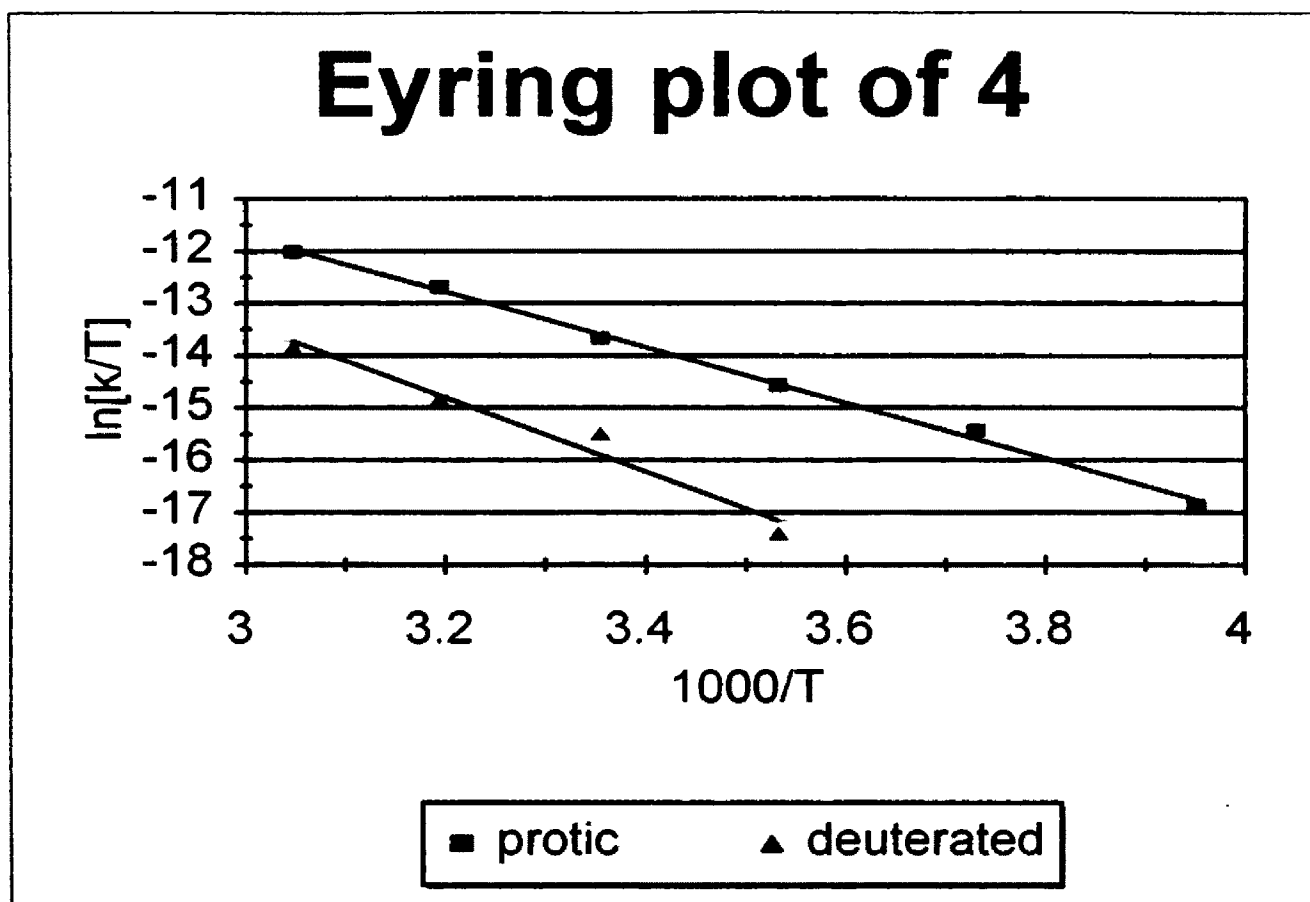
plot was $5.2 \times 10^4 \text{ sec}^{-1}$, the deuterated preexponential factor ($A_{\text{obsd}}^{\text{D}}$) was $2.0 \times 10^5 \text{ sec}^{-1}$. The ratio, $A_{\text{obsd}}^{\text{D}} / A_{\text{obsd}}^{\text{H}} = 3.8$, is large compared to what is considered a typical value. The Arrhenius plot of the overall observed rate constants for **5** is given in Figure 5. This plot is linear for both protic and deuterated cases. The activation energies (E_a) of the protic and deuterated reaction determined from the Arrhenius plots are $E_{a\text{H}} = 10.7 \text{ kcal/mol}$, $E_{a\text{D}} = 13.5 \text{ kcal/mol}$. The difference in activation energies ($\Delta E_{a\text{D}\text{H}}$) is 2.8. This value is 3 times greater than the one observed for **4**.

The observed protic preexponential factor ($A_{\text{obsd}}^{\text{H}}$) for **5** obtained from the Arrhenius plot was $2.8 \times 10^4 \text{ sec}^{-1}$, the deuterated preexponential factor ($A_{\text{obsd}}^{\text{D}}$) was $2.5 \times 10^6 \text{ sec}^{-1}$. The ratio, $A_{\text{obsd}}^{\text{D}} / A_{\text{obsd}}^{\text{H}} = 89.3$, is extremely large compared to what is considered a typical value. This value is approximately 20 times greater than the one observed for **4**.

An Eyring plot is another plot to help quantify proton barrier tunneling. Important information obtained from these plots are: change in enthalpy energy (ΔH^\ddagger), change in entropy energy (ΔS^\ddagger), and linearity due to temperature dependence. Both plots, Arrhenius and an Eyring exhibit the same linear behavior, deviations from this linearity should be considered anomalies.

The Eyring plot of the overall observed rate constants for **4** is given in Figure 6. This plot is linear for both the protic and deuterated cases which is consistent with the Arrhenius plot. The enthalpies (H) of the protic and deuterated reactions were determined from the Eyring plots; $\Delta H_{\text{H}}^\ddagger = 10.5 \text{ kcal/mol}$, and $\Delta H_{\text{D}}^\ddagger = 11.4 \text{ kcal/mol}$. The entropies (S) of the protic and deuterated reactions were $\Delta S_{\text{H}}^\ddagger = -8.33 \text{ kcal/mol K}$, and $\Delta S_{\text{D}}^\ddagger = -11.1 \text{ kcal/mol K}$. The deuterated $\Delta S_{\text{D}}^\ddagger$ is 1.3 times larger than the protic ($\Delta S_{\text{H}}^\ddagger$).

The Eyring plot of the overall observed rate constants for **5** is given in Figure 7. This plot is also linear for both protic and deuterated cases. The enthalpies (H) of the protic and deuterated reactions were $\Delta H_{\text{H}}^\ddagger = 10.5 \text{ kcal/mol}$, and $\Delta H_{\text{D}}^\ddagger = 12.7 \text{ kcal/mol}$. The deuterated $\Delta H_{\text{D}}^\ddagger$ values from both plots are larger than the ones found for the protic



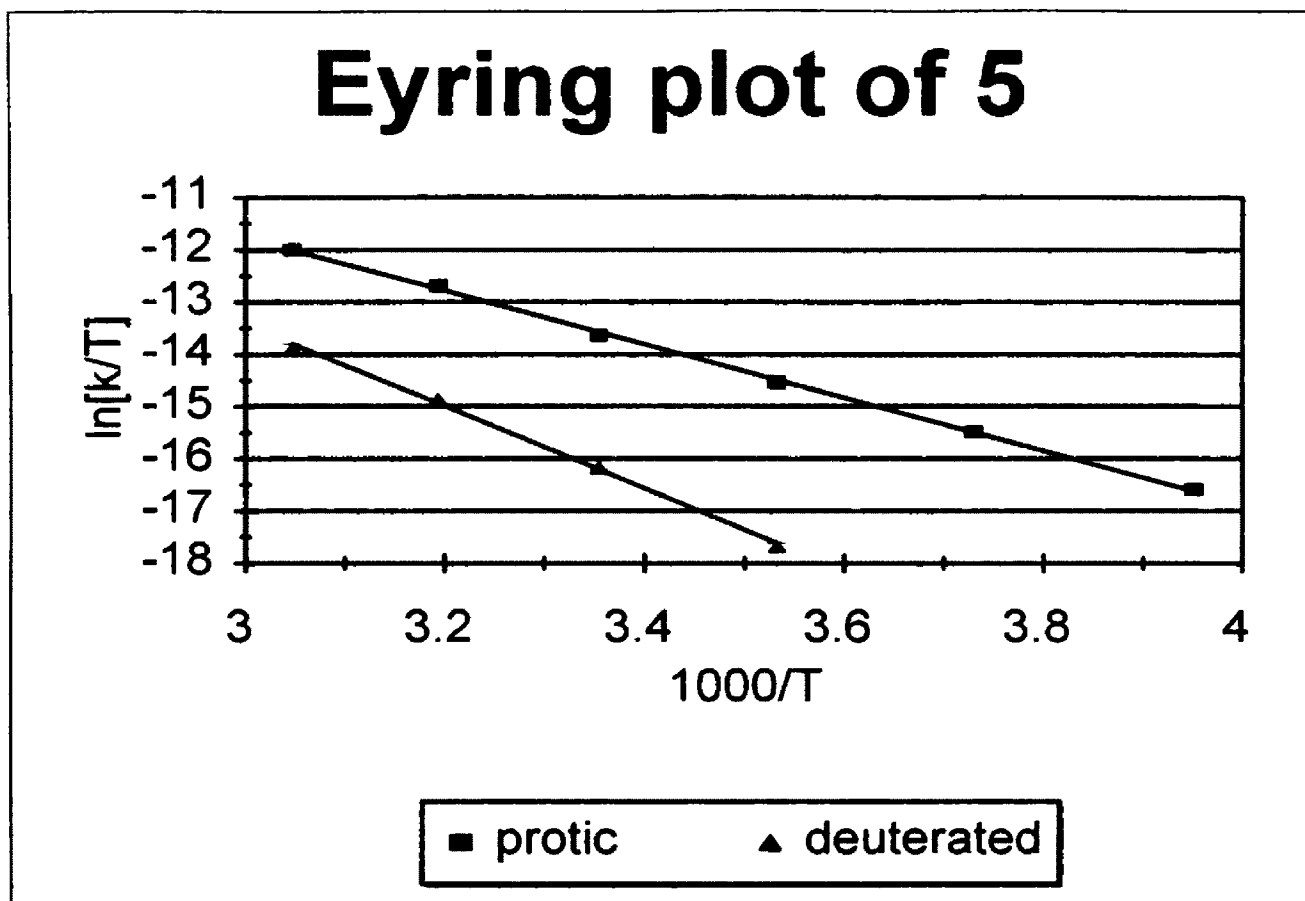
$$\Delta H_{\text{H}}^{\ddagger} = 10.5 \text{ kcal/mol}$$

$$\Delta H_{\text{D}}^{\ddagger} = 11.4 \text{ kcal/mol}$$

$$\Delta S_{\text{H}}^{\ddagger} = -8.33 \text{ kcal/mol K}$$

$$\Delta S_{\text{D}}^{\ddagger} = -11.1 \text{ kcal/mol K}$$

Figure 6: Eyring plot of the formation of 4, $(\mu\text{-H})\text{Os}_3(\text{CO})_{10}(\mu\text{-NC}(\text{H})\text{CF}_3)$.



$$\Delta H_{\text{H}}^{\ddagger} = 10.1 \text{ kcal/mol}$$

$$\Delta H_{\text{D}}^{\ddagger} = 12.7 \text{ kcal/mol}$$

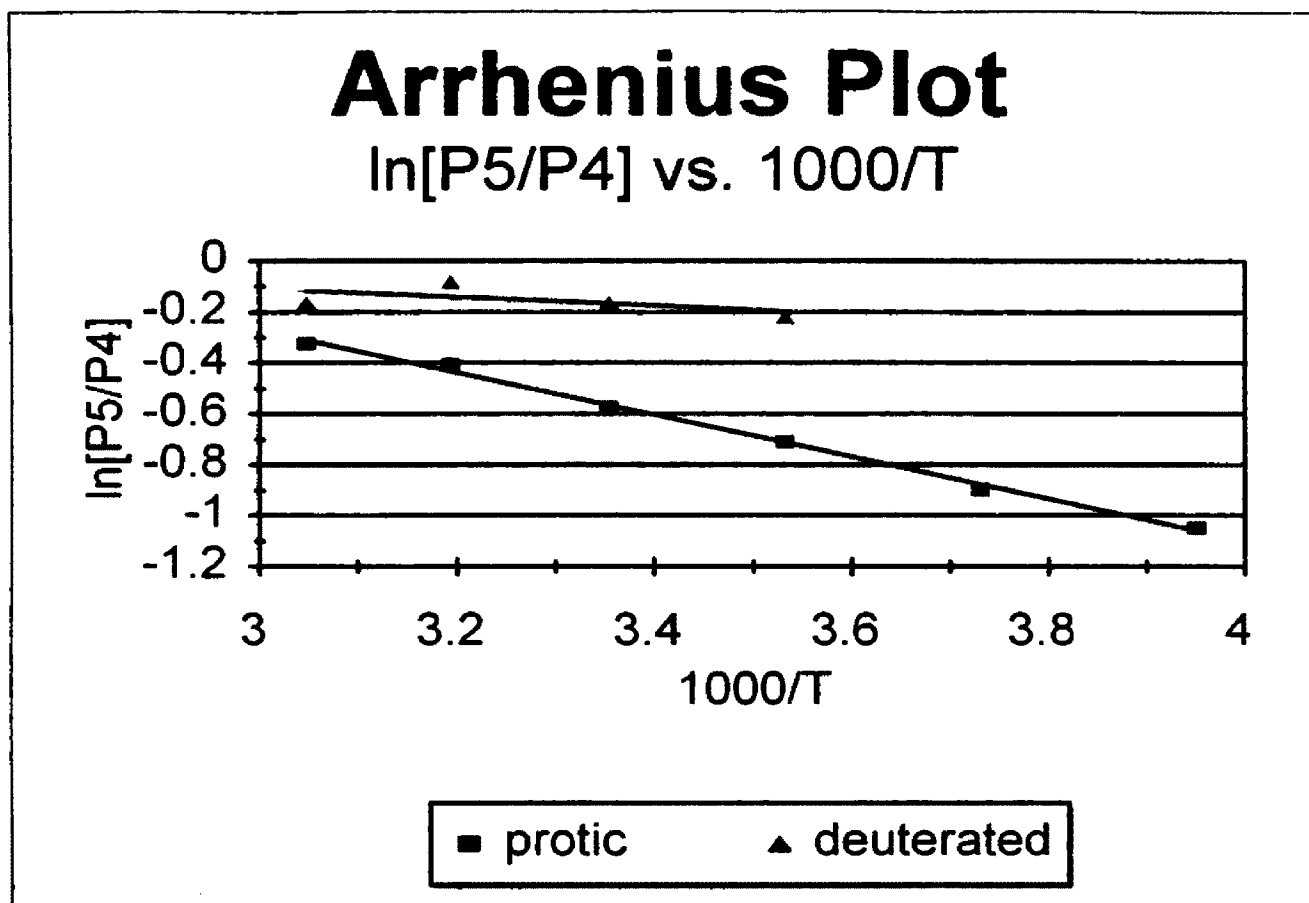
$$\Delta S_{\text{H}}^{\ddagger} = -7.07 \text{ kcal/mol K}$$

$$\Delta S_{\text{D}}^{\ddagger} = -15.3 \text{ kcal/mol K}$$

Figure 7: Eyring plot of the formation of 5, ($\mu\text{-H}$)Os₃(CO)₁₀($\mu\text{-}\eta^2\text{-HNCCF}_3$).

ΔH_{H^\ddagger} , but more important is that the observed ΔH_{D^\ddagger} for **5** is greater than the ΔH_{D^\ddagger} for **4**. The entropies (S) of the protic and deuterated were determined from the Eyring plots; $\Delta S_{H^\ddagger} = -7.07$ kcal/mol K, and $\Delta S_{D^\ddagger} = -15.3$ kcal/mol K. The deuterated ΔS_{D^\ddagger} for **5** is twice as large than the protic ΔS_{H^\ddagger} whereas for **4**, it is only 1.3 times larger. This is consistent for a reaction mechanism exhibiting proton barrier tunneling where a large negative value is observed for ΔS^\ddagger .^{33,60,61} Tunneling is most likely to occur when there is a narrow barrier width, because the narrower the width means that the geometry of the reactant going to product changes very little, and this gives rise to a highly ordered transition state, thus a large negative ΔS^\ddagger is observed.^{33,60,61}

Arrhenius plots of the product ratios were also prepared which are given in figure 8. Deviation from linearity was not observed in either the protic or deuterated plots. The change in activation energies (ΔE_a) for both the protic and deuterated cases are small values which is to be expected since $\Delta E_a = (E_{a_{prod4}} - E_{a_{prod5}})$. The observed value for the protic, ΔE_{a_H} , was 1.64 kcal/mol, and the deuterated, ΔE_{a_D} , was 0.655 kcal/mol. The deuterated, ΔE_{a_D} , case is the most interesting in that the observed product ratios remain fairly constant, thus one would suspect a slope of zero or close to zero. This means that the barrier height (E_a) remains the same or is slightly higher for both **4** and **5** when deuterium is substituted for protons. The observed protic preexponential factor (A_{obsd}^H) obtained from this Arrhenius plot was 9.11, and the deuterated preexponential factor (A_{obsd}^D) was 1.40. The ratio, $A_{obsd}^D / A_{obsd}^H = 0.154$, is close to the typical value of 1 where no tunnelling is observed. However, because these data are obtained from ratio differences one may conclude that these values are reduced, and may not reflect their true significance in regards to proton barrier tunneling.



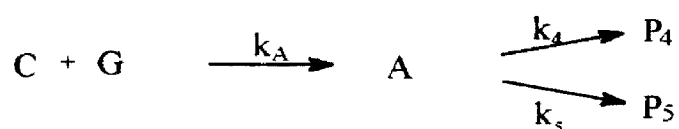
$$\Delta E_{a_H} = 1.64 \text{ kcal/mol}$$

$$\Delta E_{a_D} = 0.655 \text{ kcal/mol}$$

Figure 8: Arrhenius plots of product ratios obtained from ^{19}F NMR spectra.

2.2 Simplified mathematical treatment:

A proposed mechanism for this reaction is found in equation 16. Where C represents the compound, $(\mu\text{-H})_2\text{Os}_3(\text{CO})_{10}$, G is the gas (CF_3CN) , A is the intermediate adduct, and P_4 and P_5 are **4** and **5**, respectively, and k_4 and $k_5 \gg k_A$.



(16)

Now, if the intermediate's concentration obeys equation 17, then it is assumed that the mass balance equations found in Equation 18 are correct.^{57,62,63} Where C_0 is the initial concentration of the cluster.

$$[\text{A}] \ll [\text{C}], [\text{P}_4], [\text{P}_5]$$

(17)

$$C_0 = \text{C} + \text{P}_4 + \text{P}_5 \quad \text{and} \quad C_0 = \text{P}_{4\infty} + \text{P}_{5\infty}$$

(18)

Therefore, the kinetic expressions for the reaction are (eq. 19):

$$\begin{array}{ll} -\frac{d\text{C}}{dt} = k_A\text{C} & \frac{d\text{A}}{dt} = k_A\text{C} - k_4\text{P}_4 - k_5\text{P}_5 \\ \frac{d\text{P}_4}{dt} = k_4\text{A} & \frac{d\text{P}_5}{dt} = k_5\text{A} \end{array}$$

(19)

Now assuming steady state conditions, and solving for A (eq. 20):^{57,62,63}

$$\frac{dA}{dt} = 0 \quad \text{so,}$$

$$k_A C = k_4 A + k_5 A \quad \text{which yields:}$$

$$A = \frac{k_A C}{k_4 + k_5}$$

(20)

Therefore, expressions for each product are obtained as (eq.21):

$$\frac{dP_4}{dt} = \frac{k_A k_4}{k_4 + k_5} C \quad \text{and} \quad \frac{dP_5}{dt} = \frac{k_A k_5}{k_4 + k_5} C$$

(21)

The kinetic data are expressed for $[P_4]$ and $[P_5]$, therefore, $[C]$ must be expressed in terms of P_4 and P_5 (eq. 22):^{57,62,63}

$$C_o = C + P_4 + P_5 \quad \text{and} \quad C_o = P_{4oo} + P_{5oo}$$

therefore,

$$C = C_o - P_4 - P_5$$

$$C = P_{5oo} + P_{4oo} - P_4 - P_5$$

(22)

Because both $[P_4]$ and $[P_5]$ appear in the above equations, a new expression is generated where $K_p = P_4/P_5$, this is then rearranged to become (eq. 23):^{57,62,63}

$$P_5 = \frac{P_4}{K_p} \quad \text{which is substituted for } [P_5]$$

$$C = P_{5_{00}} + P_{4_{00}} - P_4 - \frac{P_4}{K_p}$$

$$C = P_{5_{00}} + P_{4_{00}} - \left(1 + \frac{1}{K_p}\right) P_4$$

(23)

However, it is also correct that $P_{5_{00}} = P_{4_{00}}/K_p$, which is then substituted for $P_{5_{00}}$, yielding (eq. 24):^{57,62,63}

$$C = P_{4_{00}} + \frac{P_{4_{00}}}{K_p} - \left(1 + \frac{1}{K_p}\right) P_4$$

and,

$$C = \left(1 + \frac{1}{K_p}\right) P_{4_{00}} - \left(1 + \frac{1}{K_p}\right) P_4$$

which rearranges to,

$$C = \left(1 + \frac{1}{K_p}\right) (P_{4_{00}} - P_4)$$

which gives the following expression:

$$\frac{dP_4}{dt} = \frac{k_A k_4 \left(1 + \frac{1}{K_p}\right)}{k_4 + k_5} (P_{4_{00}} - P_4)$$

(24)

It is also believed that $K_p = k_4 / k_5$, which is then substituted in the above equation to give (eq. 25):^{57,62,63}

$$\frac{dP_4}{dt} = \frac{k_A k_4 (1 + \frac{k_5}{k_4})}{k_4 + k_5} (P_{400} - P_4)$$

which finally gives the expression:

$$\frac{dP_4}{dt} = k_A (P_{400} - P_4)$$

(25)

This expression is now integrated to give Equation 26:

$$\ln \frac{P_{400} - P_4}{P_{400}} = -kt$$

(26)

The same procedures are followed for $[P_5]$.

2.3 The reaction of $\text{H}_2\text{Os}_3(\text{CO})_{10}$ with trifluoroacetonitrile followed by UV-Vis Spectroscopy :

UV-Vis Spectroscopy was used to verify the assumption that the rate law for this reaction was indeed, first-order kinetics, and therefore, the interpretation of the observed kinetic data are based on the pseudo-first order conditions of this reaction.

Kinetic experiments were conducted using five different gas (CF_3CN) volume additions which resulted in increasing rate constants. This is consistent with collision theory where one would expect more collisions to occur by increasing the concentration of reactants. Rate constants and associated errors for the formation of **4** and **5**, using different volumes of gas, are found in Table 5. These are the overall observed rate constants for the entire

Table 5 : Rate constants and errors measured by UV-Vis Spectroscopy for the formation of **4, ($\mu\text{-H}$) $\text{Os}_3(\text{CO})_{10}$ and **5**, ($\mu\text{-H}$) $\text{Os}_3(\text{CO})_{10}(\mu\text{-}\eta^2\text{-HNCCF}_3)$.**

	$10^4 k_{\text{H}}$, sec^{-1}	10^4error
1 ml of gas	0.2164	0.01194
1 ml of gas	0.3704	0.0004473
4 ml of gas	1.458	0.005609
4 ml of gas	1.301	0.002476
6 ml of gas	2.206	0.001191
6 ml of gas	2.193	0.0007659
8 ml of gas	2.600	0.001219
10 ml of gas	3.150	0.1154
10 ml of gas	2.986	0.03136

reaction which includes both the formation of the adduct and the adduct's disappearance into the two products.

A kinetic plot showing rate constants increasing with time, using the five different gas volumes is found in Figure 9.

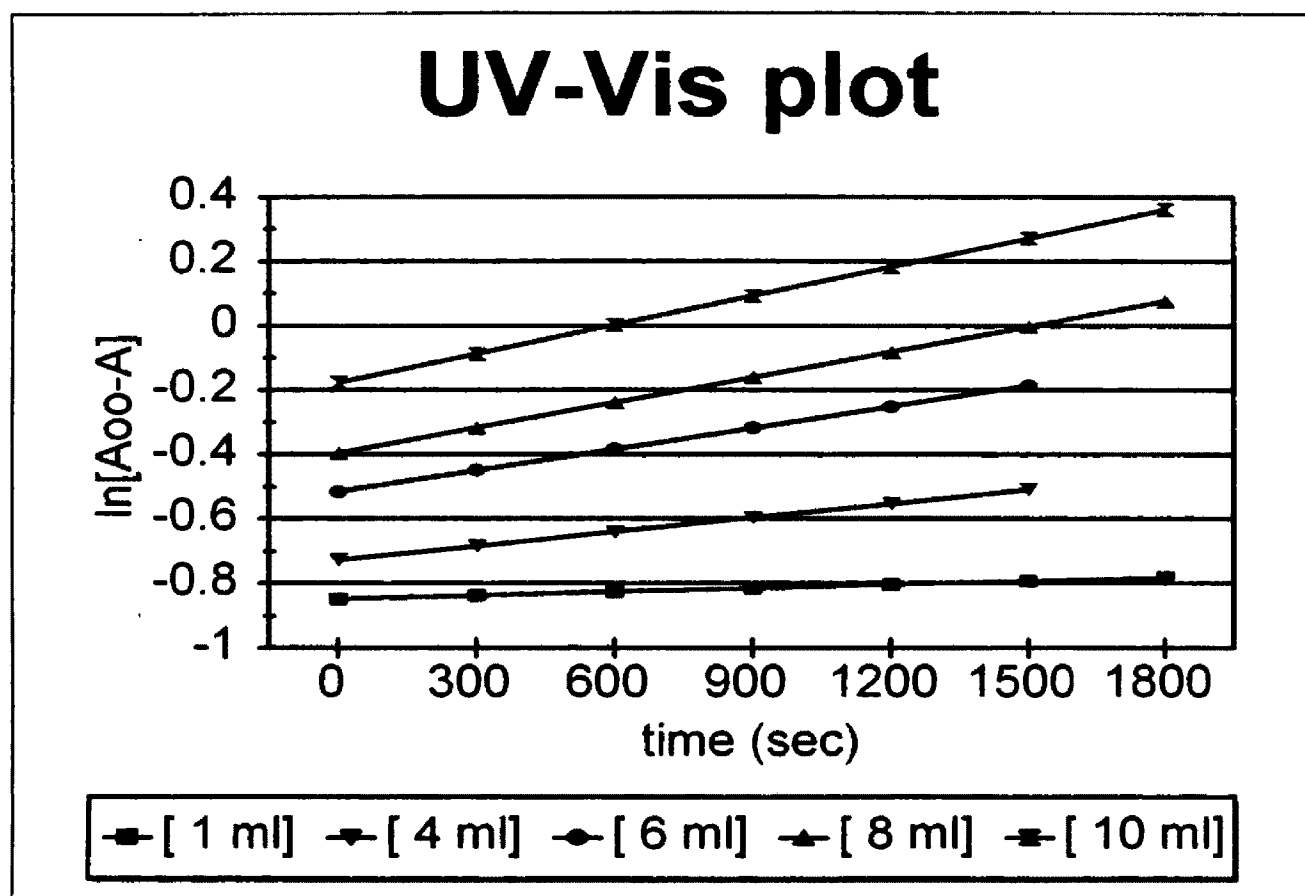


Figure 9: UV-Vis kinetic plot of the formation of both 4 and 5 using variable gas volumes.

Earlier experiments revealed that both 4 and 5 show maximum absorption at 392 nm. Because, each product absorbed light at the same wavelength it was impossible to differentiate between the two products. Therefore, molar absorptivity experiments using Beer's Law were conducted on each product to determine their extinction coefficients. Extinction coefficients were determined for the starting compound, $(\mu\text{-H})_2\text{Os}_3(\text{CO})_{10}$ and

for **4**, $(\mu\text{-H})\text{Os}_3(\text{CO})_{10}(\mu\text{-NC(H)CF}_3)$ and **5**, $(\mu\text{-H})\text{Os}_3(\text{CO})_{10}(\mu\text{-}\eta^2\text{-HNCCF}_3)$.

These determinations were made using a starting concentration of ~ 4 mmole/liter for each compound which were then diluted by a factor of 2.5 each time, so each compound contained five different concentrated solutions. Absorptions were determined at their maximum absorbance (392 nm) which resulted in extinction coefficients of 221.8 $\text{L}/(\text{cm} \cdot \text{mol})$ for the starting cluster, and values of 2159.7 and 9374.5 $\text{L}/(\text{cm} \cdot \text{mol})$ for **4** and **5**, respectively. Because, the extinction coefficients of **4** and **5** are different, the absorbance observed at 392 nm is not a true reflection of their concentration.

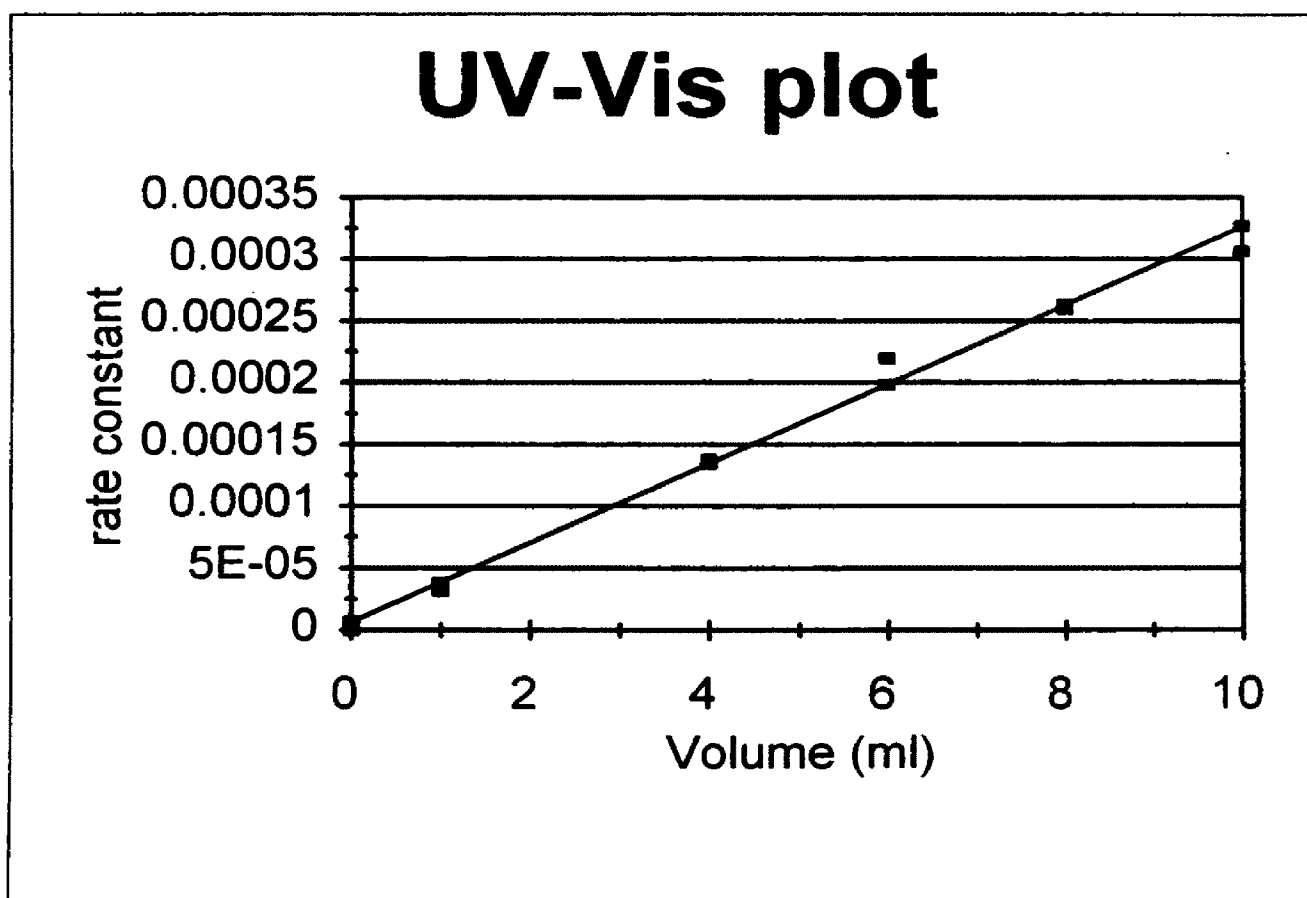


Figure 10: UV-Vis kinetic plot of rate constants versus volume of gas (CF_3CN) used.

To verify whether pseudo-first order kinetics conditions are followed, a plot of rate constants versus volume of gas (CF_3CN) was prepared (Figure 10). If pseudo-first order conditions are fulfilled, this plot should be linear and the y-intercept should go through the origin. This plot shows good linearity with a slope value of 3.2×10^{-5} , and the y-intercept goes through the origin, indicating that the reactions are following pseudo-first order conditions.

These experiments also revealed two isosbestic points which are shown in Figure 11.

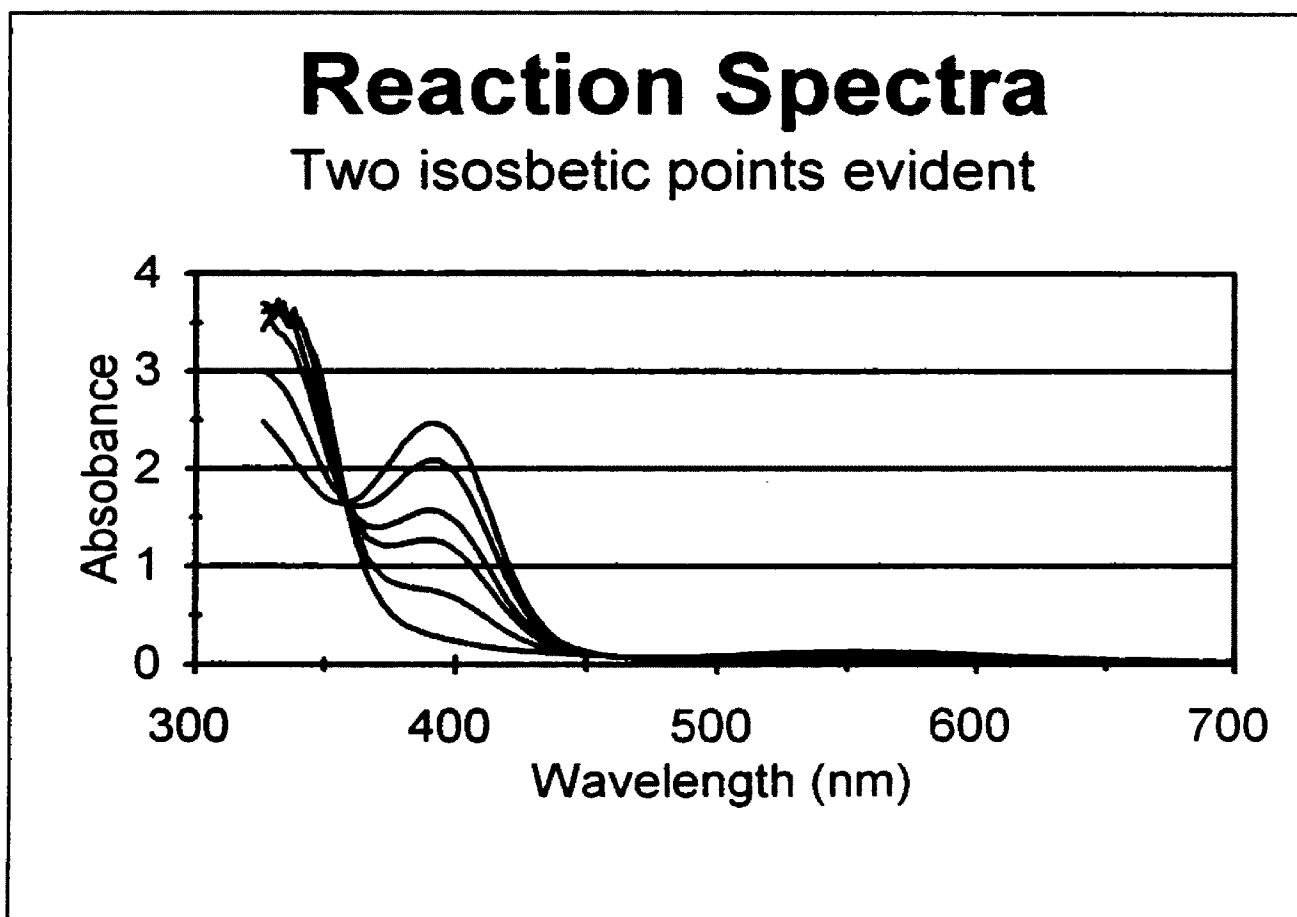


Figure 11: UV-Vis kinetic spectrum where two isosbestic points are evident, performed at 25°C, with 4 ml of gas (CF_3CN).

The isosbestic point is where the absorbance due to the reactant's decomposition equals the absorbance of the product being formed. However, the determination and interpretation as to why there was two isosbestic points was not performed at this time. This was considered another project and will be conducted at a later date. Individual UV-Vis kinetic plots are found in Figures 59-67, after the experimental section.

2.4 The reaction of $\text{PPN}[\text{Ru}_3(\text{CO})_{10}(\mu\text{-NO})]$, **1**, with $\text{CF}_3\text{SO}_3\text{X}$ and $\text{CF}_3\text{CO}_2\text{X}$ (X= H or D) followed by ^{13}C NMR spectroscopy:

Experiments were conducted using ^{13}C NMR techniques on ^{13}CO -enriched samples of **1**. This allowed us to explore these reactions using variable temperature (VT) ^{13}C NMR in order to monitor the conversion of **1** to **2** and the conversion of **2** to **3** using both protonated and deuterated acids ($\text{CF}_3\text{SO}_3\text{X}$ and $\text{CF}_3\text{CO}_2\text{X}$ where X= H or D).

The VT- ^{13}C NMR study began by monitoring compound **1** which at -80°C , produced a spectrum consisting of four resonances in the carbonyl region at 211.08, 204.89, 203.15, and 198.66 ppm with relative intensities of 1:1:6:2 (Figure 12). However, upon warming the sample of **1** to 25°C , these four resonances converged into a single broad resonance at 203.25 ppm. This is reasonable, because the average weighted chemical shift of the four

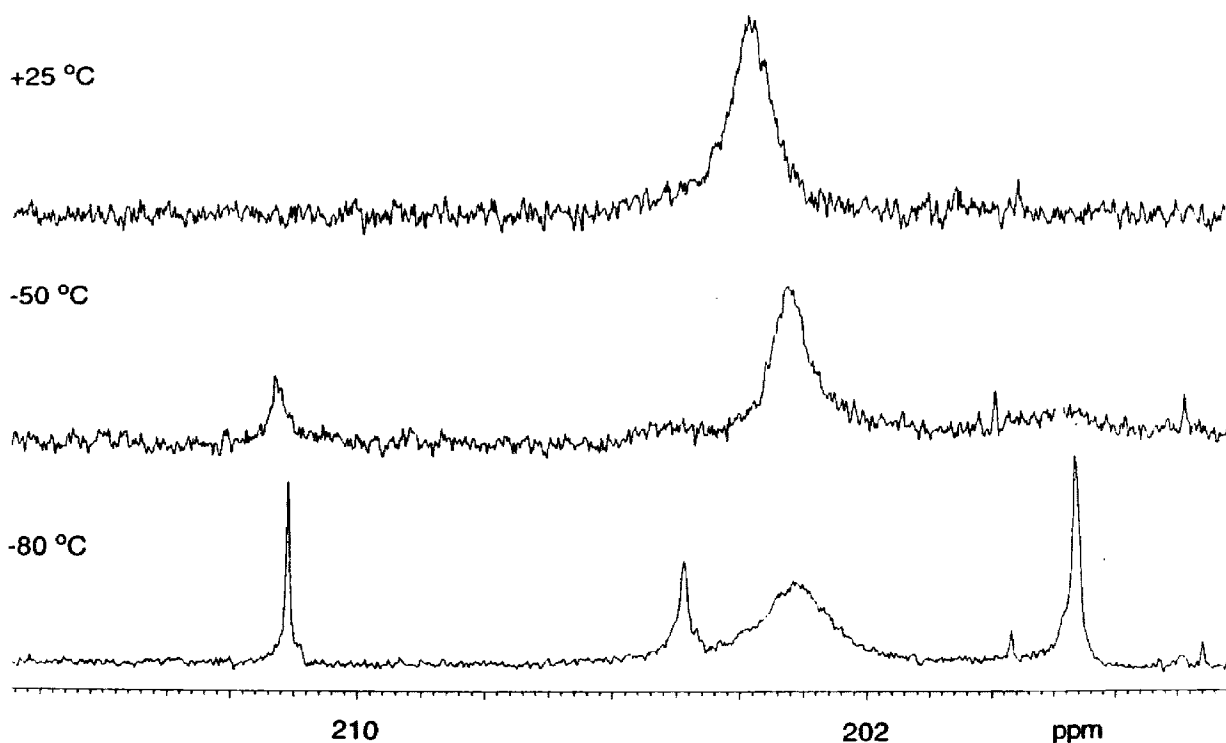
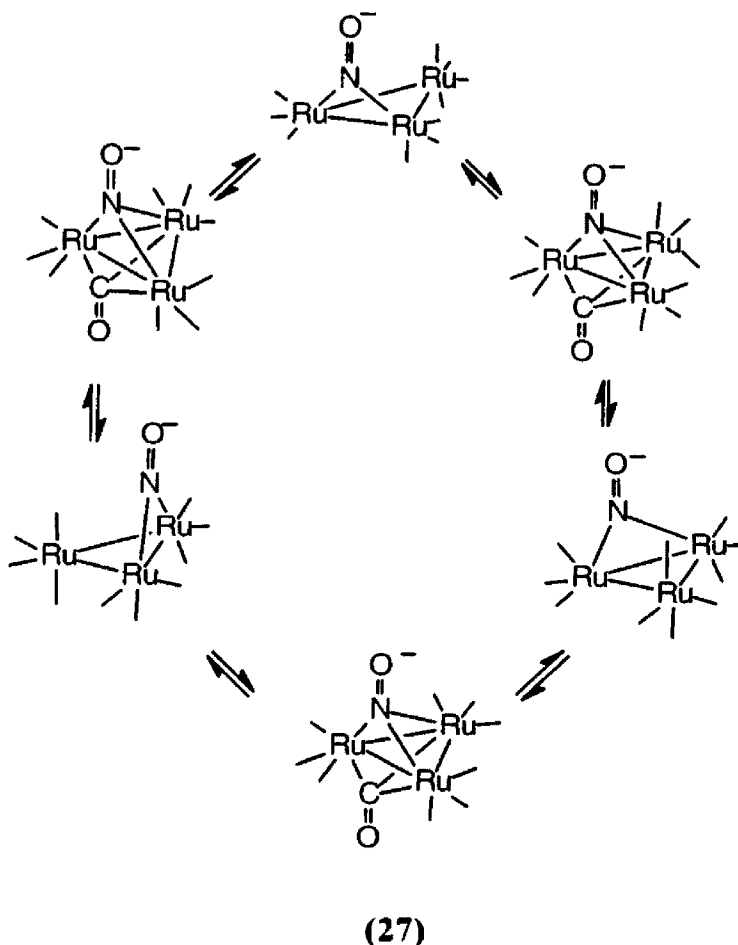


Figure 12: VT- ^{13}C NMR spectra of **1 in $\text{CD}_2\text{Cl}_2/\text{CH}_2\text{Cl}_2$, focusing on the carbonyl region at 100 MHz.**

resonances observed at -80°C is 203.22 ppm. The broad resonance appearing in the -80°C spectrum at 203.15 ppm with a relative intensity of six, arise from the twin sets of three carbonyl groups. Each set is bonded to one ruthenium atom bridged by the nitrosyl group which undergoes a tripodal motion on the NMR time scale. The non-equivalent axial carbonyl groups bonded to ruthenium atom as the $\text{Ru}(\text{CO})_4$ moiety in **1**, give rise to the interchangeable resonances at 211.08 and 204.89 ppm. Whereas, the resonance at 198.66 ppm, with a relative intensity of two, arises from the equivalent radial carbonyls on the same $\text{Ru}(\text{CO})_4$ moiety.

A complete averaging of all the carbonyl groups gives rise to the broad resonance observed after heating the sample. The simplest mechanism to explain this would be for the nitrosyl ligand and one of the axial carbonyls on the $\text{Ru}(\text{CO})_4$ moiety to form a μ_3 bonding mode which changes **1**, to where the bridging nitrosyl group is now along a different edge of the Ru_3 triangle, and therefore, the $\text{Ru}(\text{CO})_4$ group is on a different ruthenium atom. Further, because both the axial carbonyls found on the $\text{Ru}(\text{CO})_4$ moiety, and the carbonyl groups found on the $\text{Ru}(\text{CO})_3$ group are undergoing a tripodal motion would cause the interchange of all the carbonyl groups (eq. 27).⁶⁴ However, one can not rule out the possibility of a more complex mechanism, or perhaps, mechanisms, but this is probably the most likely considering the ground state structure of **2**.

When a ^{13}C -enriched sample of **1** is protonated with $\text{CF}_3\text{SO}_3\text{H}$ at ambient temperature, the -80°C ^{13}C NMR spectrum shows two sharp resonances in the carbonyl region. The chemical shifts for these resonances are 195.30 and 192.02 ppm with a relative intensity of 1:2 (Figure 13a). The two pseudo-radial and one pseudo-axial terminal carbonyls in **2** gives rise to these observed resonances.⁵⁶ A third, very broad signal, at a chemical shift of 264.7 ppm, appears in the spectrum which is just barely



detectable above noise. This resonance is probably due to the triple bridging carbonyl ligand found in **2**.⁶⁵ However, as the temperature is increased to 25°C, the two formally distinct upfield resonances merge together to form a single broad resonance at 193.38 ppm (Figure 13b). The weighted average of the two terminal carbonyls observed from the -80°C spectrum was 193.11 ppm which agrees well with the chemical shift of the single resonance observed in the 25°C spectrum.

Compound **2** changes color, from red to amber, when 0.4 eq. of $\text{PPNCF}_3\text{CO}_2$ is added to this solution at 25°C. Six resonances are observed in the ^{13}C NMR spectrum at chemical shifts of 201.59, 201.35, 194.22, 194.09, and 183.46 ppm with a relative intensity of approximately 2:1:1:2:2:2. These six resonances are consistent that **2**

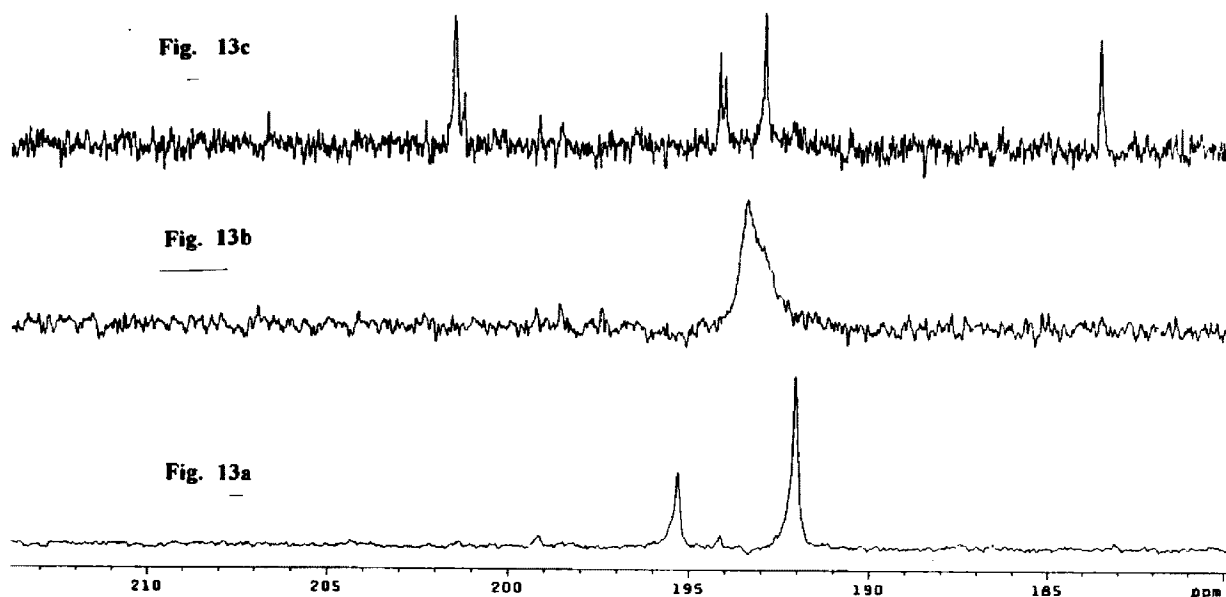


Figure 13: a) ^{13}C NMR spectrum of the carbonyls of **2** in $\text{CD}_2\text{Cl}_2/\text{CH}_2\text{Cl}_2$ at -80°C and at 100 MHz (where **1** is protonated with 1 eq. $\text{CF}_3\text{SO}_3\text{H}$).
 b) ^{13}C NMR spectrum of **2** at 25°C .
 c) ^{13}C NMR spectrum of **2** converted to **3** after the addition of 0.4 eq. of $\text{PPNCF}_3\text{CO}_2$ at 25°C .

converted to **3**,⁵⁶ (Figure 13c) because this spectrum is identical to the one obtained when 1 eq. of CF_3COOH was added to **1** at 25°C . No conversion of **2** to **3** was observed when PPNCF_3O_2 was injected at -80°C , however, conversion was observed when the sample was warmed to 10°C . The ^{13}C NMR spectrum showed very little change when $\text{CF}_3\text{SO}_3\text{D}$ was used followed by the addition of $\text{PPNCF}_3\text{CO}_2$. However, the changes observed for **3** were some disappearance of multiplicity or the broadness of the carbonyl resonances at 201.59, 192.94, and 183.46 ppm. These changes are attributed to the lack of partially

resolved proton couplings with the bridging hydride in the deuterated analog.

When a ^{13}C -enriched sample of **1** is protonated with 1 eq. of either CF_3COOH or CF_3COOD at -80°C , the ^{13}C NMR spectrum is identical to the one observed at 25°C , when **1** was protonated with $\text{CF}_3\text{SO}_3\text{H}$ (Figure 14a). Partial conversion of **2** to **3** was observed when the sample was heated to 10°C for both the protonated and deuterated cases (Figure 14b).

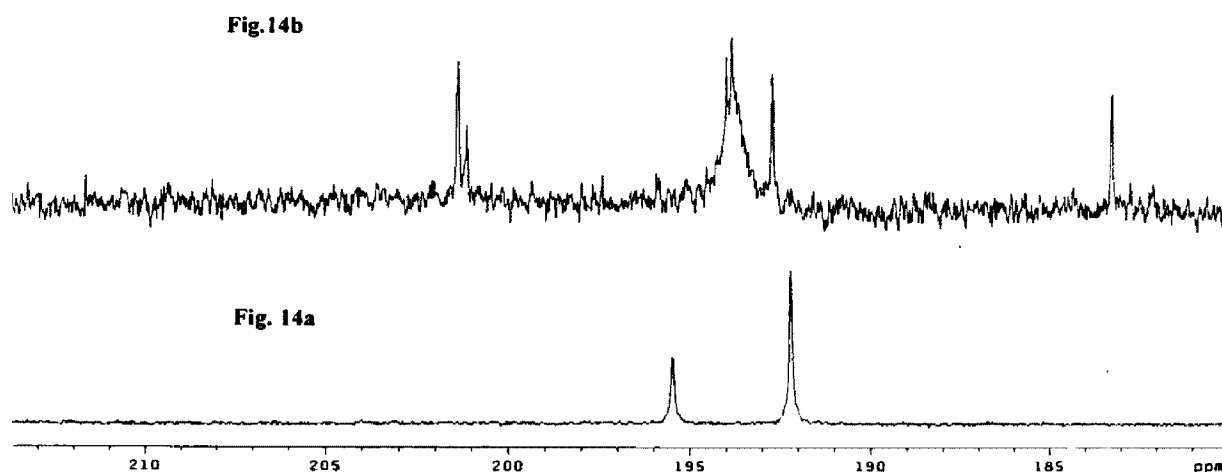


Figure 14: a) ^{13}C NMR spectrum of **1** after the addition of 1 eq. of $\text{CF}_3\text{CO}_2\text{H}$ or $\text{CF}_3\text{CO}_2\text{D}$ at -80°C .
 b) ^{13}C NMR spectrum of **1** after the addition of 1 eq. of $\text{CF}_3\text{CO}_2\text{H}$ or $\text{CF}_3\text{CO}_2\text{D}$ at -80°C which is heated to 10°C showing the partial conversion of **2** to **3**.

However, total conversion to **3** was observed when the sample was heated to 25°C. Therefore, at low temperatures, regardless of which acid was used, CF₃CO₂X (X = H or D), initial protonation occurred at the nitrosyl oxygen. However, O-protonation was not observed at low temperatures when the complex, Ru₃(CO)₁₀(μ-CO)(μ-H)⁻ was protonated with CF₃CO₂H, but investigators did observe O-protonations using acids, such as, CF₃SO₃H or FSO₃H.^{52,66} Because O-protonation was not observed in the reaction of Ru₃(CO)₁₀(μ-CO)(μ-H)⁻ with CF₃CO₂H, suggests that initial protonation may be kinetic in origin, and that the proton transfer to the metal core is very fast at the temperature examined (-40°C).

When a ¹³CO-enriched sample of **1** is protonated with 0.3 eq. of CF₃CO₂H at -80°C, the ¹³C NMR spectrum shows partial conversion of **1** to **2** (Figure 15). When the solution was heated to 10°C, the resonances for **1** and **2** began to average independently. However, when a temperature of 25°C was reached, the spectrum showed **2** completely converted to **3** which appeared as well defined resonances (Figure 15). This suggests that the carbonyl exchange is slow between **1** and **3** on the NMR time scale at 25°C. In another experiment, a sample of ¹³CO-enriched **1** was protonated with an excess of CF₃SO₃H at 25°C, then cooled to -80°C, where a ¹³C NMR spectrum was recorded that showed resonances associated with both **2** and **3**. The sample was then warmed to ambient temperature where the spectrum showed that resonances associated with **2** had broadened but remained well defined in the case of **3**. However, judging from the ¹³C NMR spectrum, considerable decomposition had occurred which was probably due to the excess acid. This experiment did show that conversion of **2** to **3** is possible in the presence of excess CF₃SO₃H, but considerably slower than what was observed when CF₃CO₂H was used.

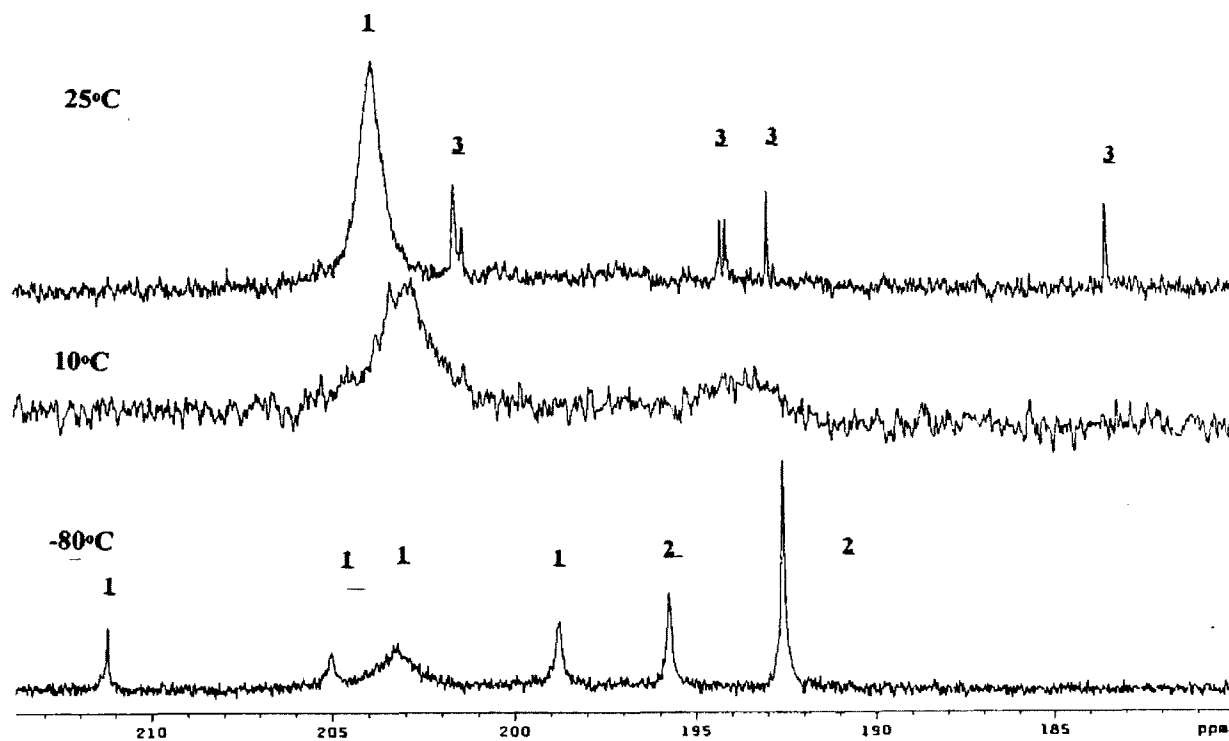


Figure 15: Variable temperature ^{13}C NMR spectra of **1 after the addition of 0.3 eq. of $\text{CF}_3\text{CO}_2\text{H}$ in $\text{CD}_2\text{Cl}_2/\text{CH}_2\text{Cl}_2$ at 100 MHz.**

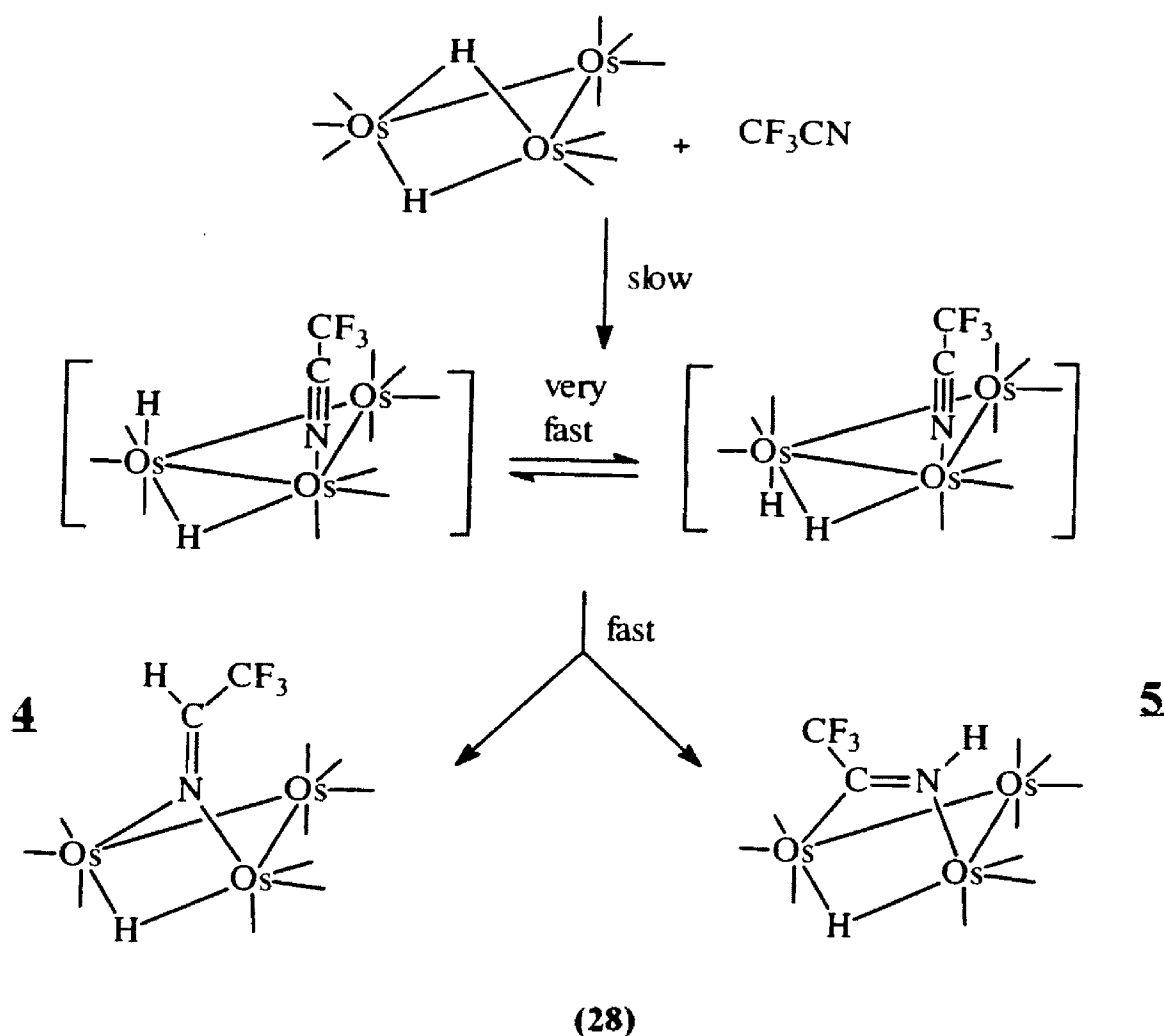
CHAPTER 3

CONCLUSIONS / FUTURE WORK

Verification of proton barrier tunneling can be a formidable task even on the best of chemical systems. These tasks include that good kinetic data are obtained and the following criteria be met: 1) an Arrhenius plot that exhibits deviation from linearity due to the proton transfer becoming less dependent on temperature; 2) that the preexponential ratios (A_D/A_H) are greater than one; 3) that the KDIE's (k_H/k_D) increase with decreasing temperature; 4) that the change in entropy (ΔS^\ddagger) becomes more negative in the case of the deuterated species.

The kinetic data obtained for this system all exhibit the specific trends for a reaction associated with a tunneling component especially in the case of **5**. Kinetic plots of **4** and **5** did not show deviation in linearity which suggests that rate constants are temperature dependent. However, kinetic plots that show deviations from linearity are difficult to obtain because reactions become extremely slow at lower temperatures where one would expect such deviations to occur. The observed kinetic deuterium isotope effects (k_H/k_D) for **5** increased with decreasing temperatures, whereas the isotope effect for **4** remained fairly constant. The preexponential factor ratio ($A_{\text{obsd}}^D / A_{\text{obsd}}^H$) for **5** was determined to be 89.3 which is ~ 24 times larger than the one observed for **4**. The observed deuterated change in entropy (ΔS_D^\ddagger) for **5** was -15.3 kcal/mole K which is 2 times larger than for **4**. These trends suggest that proton barrier tunneling is a major contributor in this reaction's mechanism, especially in the case of **5**. However, verification of a chemical reaction's mechanism is difficult, therefore, good experimental design is required to collect the best supportive data. The data collected from these experiments supports a mechanism that exhibits proton barrier tunneling. However, these data are the reaction's overall observed rate constants. The adduct (transition state) could not be isolated which means that the observed rate constants include both the rate of adduct's formation and

disappearance. This raises the question as to whether the observed isotopic data were attenuated or not? The data suggest that the rate of adduct formation is slow compared to the rate of adduct disappearance. This means that the slow rate constant (adduct formation) will dominate the overall reaction's rate constant. Therefore, the extremely fast rate constant (adduct disappearance) will not be as prevalent in the observed overall reaction's rate constant. Because the hydrogen transfer takes place in the adduct disappearance step, one would expect that the isotope effect occurring at this step to be large, but since this is the fast step and not the dominate one, then the observed KDIE's would be attenuated. The proposed mechanism for this reaction is found in equation 28.



The adduct's back reaction where it reverts back to the starting cluster is extremely slow or relatively non-existent. The hydrogen transfer step must be fast because there is no accumulating concentration of the adduct which explains why the adduct could not be detected. The *cis-trans* interconversion is extremely fast and it is not known which adduct isomer leads to which product, or perhaps only one of the adduct forms the two products (eq. 28).³³ This determination could not be made with the data collected. Regardless of which adduct leads to which product, the fluxionality exhibited by these adducts probably plays an important role as to why proton barrier tunneling is observed in this mechanism.^{26,33} The energy involved in fluxionality may be comparable to the reaction's activation energy which would assist in the possibility of tunneling by raising the hydrogen part way up the potential energy barrier where the barrier width is narrower.^{26,33} The activation energies obtained from the Arrhenius plots substantiate these claims by having values within reason to assist the hydrogen part way up the barrier.

The geometry of these species also explains why proton barrier tunneling is observed in this reaction. The barrier's width becomes narrower allowing the hydrogen to tunnel through if the adduct-product species geometry is similar. Because **5** exhibits a larger tunneling component than **4**, it appears that a more protic transition state is more likely to show this effect.³³ All cases reporting anomalously large KDIE in organometallic reactions involve some type of proton transfer.^{26,33,59} Polarity of the hydrogen transfer is probably a more important factor in determining the effectiveness of tunneling than the geometric positioning of the ligand to the cluster in the final product. The large isotope effects observed for **5** could mean that the metal-to-nitrogen hydrogen transfer is facilitated by a hydrogen bonded intermediate.^{67,68}

Experiments involving compound **1**, clearly show that the site of protonation is the nitrosyl oxygen regardless of which acid was used, CF₃SO₃H or CF₃CO₂H. No large KDIE was observed with the anion assisted conversion of **2** to **3** because this conversion

was too rapid by the methods used in monitoring this reaction. A large KDIE is possible for this conversion but is probably imbedded in such a rapid process. Because of the similarities between this conversion and that of equations 11 and 12, we suggest that an intramolecular process is responsible for the observed large KDIE. However, future studies using a more rapid kinetic technique will confirm the above conclusion. These preliminary studies have allowed a generalization, in that the intermolecular base assisted proton transfer (path a, eq. 15) is more rapid than the intramolecular process (path b, eq. 15).

In the future, we will investigate the generality of proton barrier tunneling in a variety of transition metal centers. Systems worth studying deal with protonations of oxygen in complexes, such as, $(\mu_3\text{-CO})(\mu\text{-CO})\text{M}_3(\text{CO})_9^{2-}$ (M= Fe, Ru, Os). These types of complexes contain face bridging carbonyls which should be the site of protonation. This will provide us an understanding of the conversion of oxygen protonated species which we can compare to already known species, such as, $(\mu\text{-H})(\mu\text{-CO})\text{M}_3(\text{CO})_{10}^{1-}$. Studying these systems should provide us with a general trend in predicting where to expect proton transfers.

CHAPTER 4

EXPERIMENTAL

Materials

The compounds ($\mu\text{-H}$)₂Os₃(CO)₁₀, and ($\mu\text{-D}$)₂Os₃(CO)₁₀ were prepared according to literature procedures.^{69,70} Os₃(CO)₁₂ was purchased from Strem Chemicals and stored in a desiccator dried with CaCl₂. Solvents were ACS reagent grade and were distilled with an appropriate drying agent and stored over molecular sieves. Chloroform-d₁ was purchased from Aldrich and was stored over phosphorous pentoxide (PO₅) followed by freeze-thaw technique to maintain a dry, oxygen-free solvent which is then distilled directly into the storage vessel. Trifluoroacetonitrile was purchased from Lancaster Chemicals.

Spectra

Nuclear magnetic resonance spectra were obtained on a Varian Unity Plus 400 MHz spectrometer. ¹H NMR spectra were recorded in CDCl₃ solutions in the fourier transform mode where the solvent peak (7.24 ppm) was used as an internal standard to calibrate the spectra. Fluorine-19 NMR spectra were recorded in CDCl₃ solutions in the fourier transform mode where CF₃COOH (0.0 ppm) was used as an external standard to calibrate the spectra. UV-Vis spectra were obtained on a Hewlet-Packard 8452A Diode Array spectrophotometer operating in the kinetics mode in CDCl₃.

Preparation of H₂Os₃(CO)₁₀ + CDCl₃ stock solution:

The stock solution was prepared by transferring 20 ml of dried CDCl₃ to a flame dried Schlenk tube via trap-to-trap distillation. The Schlenk tube, and other necessary equipment, were then transported into a Braun Basic System MB 150 dry box which

maintains an atmosphere of dry nitrogen. ($\mu\text{-H}$)₂Os₃(CO)₁₀ (299.6 mg, 0.3304 mmol) was placed in an oven dried 10 ml volumetric flask and brought to volume by syringing in 10 ml of CDCl₃. The stock solution with a concentration of 0.03304 mol/liter was stored in the dry box until needed.

Preparation of D₂Os₃(CO)₁₀ + CDCl₃ stock solution:

($\mu\text{-D}$)₂Os₃(CO)₁₀ (154.1 mg, 0.1696 mmol) was placed in an oven dried 5 ml volumetric flask and brought to volume by syringing in 5 ml of CDCl₃. The stock solution with a concentration of 0.03261 mol/liter was stored in the dry box until needed.

Kinetic runs of X₂Os₃(CO)₁₀ + CF₃CN, X = H or D:

Samples were prepared by syringing 0.6 ml of the stock solution into a flamed dried J. S. Young Valve 5 mm NMR tube (Brunfeldt or Wilsnad). The NMR tube was inserted into a specially designed manometric vacuum manifold apparatus designed specifically for syringing gases into NMR tubes (Figure 16). The contents of the tube were then frozen using liquid N₂ and sealed under vacuum (10⁻² torr). The gas, CF₃CN, (0.20 mmol) was released into the manifold passing through a drying tube containing Aquasorb (Mallincrodt) to remove any residual H₂O in the gas. The gas was monitored with the manometer and the gas flow was stopped when a pressure of 1 atmosphere was obtained. A Hamilton gas tight syringe was used to remove 5 ml (0.20 mmol) of the gas which was injected into the evacuated NMR tube. The tube was then removed from the apparatus and placed in a dry ice/acetone bath and allowed to reach temperature. The tube was then inserted into the NMR instrument where the reaction was monitored using an NMR kinetic software program. This program is designed for setting variable timed arrays

as a function of absolute intensity which maintains the integrity of the spectra so relative concentrations are obtained via peak integration. Fluorine-19 NMR was used exclusively in kinetic runs because signal intensities change with ^1H NMR when switching from protic to deuterated reactants. Kinetic runs with $(\mu\text{-H})_2\text{Os}_3(\text{CO})_{10}$ were conducted at 55, 40, 25, 10, -5, and -20°C , and runs with $(\mu\text{-D})_2\text{Os}_3(\text{CO})_{10}$ at 25, 10, -5, and -20°C .

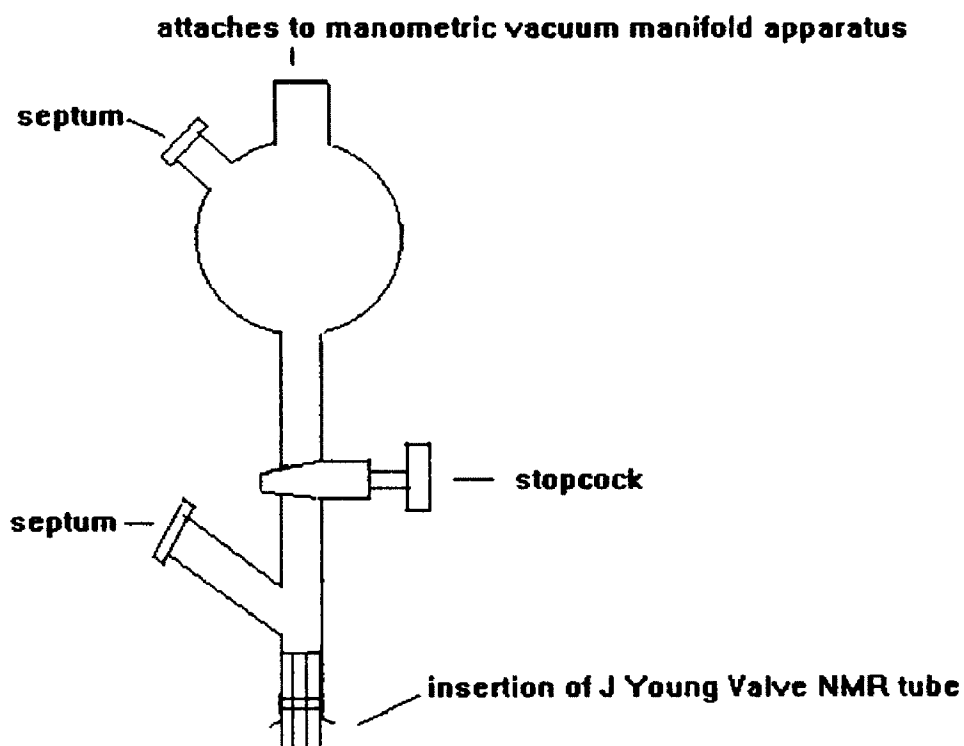


Figure 16: Specially designed glassware to inject gas compounds into NMR tubes.

Each kinetic run was performed in duplicate or sometimes in triplicate to ensure repeatability and data agreement. Duplicate experiments at the various temperatures

were done in random to reduce systematic and random errors associated with experimentation. Product **4**, ($\mu\text{-X}$)Os₃(CO)₁₀($\mu\text{-NC(X)CF}_3$), X = H or D appeared as a doublet at 4.86 ppm, and **5**, ($\mu\text{-X}$)Os₃(CO)₁₀($\mu\text{-}\eta^2\text{-XNCCF}_3$), X = H or D appeared as a doublet at -1.57 ppm. The disappearance of reactant was followed by ¹H NMR with the decreasing hydride peak at -11.49 ppm and the appearance of hydride peaks for **4** and **5** at -14.88 and -15.18 ppm, respectively. Kinetic plots are given as Figures 17-56 at the end of the experimental section. Fluorine-19 NMR data are given in Table 6 and ¹H NMR data are given in Table 7.

Preparation of H₂Os₃(CO)₁₀ + CF₃CN stock solution used in UV-Vis Kinetics:

The stock solution was prepared by transferring 55 ml of dried CDCl₃ to a flame dried Schlenck tube via trap-to-trap distillation. The Schlenck tube was then transported into the Braun dry box. H₂Os₃(CO)₁₀ (18.2 mg, 0.02007 mmol) was placed in an oven dried 50 ml volumetric flask and brought to volume by syringing in 50 ml of CDCl₃. The stock solution with a concentration of 0.4015 mmol/liter was stored in the dry box.

Kinetic run of H₂Os₃(CO)₁₀ + CF₃CN used in UV-Vis Kinetics:

Samples were prepared by syringing 2.5 ml of the stock solution into a oven dried quartz septum capped cuvette. The cuvette was placed in the spectrophotometer and allowed to reach temperature (25°C). The specially designed manometric vacuum manifold was used to deliver the gas, CF₃CN, only the stopcock permitting gas flow into an NMR tube was closed. The gas was monitored by the manometer and the gas flow was stopped when a pressure of 1 atmosphere was obtained. The gas was then syringed into the cuvette

and the reaction was monitored by the spectrophotometer. The kinetic experiments were performed at 25°C and only the volumes of gas were varied (volumes used were 1, 2, 4, 6, 8, and 10 ml). Each kinetic run was performed in duplicate to ensure repeatability and data agreement. The reactant, $(\mu\text{-H})_2\text{Os}_3(\text{CO})_{10}$ maximum absorption was at 552 nm, and both **4**, $(\mu\text{-H})\text{Os}_3(\text{CO})_{10}(\mu\text{-NC(H)CF}_3)$ and **5**, $(\mu\text{-H})\text{Os}_3(\text{CO})_{10}(\mu\text{-}\eta^2\text{-HNCCF}_3)$ absorbed at the same wavelength of 392 nm. Therefore, three wavelengths were used to monitor the reaction, 550, 552, and 554 nm. for the reactant and 390, 392, and 394 nm. for the two products. Kinetic plots are given as Figures 59-67 at the end of the experimental section.

Materials used in preparing **1, PPN[Ru₃(CO)₁₀($\mu\text{-NO}$)]:**

Compound **1**, and PPNCF₃CO₂ were prepared according to literature procedures.^{56,71} Trifluoroacetic acid, triflic acid, trifluoroacetic acid-d, triflic acid-d, and methylene chloride-d₂ were purchased from Aldrich Chemicals and used as received. Methylene chloride was distilled from calcium hydride and stored in a Braun Basic System MB 150 dry box. Ru₃(CO)₁₂ was enriched by exposing 0.5 g in 250 ml of heptane to 0.5 atm of 90% ¹³C (Monsanto) at 80-90°C for 2 days.

Spectra

¹H and ¹³C NMR spectra were obtained on a Varian Unity Plus 400 MHz spectrometer at 400 and 100 MHz, respectively.

Sample preparation and monitoring procedures:

¹³C-enriched samples of **1** (40-50 mg) were dissolved in a 2.5 ml solution containing

a 1:4 mixture of $\text{CD}_2\text{Cl}_2/\text{CH}_2\text{Cl}_2$ in a 5 or 10 mm J.S. Young resealable NMR tube. Under an inert atmosphere inside a Braun dry box at ambient temperature, the sample was injected with a 1 eq. of $\text{CF}_3\text{SO}_3\text{X}$ ($\text{X}=\text{H}$ or D). The tubes containing the samples were then placed in the NMR spectrometer where ^1H or ^{13}C NMR spectra of **2** were obtained at various temperatures (-80 to 25°C).

In another experiment, a sample was prepared in a septum capped 10 mm NMR tube. This tube was placed in the NMR spectrometer and cooled to -80°C . After reaching the desired temperature, the tube was removed and quickly injected with 0.4 eq. of $\text{PPNCF}_3\text{CO}_2$, inverted once and reinserted back into the NMR spectrometer at -80°C . Spectra were then recorded at the following temperatures: -80 , -50 , -20 , $+10$, and $+25^\circ\text{C}$. Temperature equilibration times were 15 minutes and accumulation times were set at 7 minutes. Conversion of **2** to **3** was not observed until a temperature of 10°C was reached. The rate of conversion of **2** to **3** showed no difference regardless of which sample was used, protonated or deuterated. However, conversion to **3** was instantaneous at ambient temperature when $\text{PPNCF}_3\text{CO}_2$ was injected into a solution of **2**.

Samples of **1**, prepared in a septum capped 10 mm NMR tube were placed in the NMR spectrometer and cooled to -80°C . The tube was removed and quickly injected with 1 eq. of $\text{CF}_3\text{CO}_2\text{X}$ ($\text{X}=\text{H}$ or D), inverted once and reinserted back into the NMR spectrometer at -80°C . Spectra were then recorded at the following temperatures: -80 , -50 , -20 , $+10$, and $+25^\circ\text{C}$. Conversion of **2** to **3** was again not observed until a temperature of 10°C was reached. Also, no difference in the rate of conversion was observed between the protonated or deuterated cases. Protonation of **1** with $\text{CF}_3\text{CO}_2\text{X}$ ($\text{X}=\text{H}$ or D) at ambient temperature converts directly to **3** as previously reported.⁵⁶

Table 6: Fluorine-19 NMR data for 4, ($\mu\text{-H}$)Os₃(CO)₁₀($\mu\text{-NC(H)CF}_3$) and 5, ($\mu\text{-H}$)Os₃(CO)₁₀($\mu\text{-}\eta^2\text{-HNCCF}_3$).

Complex	¹⁹ F NMR spectrum (δ , ppm) ^a
<u>4</u>	4.86 (d), ³ J (FCH) = 4.5 Hz, ⁵ J (FOsH) = 0.7 Hz ⁵⁴
<u>5</u>	-1.57 (d), ⁴ J (FH) = 2 Hz ⁵⁴

^a At field relative to CF₃COOH ; s = singlet, d = doublet.

Table 7: ¹H NMR data for 4, ($\mu\text{-H}$)Os₃(CO)₁₀($\mu\text{-NC(H)CF}_3$) and 5, ($\mu\text{-H}$)Os₃(CO)₁₀($\mu\text{-}\eta^2\text{-HNCCF}_3$) and the starting complex, H₂Os₃(CO)₁₀.

Complex	¹ H NMR spectrum (δ , ppm) ^a
<u>4</u>	7.75 (q , 1 H), ³ J (HF) = 4.2 Hz ⁵² -14.88 (s , 1 H)
<u>5</u>	9.70 (s , 1 H) -15.18 (s , 1 H)
<u>SC</u>	-11.49 (s , 1 H)

^a At field relative to CDCl₃; s = singlet, q = quartet.

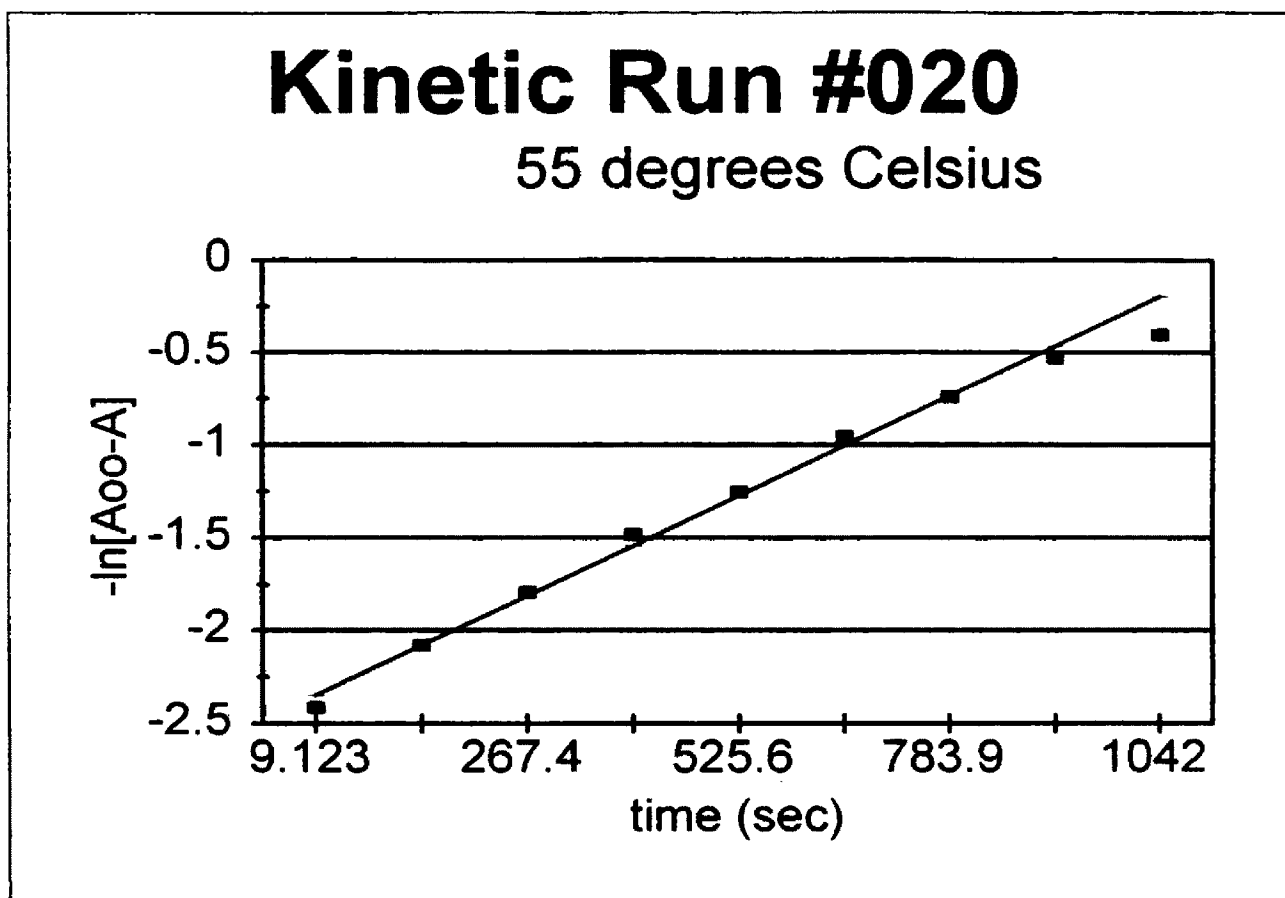
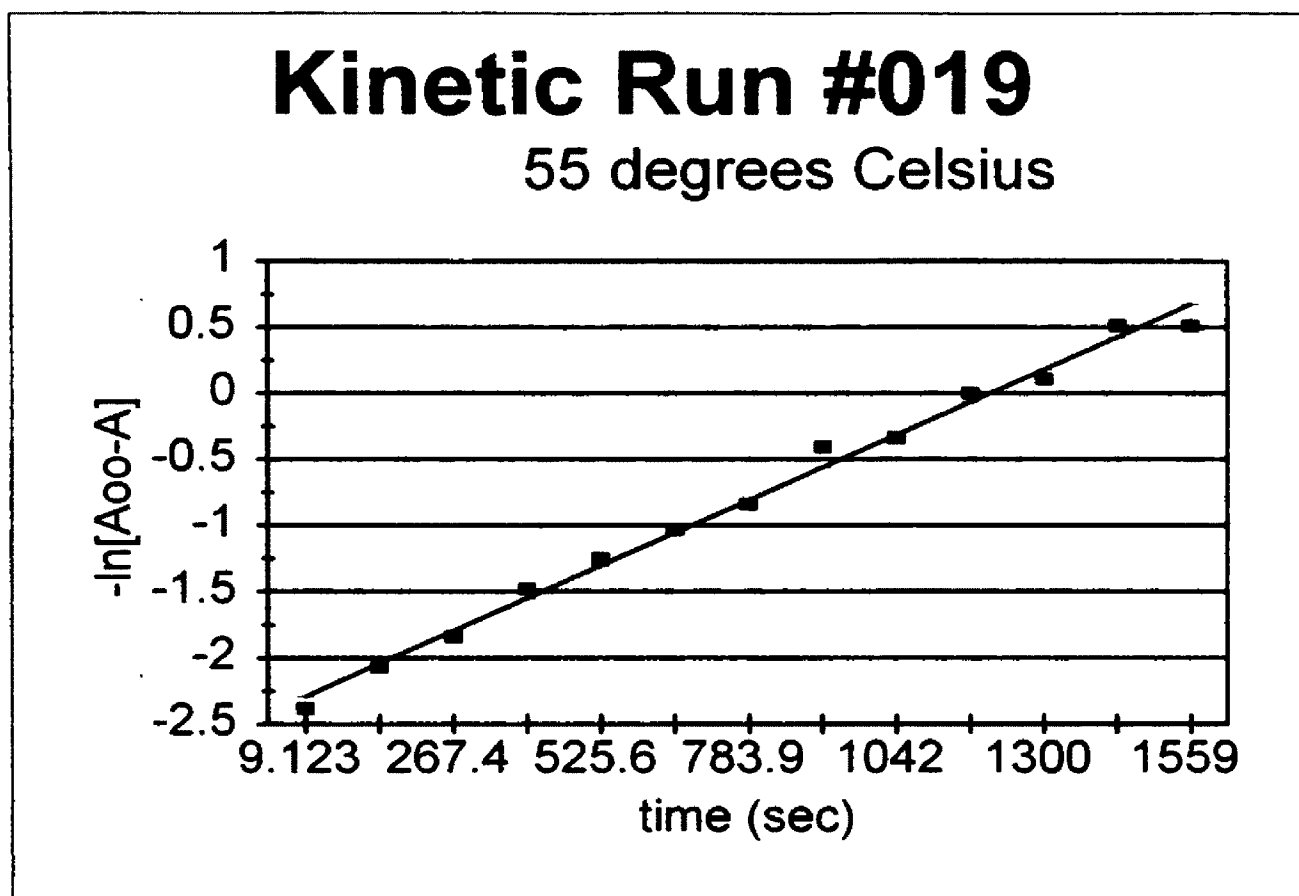
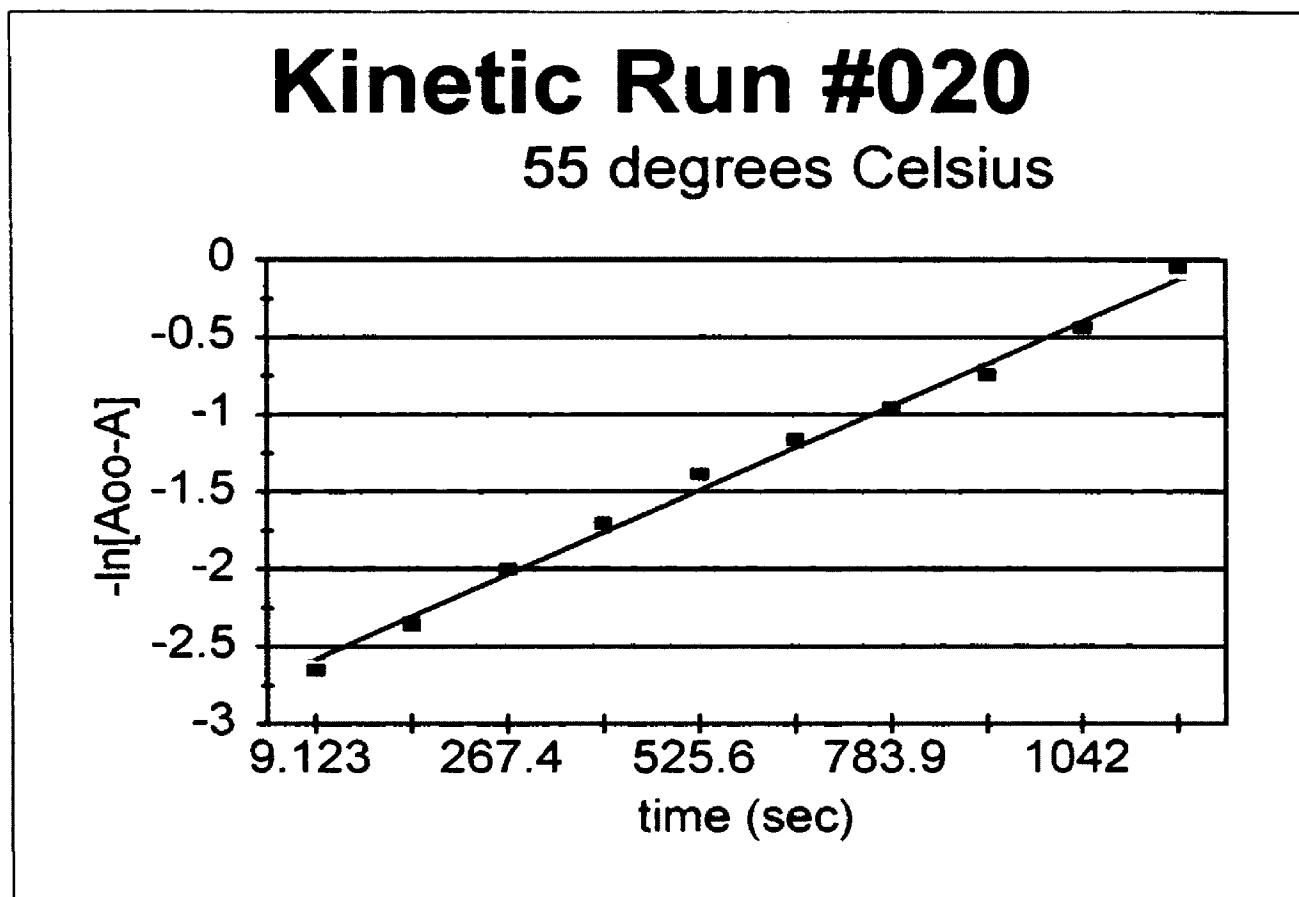


Figure 17: Kinetic plot of the formation of 4, ($\mu\text{-H}$)Os₃(CO)₁₀ ($\mu\text{-NC(H)CF}_3$) at 55°C.



**Figure 18: Kinetic plot of the formation of $4, (\mu\text{-H})\text{Os}_3(\text{CO})_{10}$
 $(\mu\text{-NC(H)CF}_3)$ at 55°C.**



**Figure 19: Kinetic plot of the formation of $\mathbf{5}$, $(\mu\text{-H})\text{Os}_3(\text{CO})_{10}$
 $(\mu\text{-}\eta^2\text{-NC(H)CF}_3)$ at 55°C.**

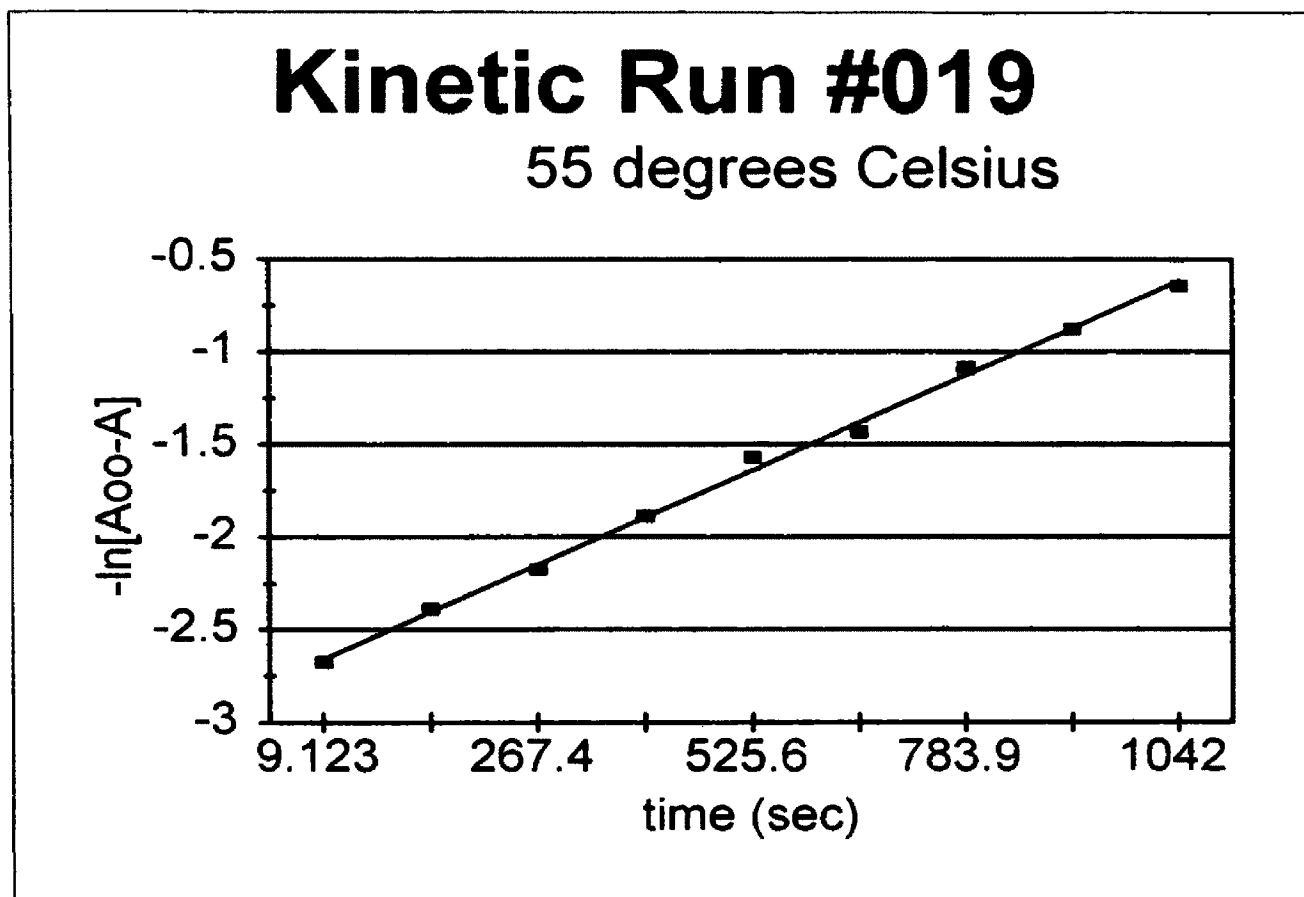


**Figure 20: Kinetic plot of the formation of $\mathbf{5}$, $(\mu\text{-H})\text{Os}_3(\text{CO})_{10}$
 $(\mu\text{-}\eta^2\text{-HNCCF}_3)$ at 55°C.**

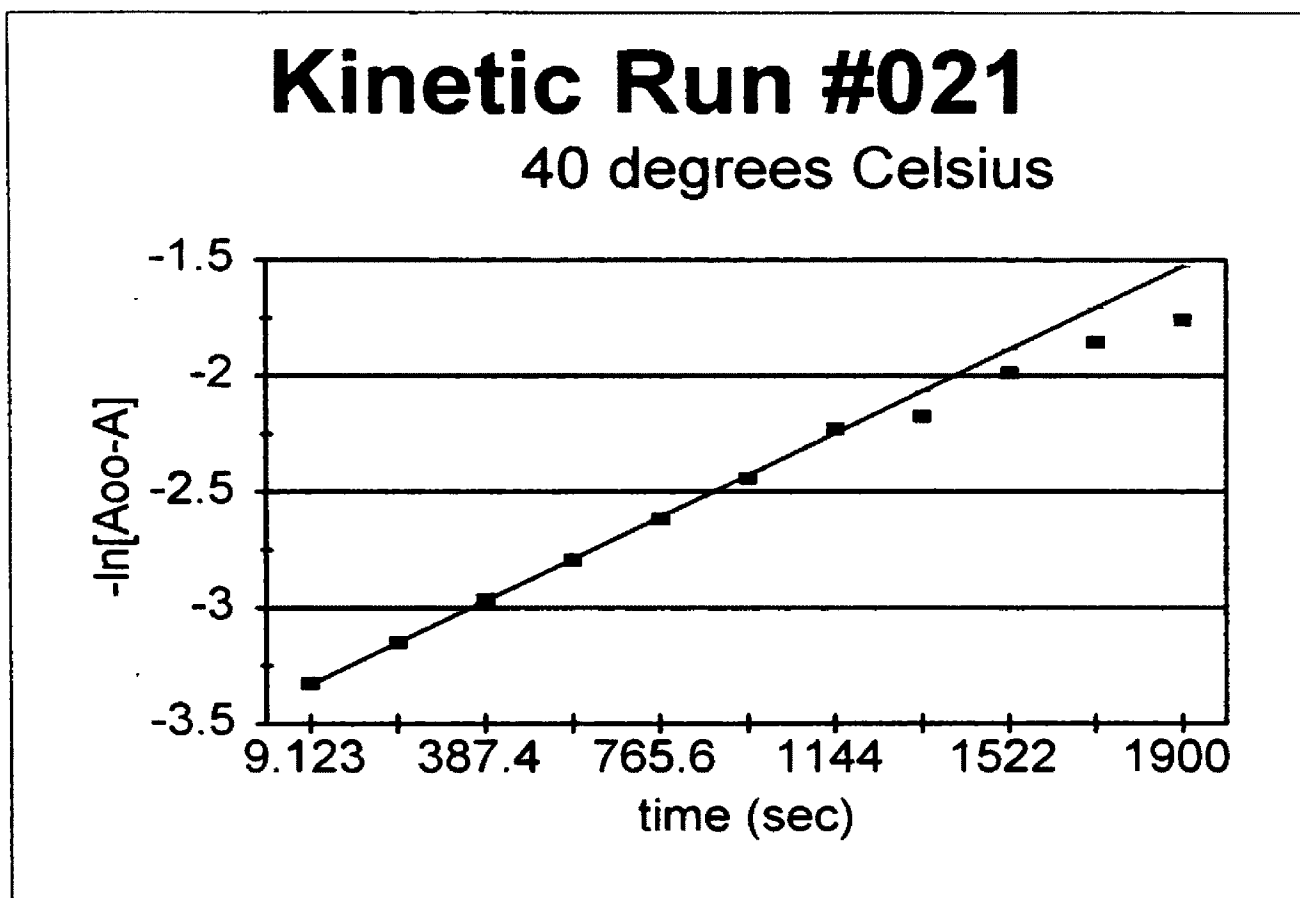


Figure 21: Kinetic plot of the formation of $4, (\mu\text{-H})\text{Os}_3(\text{CO})_{10}$ ($\mu\text{-NC(H)CF}_3$) at 40°C.

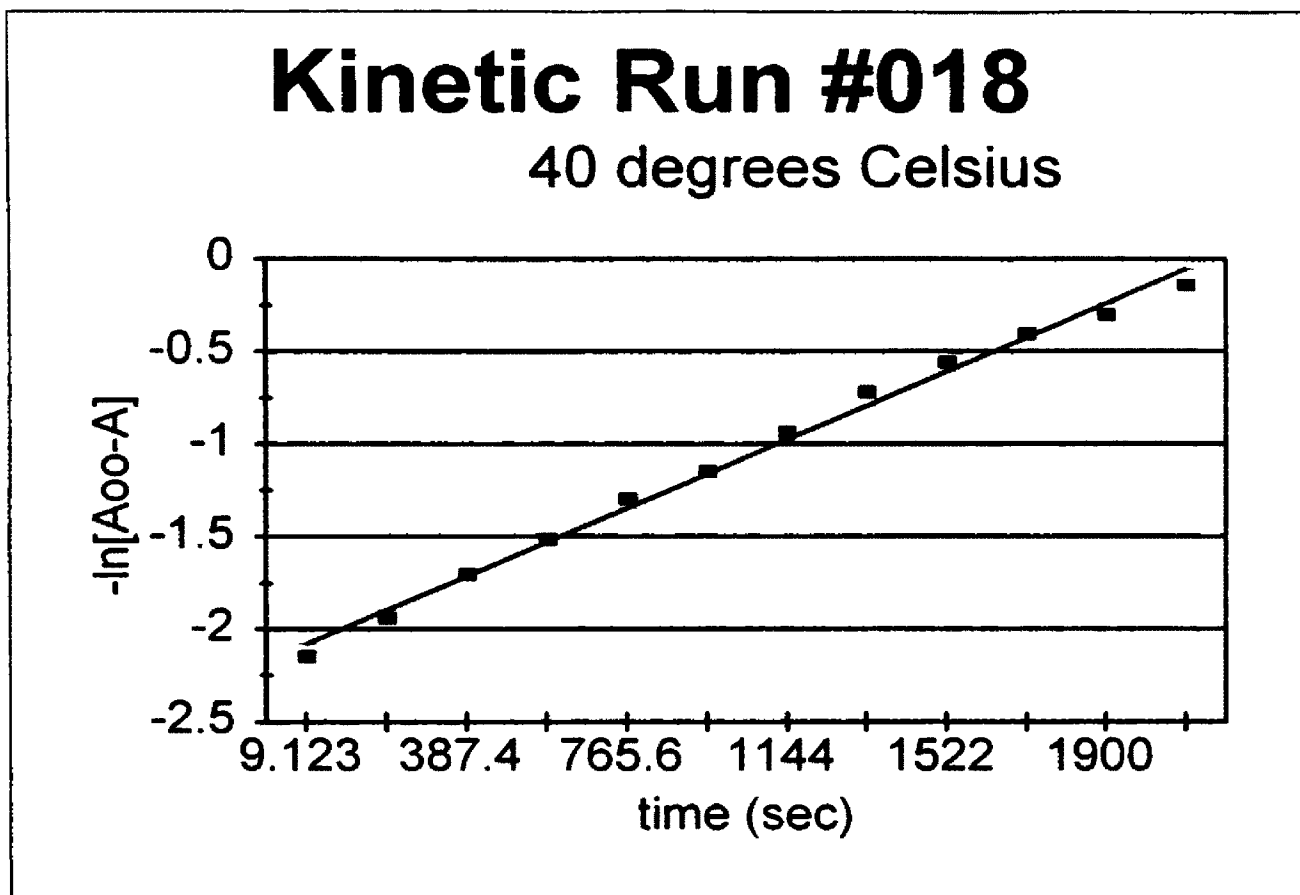


Figure 22: Kinetic plot of the formation of 4, (μ -H)Os₃(CO)₁₀ (μ -NC(H)CF₃) at 40°C.

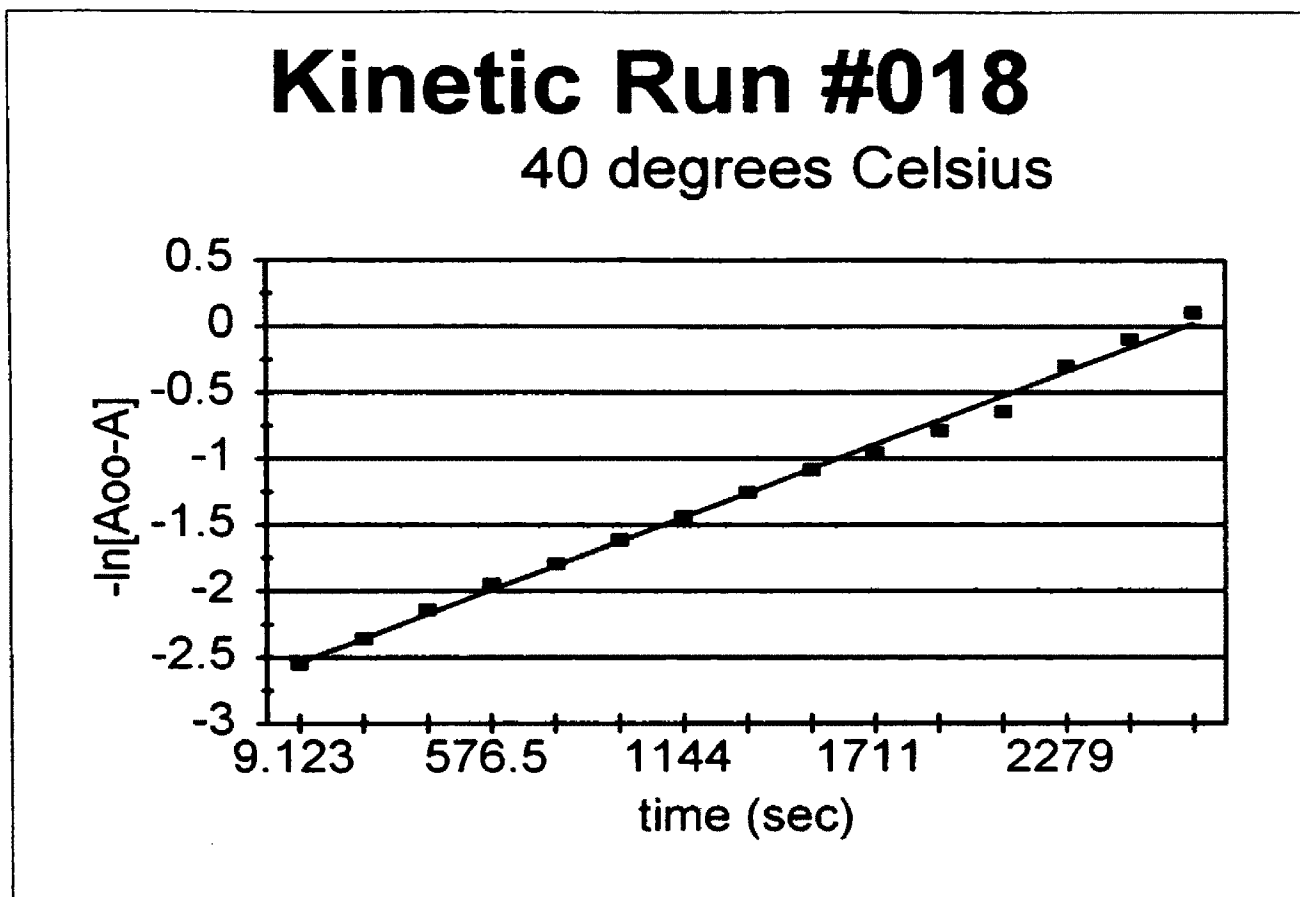
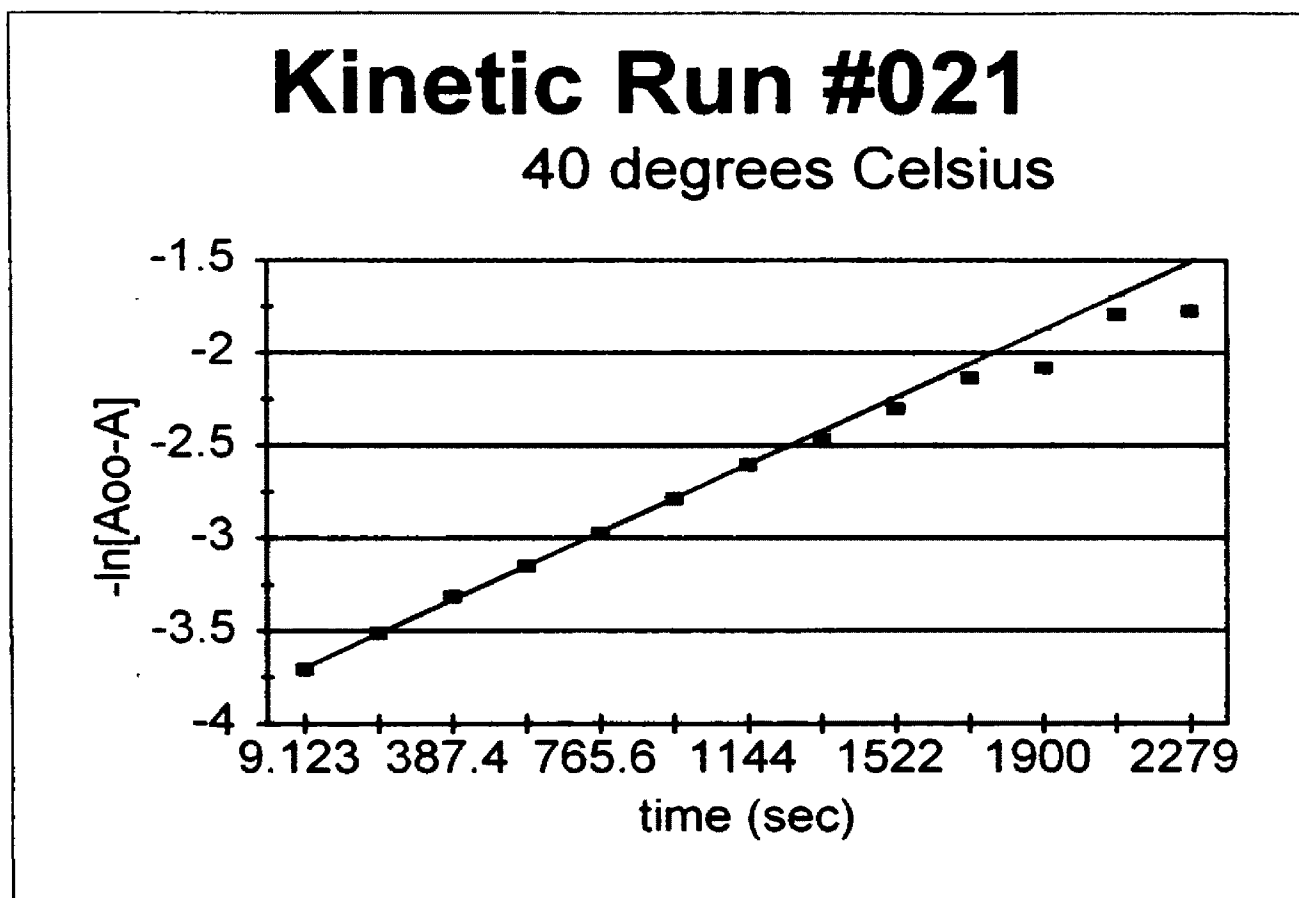


Figure 23: Kinetic plot of the formation of $\underline{5}$, $(\mu\text{-H})\text{Os}_3(\text{CO})_{10}$ ($\mu\text{-}\eta^2\text{-HNCCF}_3$) at 40°C.



**Figure 24: Kinetic plot of the formation of $\underline{5}$, $(\mu\text{-H})\text{Os}_3(\text{CO})_{10}$
 $(\mu\text{-}\eta^2\text{-HNCCF}_3)$ at 40°C.**

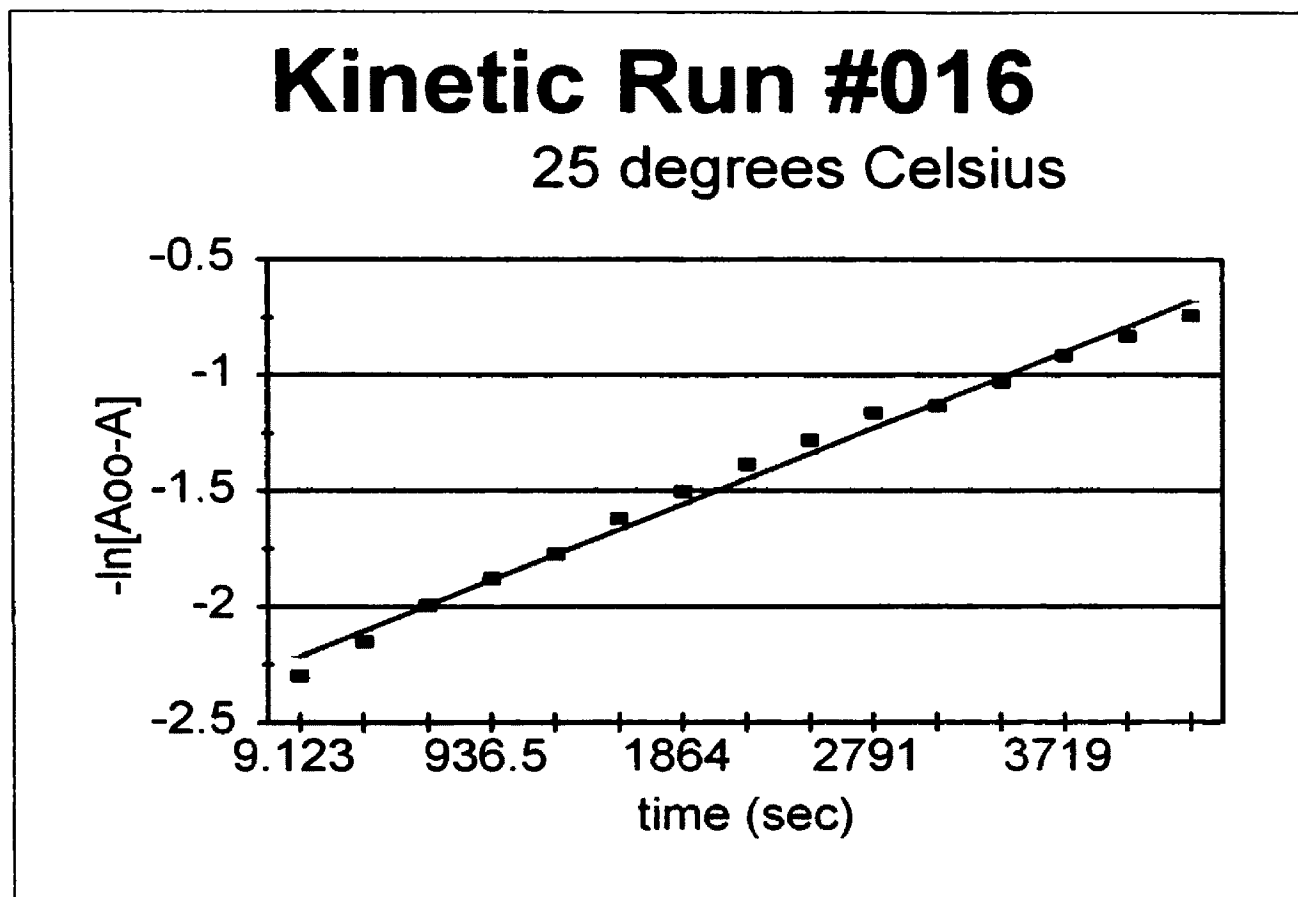


Figure 25: Kinetic plot of the formation of 4, (μ -H)Os₃(CO)₁₀ (μ -NC(H)CF₃) at 25 °C.

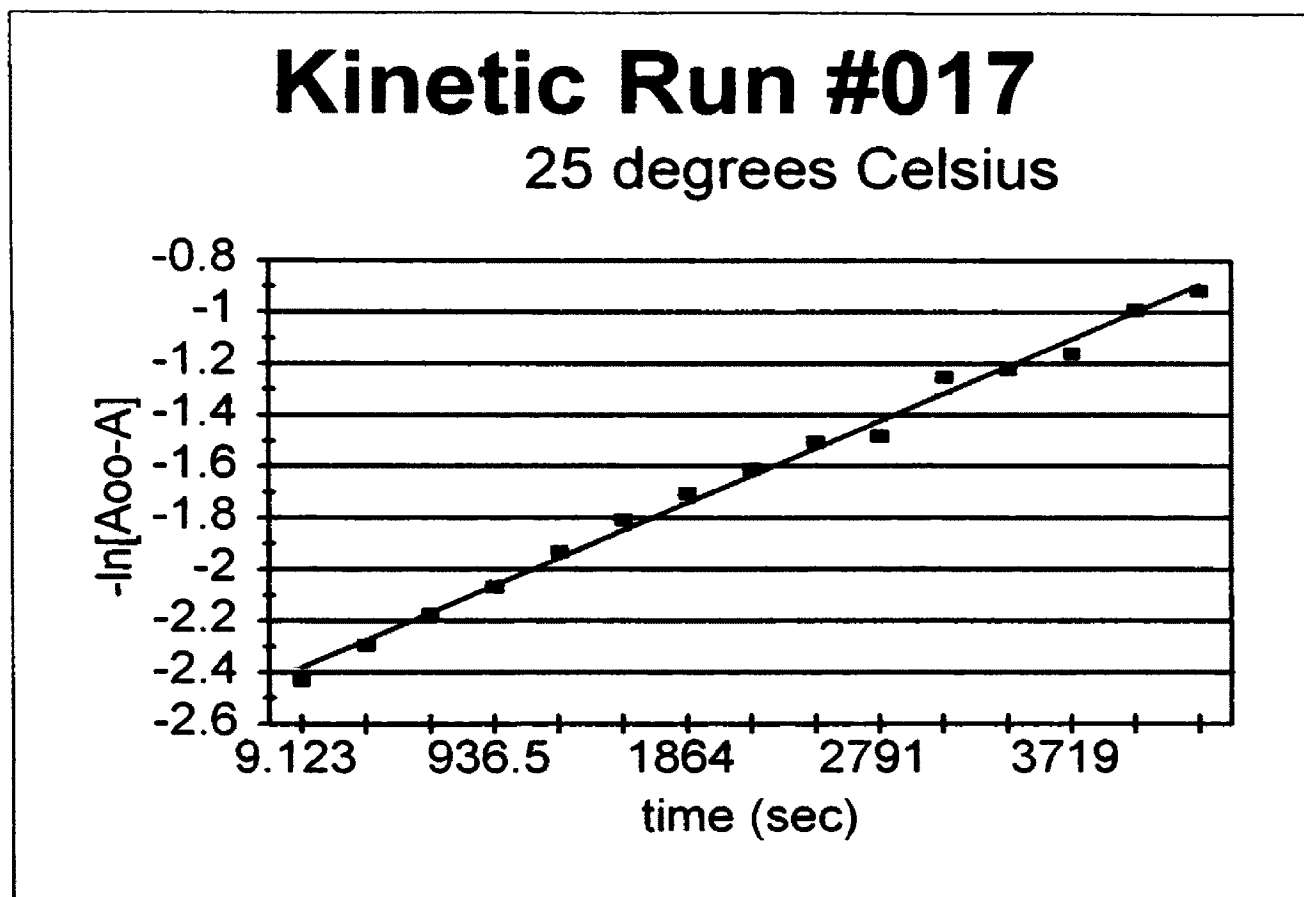
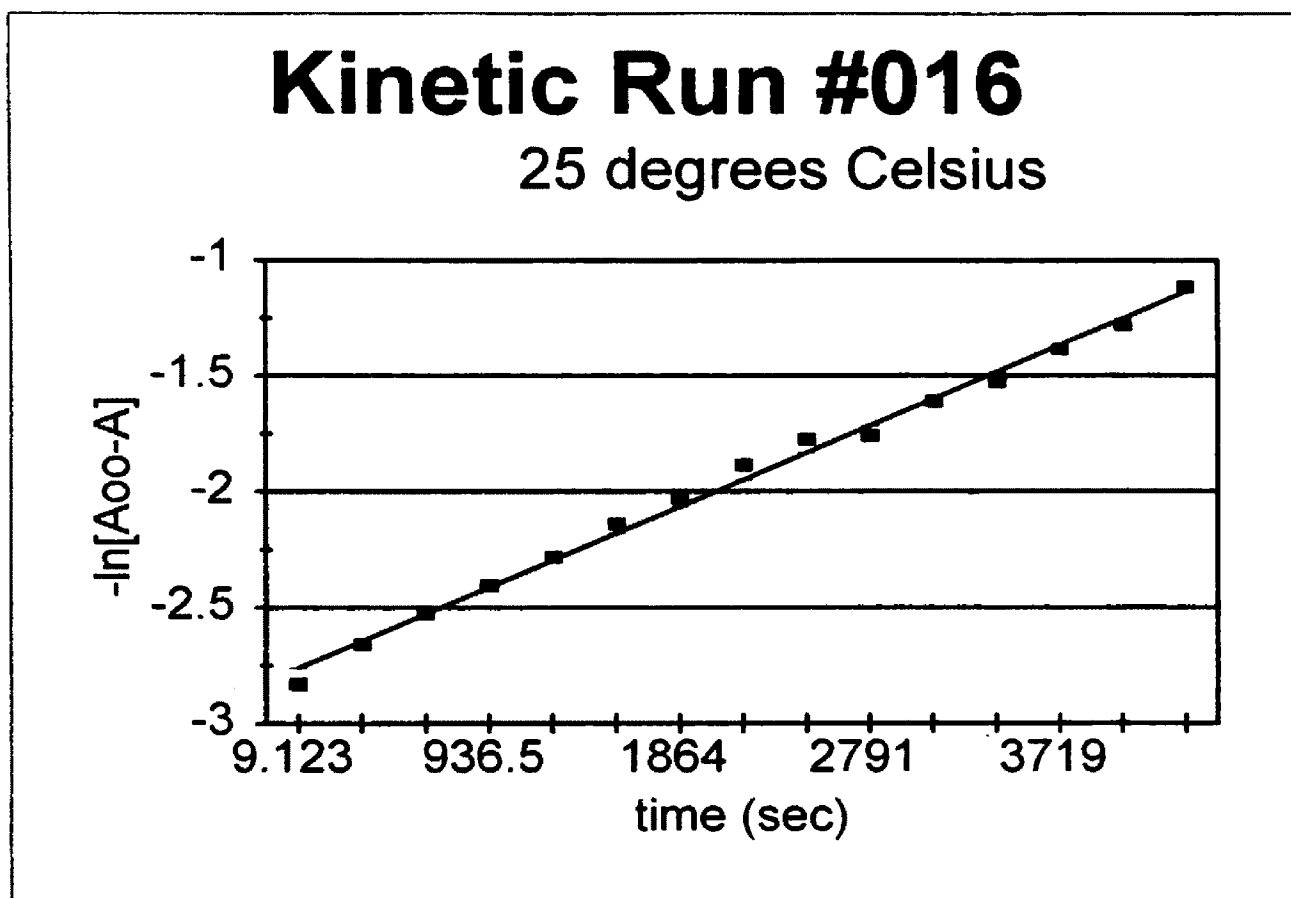
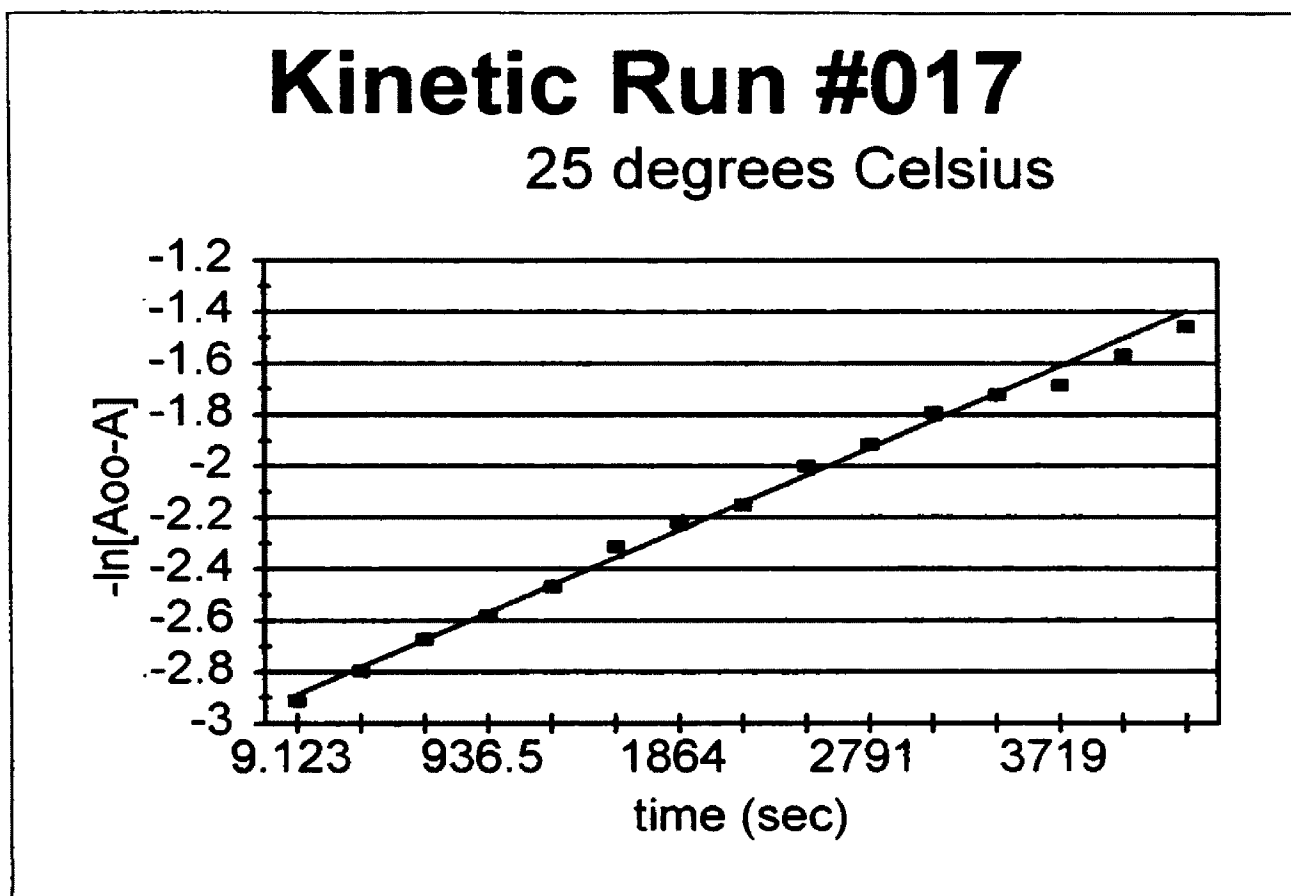


Figure 26: Kinetic plot of the formation of 4, ($\mu\text{-H}$)Os₃(CO)₁₀ ($\mu\text{-NC(H)CF}_3$) at 25°C.



**Figure 27: Kinetic plot of the formation of $\mathbf{5}$, $(\mu\text{-H})\text{Os}_3(\text{CO})_{10}$
 $(\mu\text{-}\eta^2\text{-HNC}\text{CF}_3)$ at 25°C.**



**Figure 28: Kinetic plot of the formation of 5, $(\mu\text{-H})\text{Os}_3(\text{CO})_{10}$
 $(\mu\text{-}\eta^2\text{-HNCCF}_3)$ at 25°C.**

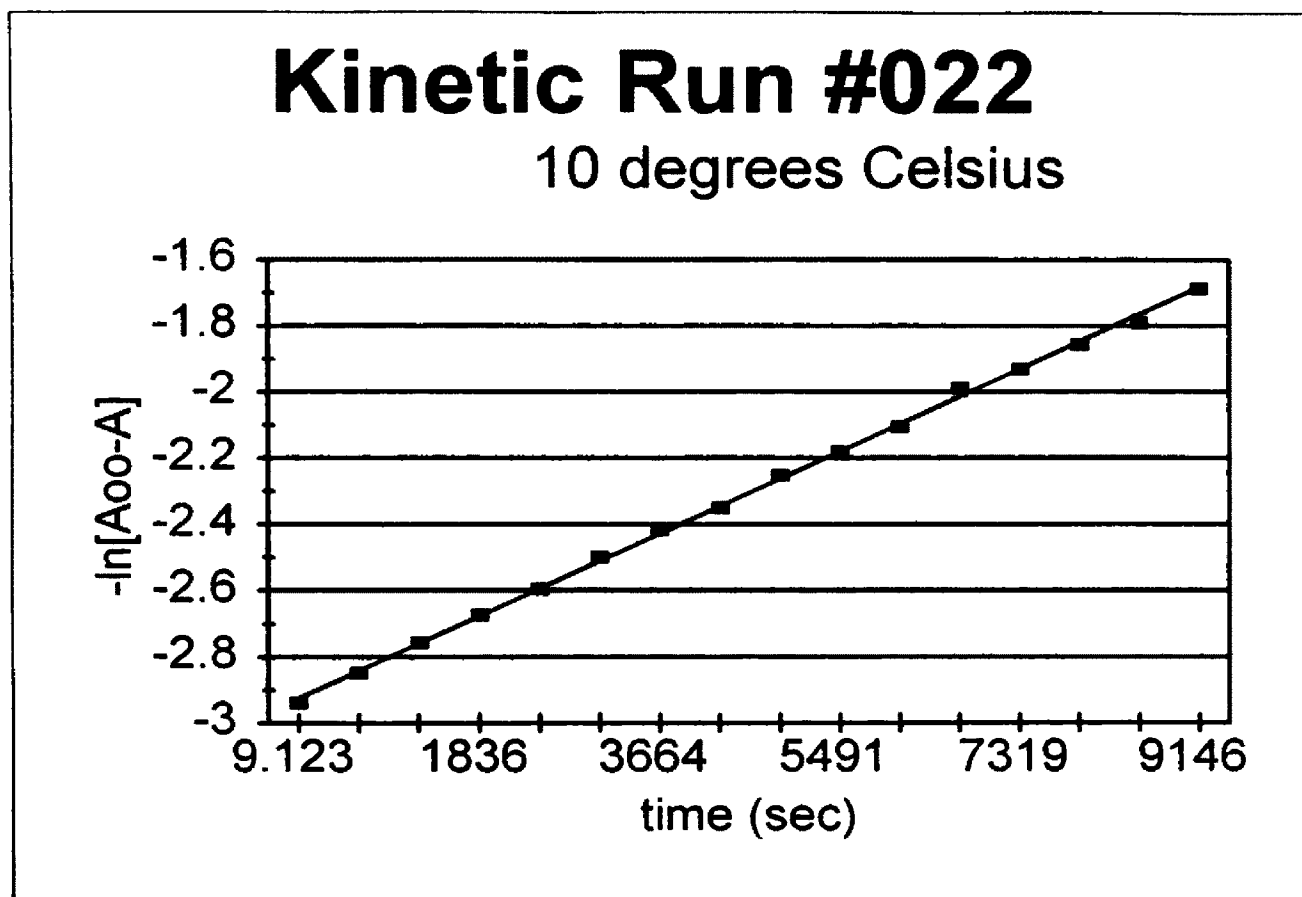


Figure 29: Kinetic plot of the formation of 4, ($\mu\text{-H}$)Os₃(CO)₁₀ ($\mu\text{-NC(H)CF}_3$) at 10°C.

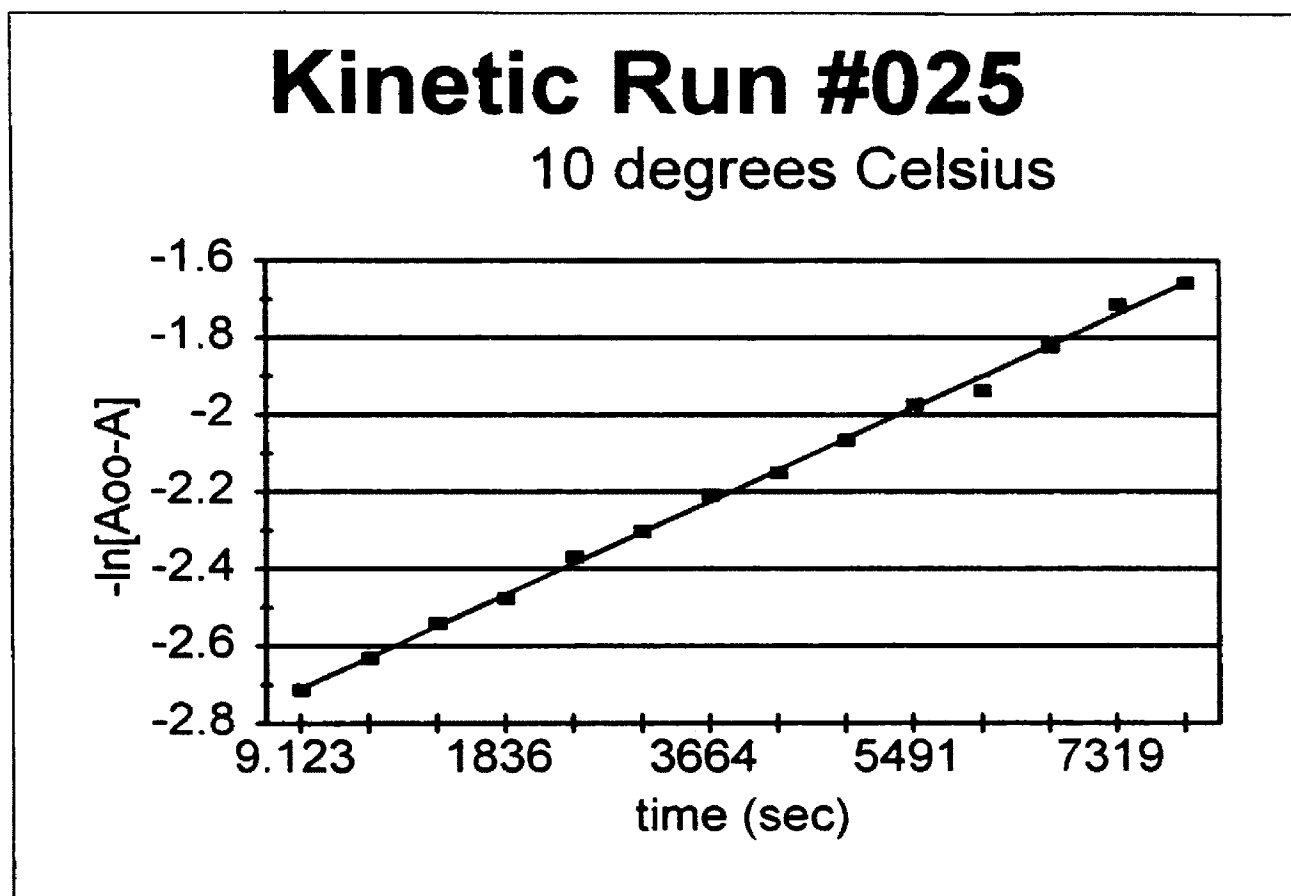
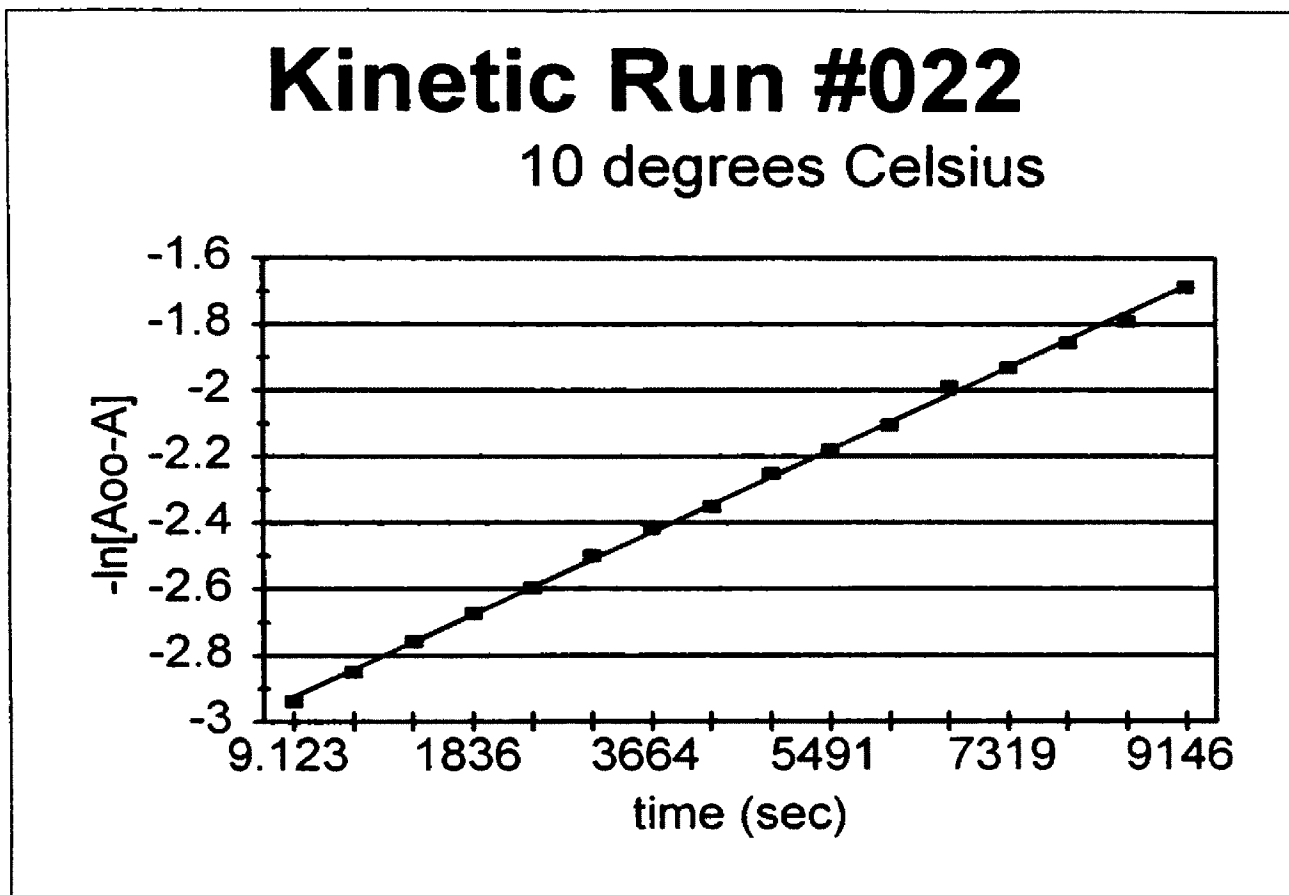
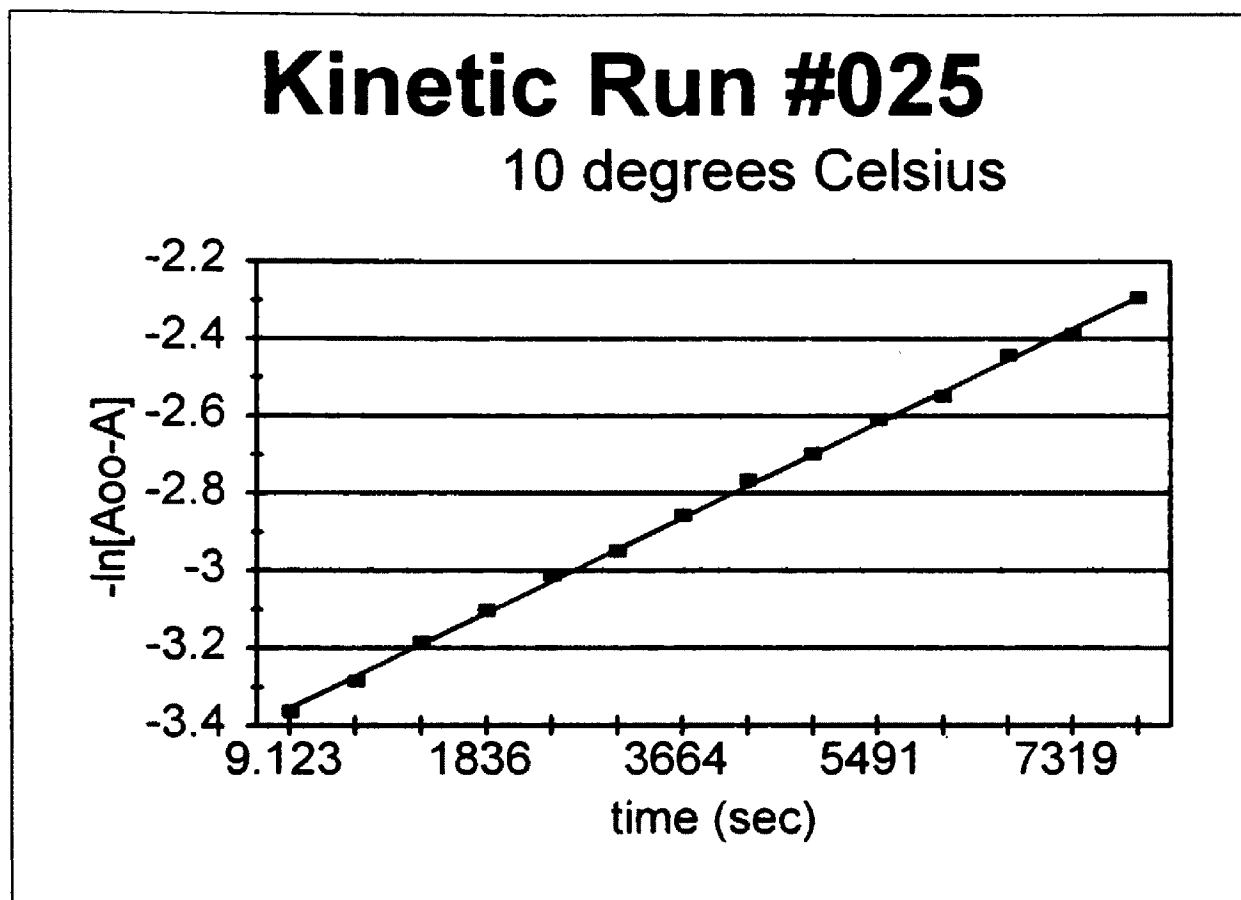


Figure 30: Kinetic plot of the formation of 4, (μ -H)Os₃(CO)₁₀ (μ -NC(H)CF₃) at 10°C.



**Figure 31: Kinetic plot of the formation of $\mathbf{5}$, $(\mu\text{-H})\text{Os}_3(\text{CO})_{10}$
 $(\mu\text{-}\eta^2\text{-HNCF}_3)$ at 10°C .**



**Figure 32: Kinetic plot of the formation of $\mathbf{5}$, $(\mu\text{-H})\text{Os}_3(\text{CO})_{10}$
 $(\mu\text{-}\eta^2\text{-HNCCF}_3)$ at 10°C .**

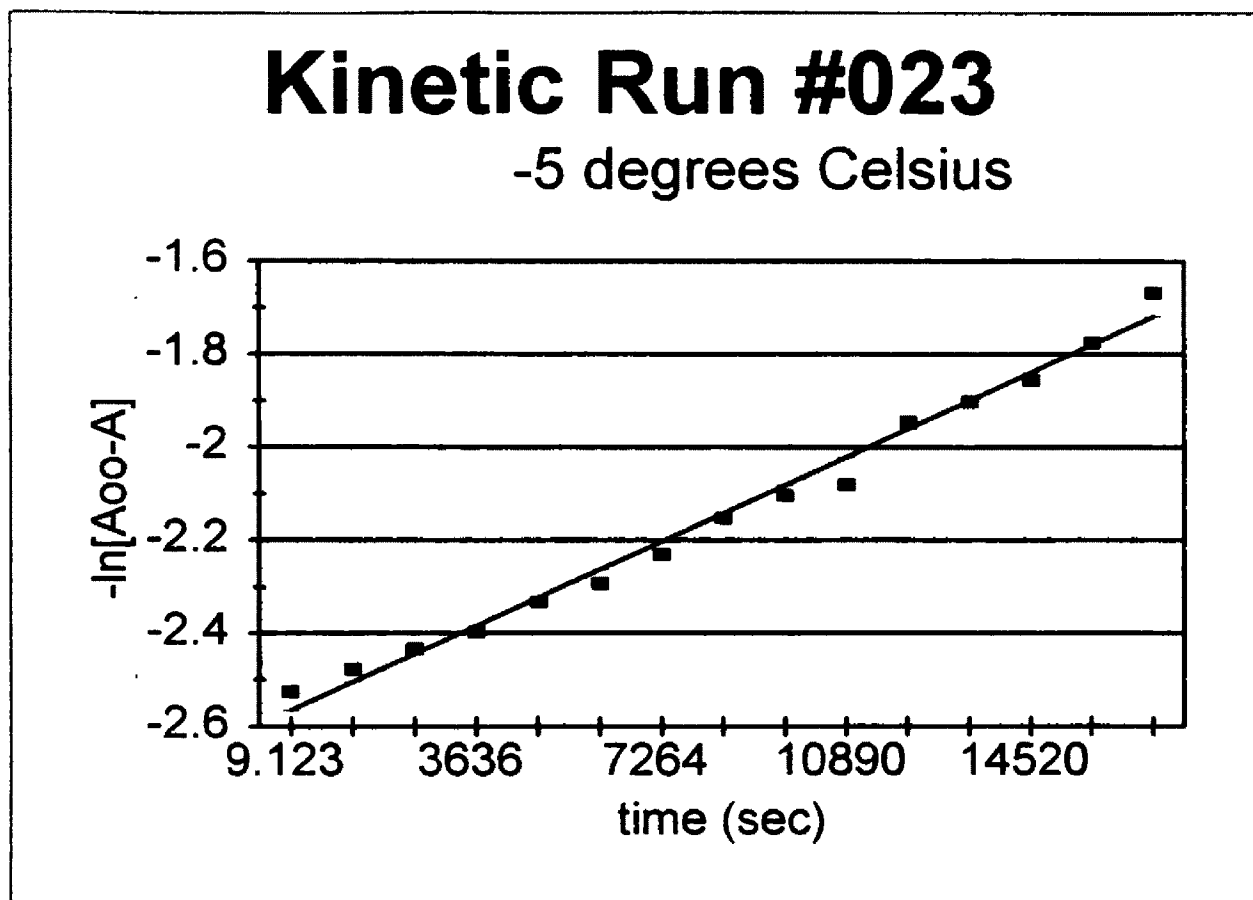


Figure 33: Kinetic plot of the formation of 4, ($\mu\text{-H}$)Os₃(CO)₁₀ ($\mu\text{-NC(H)CF}_3$) at -5°C .

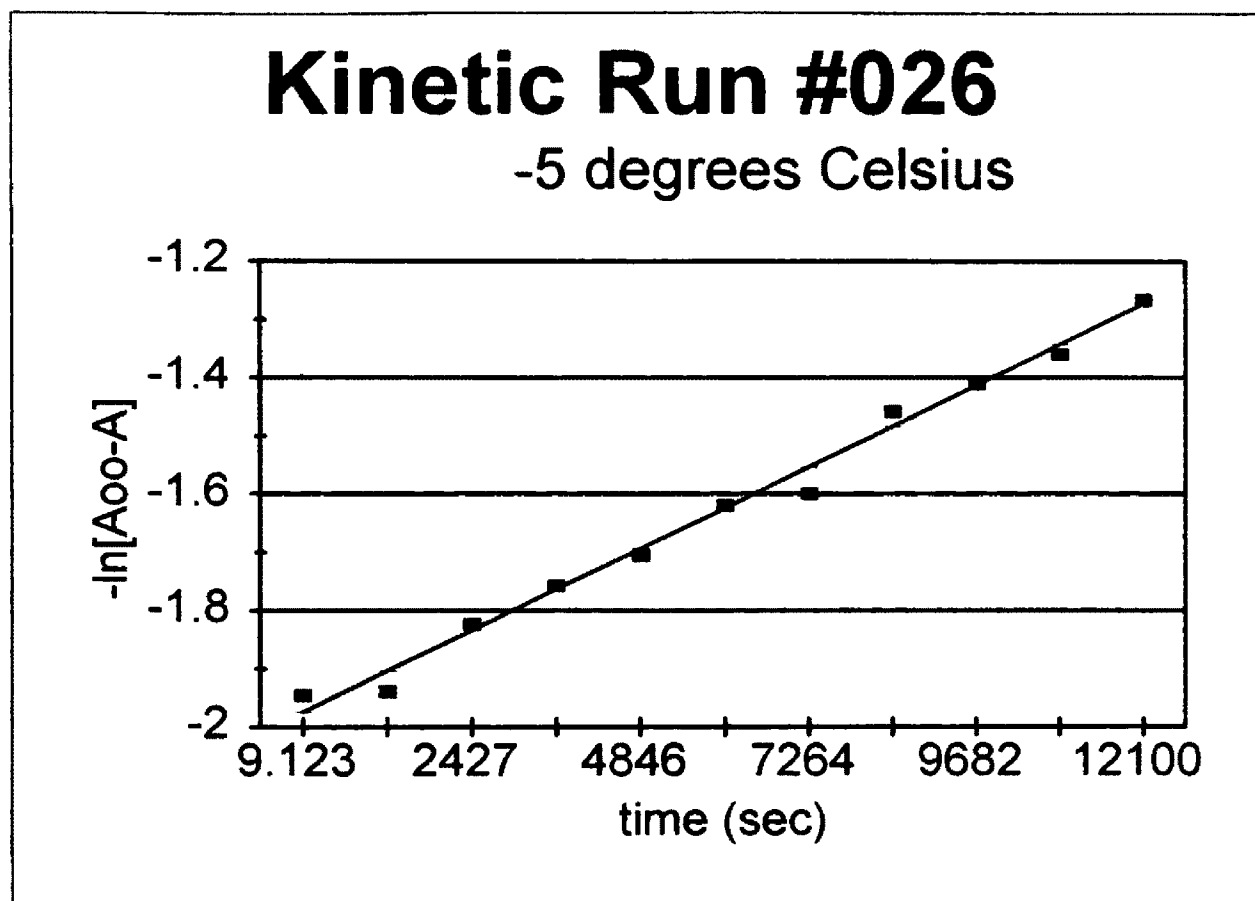


Figure 34: Kinetic plot of the formation of 4, ($\mu\text{-H}$)Os₃(CO)₁₀ ($\mu\text{-NC(H)CF}_3$) at -5°C.

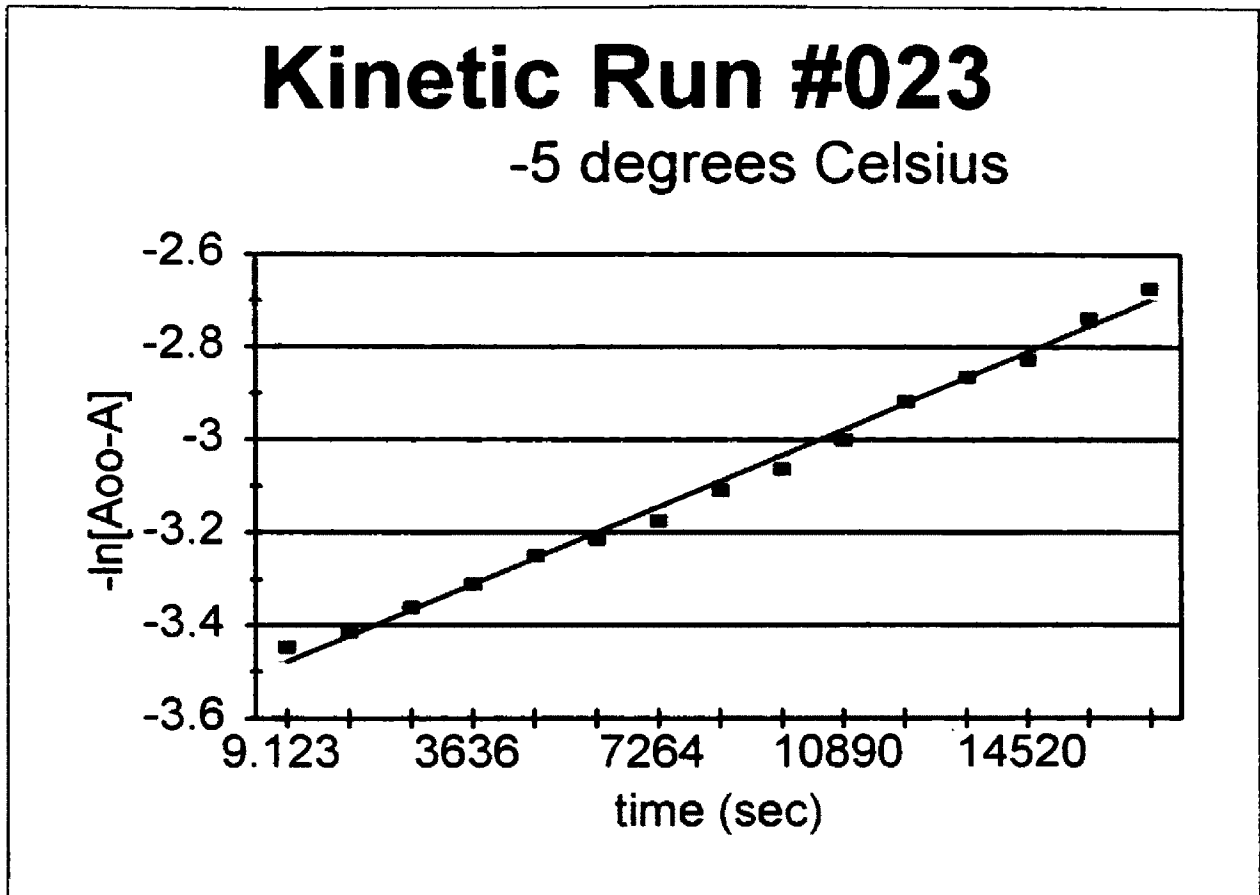


Figure 35: Kinetic plot of the formation of 5, (μ -H) $\text{Os}_3(\text{CO})_{10}$ (μ - η^2 -HNCCF₃) at -5°C.

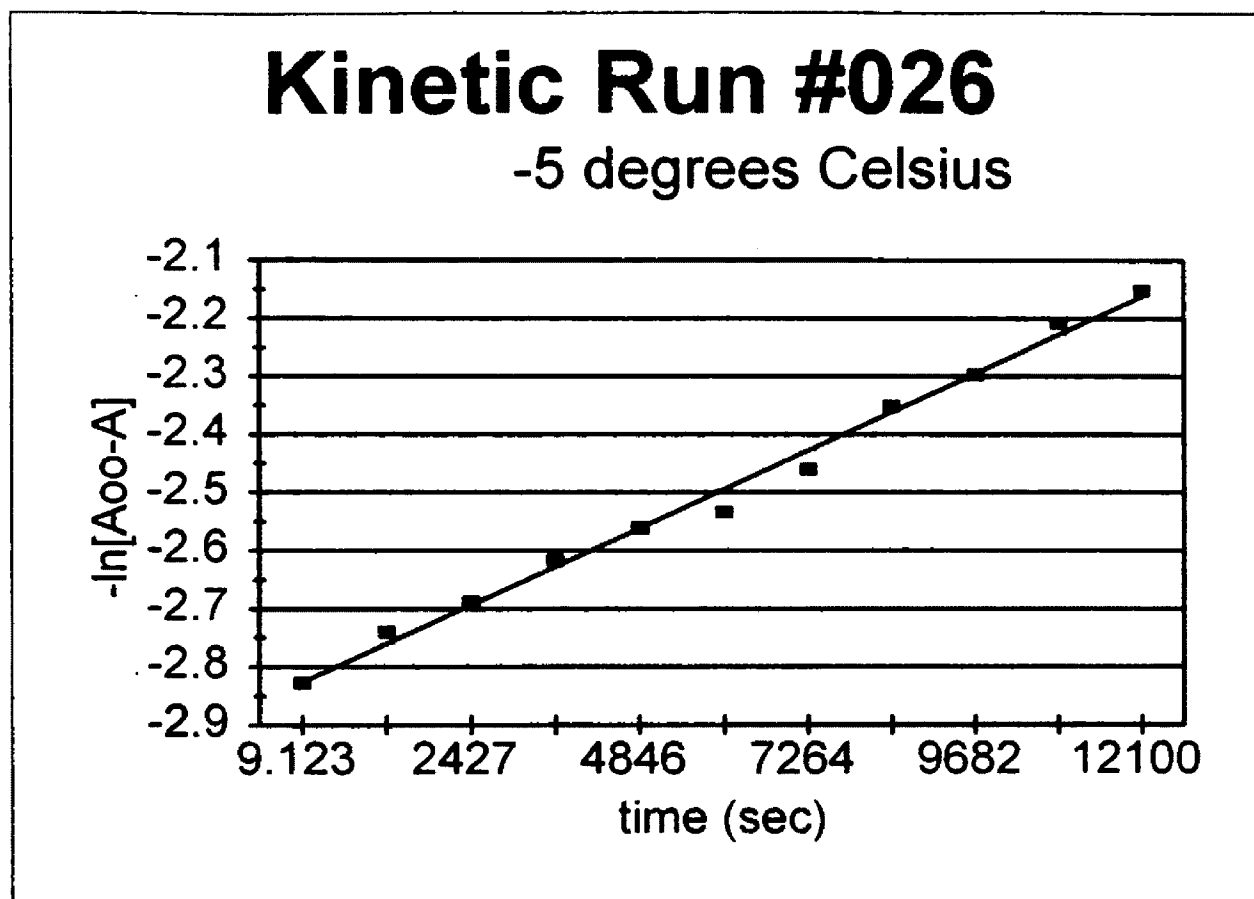


Figure 36: Kinetic plot of the formation of 5, ($\mu\text{-H}$)Os₃(CO)₁₀ ($\mu\text{-}\eta^2\text{-HNCCF}_3$) at -5°C .

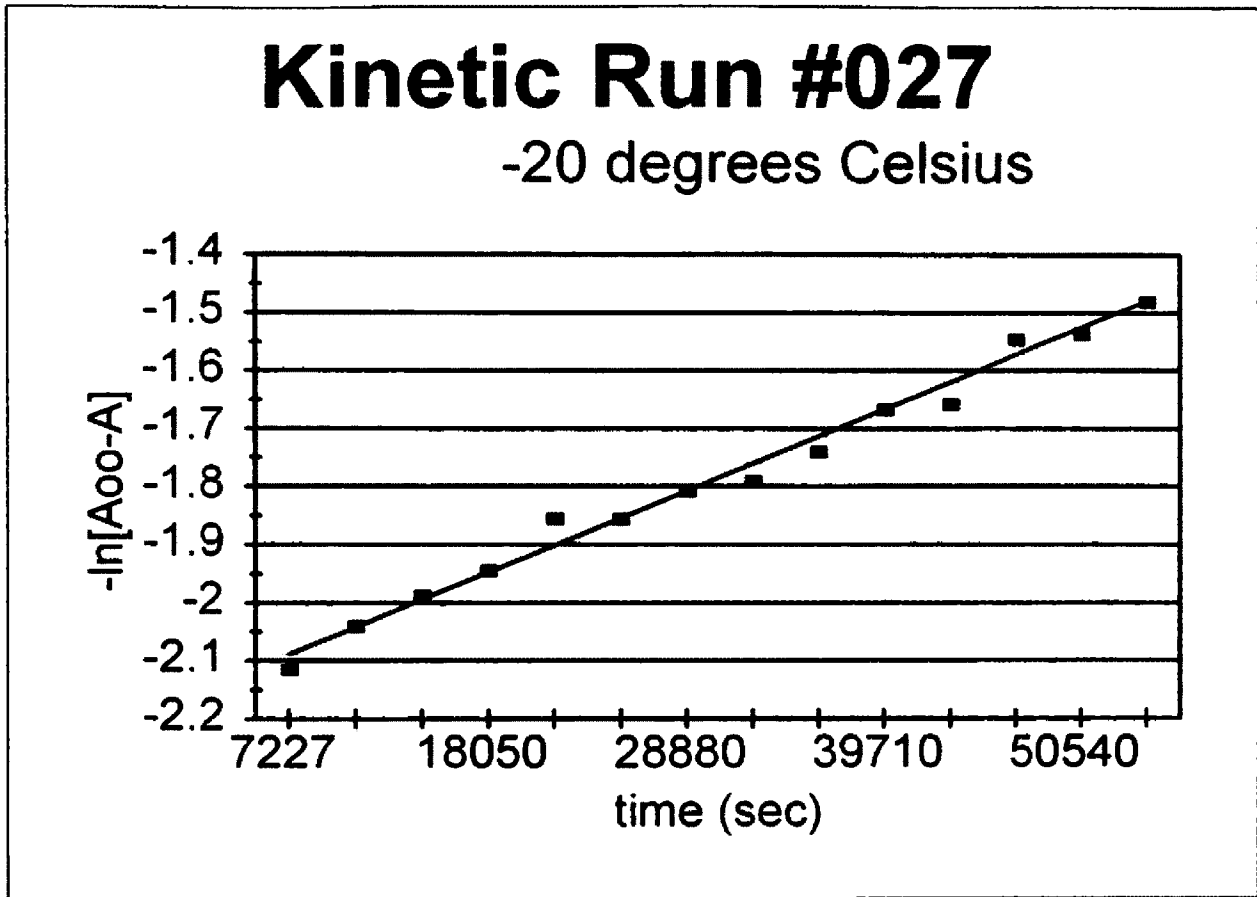


Figure 37: Kinetic plot of the formation of $\mathbf{4}$, $(\mu\text{-H})\text{Os}_3(\text{CO})_{10}$ ($\mu\text{-NC(H)CF}_3$) at -20°C .

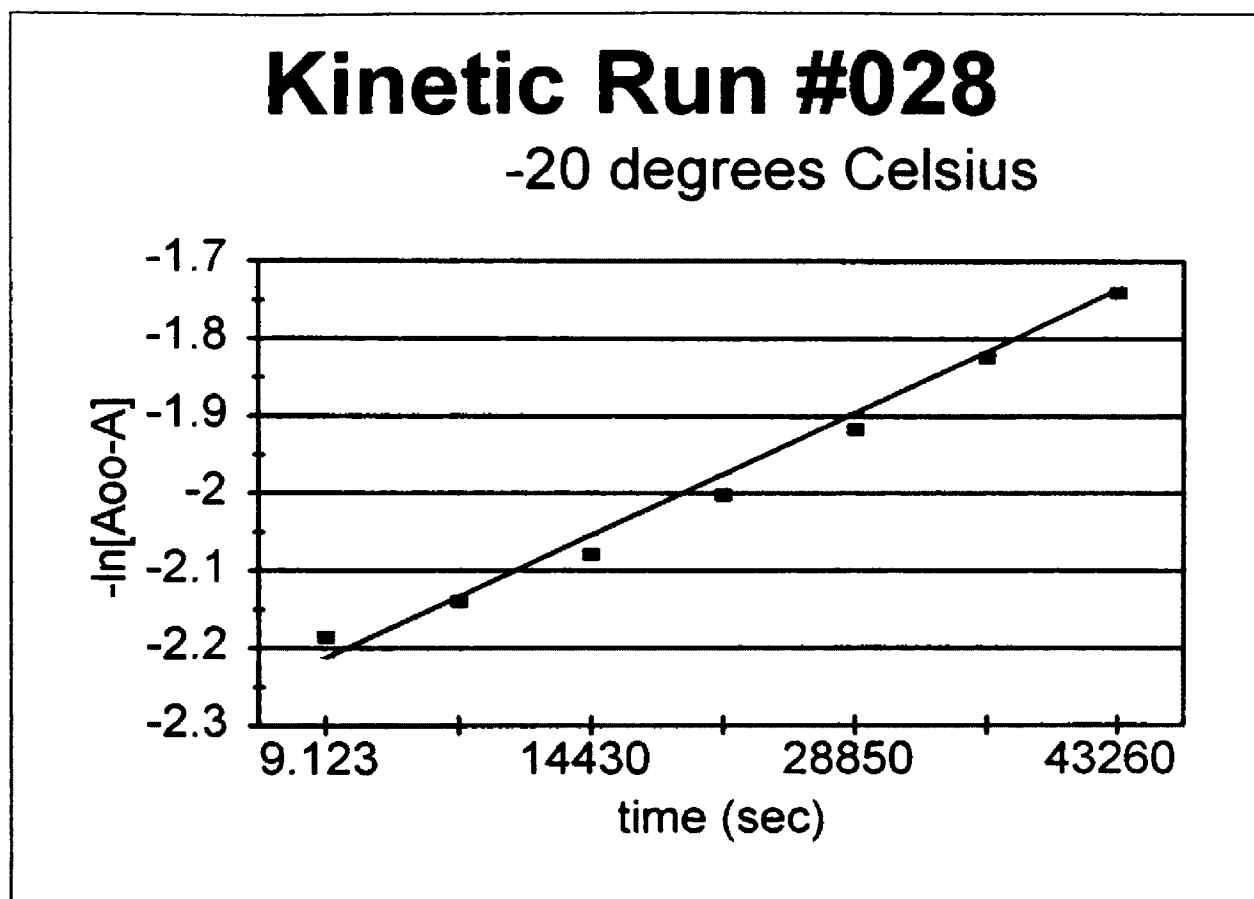


Figure 38: Kinetic plot of the formation of 4, (μ -H)Os₃(CO)₁₀ (μ -NC(H)CF₃) at -20°C.

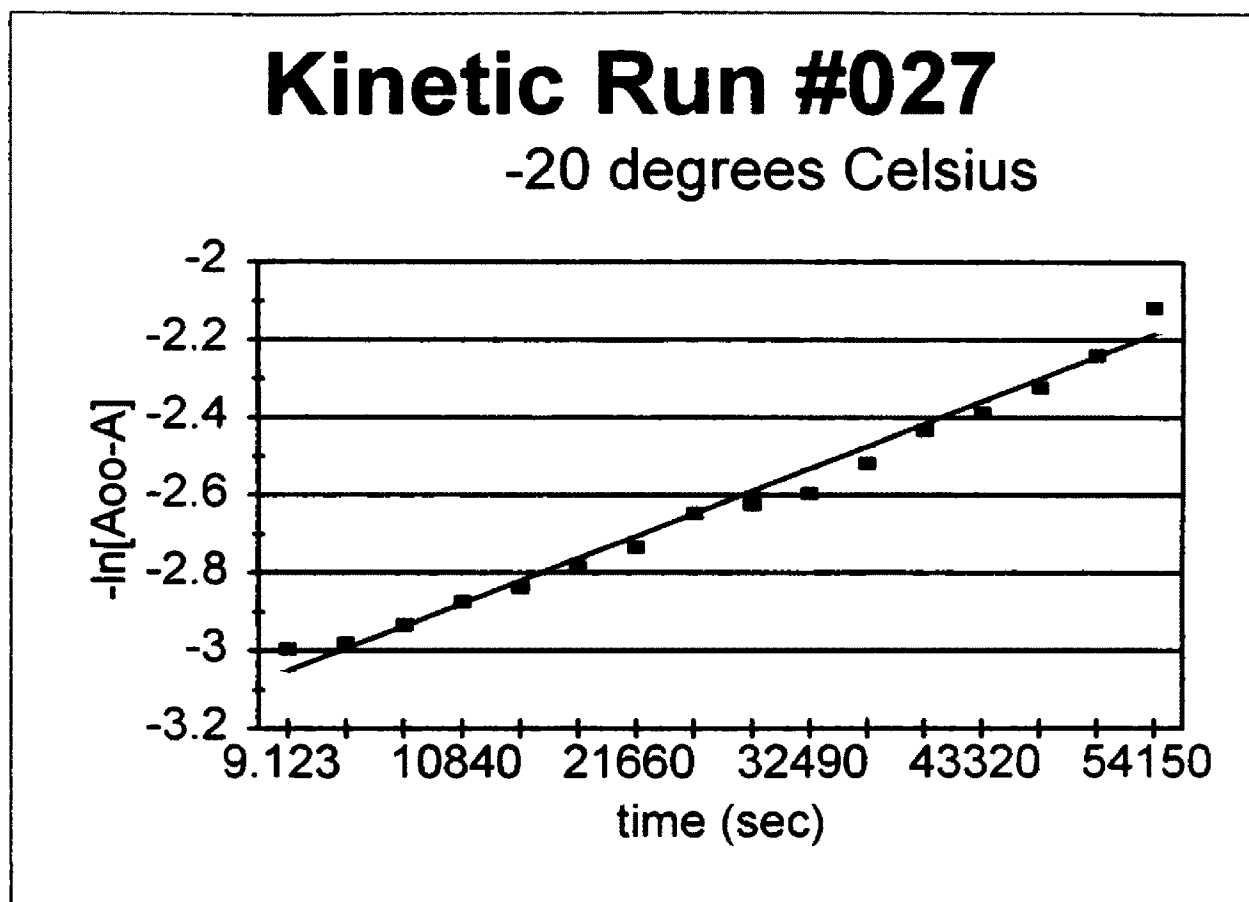


Figure 39: Kinetic plot of the formation of $\underline{5}$, $(\mu\text{-H})\text{Os}_3(\text{CO})_{10}$
 $(\mu\text{-}\eta^2\text{-HNCCF}_3)$ at -20°C .

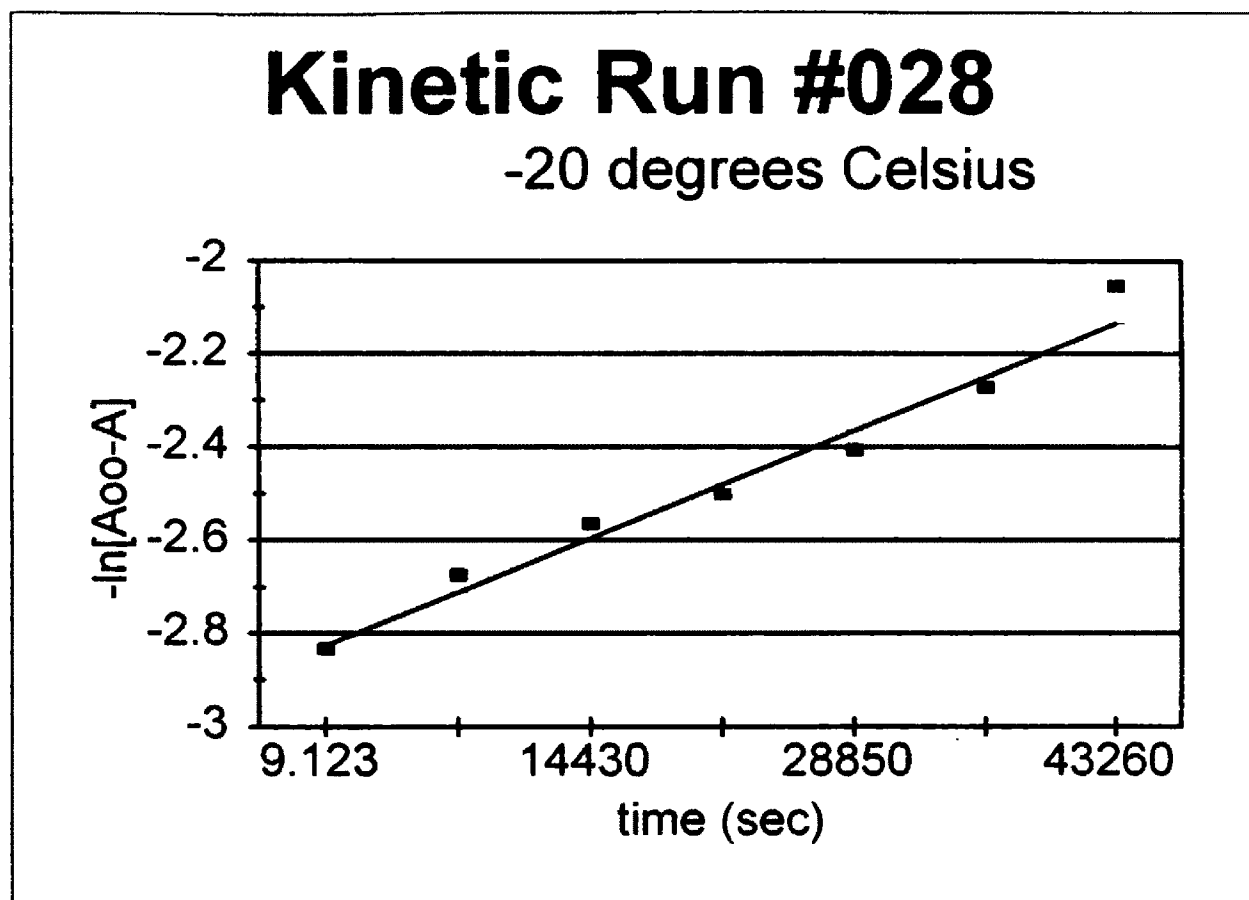


Figure 40: Kinetic plot of the formation of Σ , $(\mu\text{-H})\text{Os}_3(\text{CO})_{10}$
 $(\mu\text{-}\eta^2\text{-HNCCF}_3)$ at -20°C .

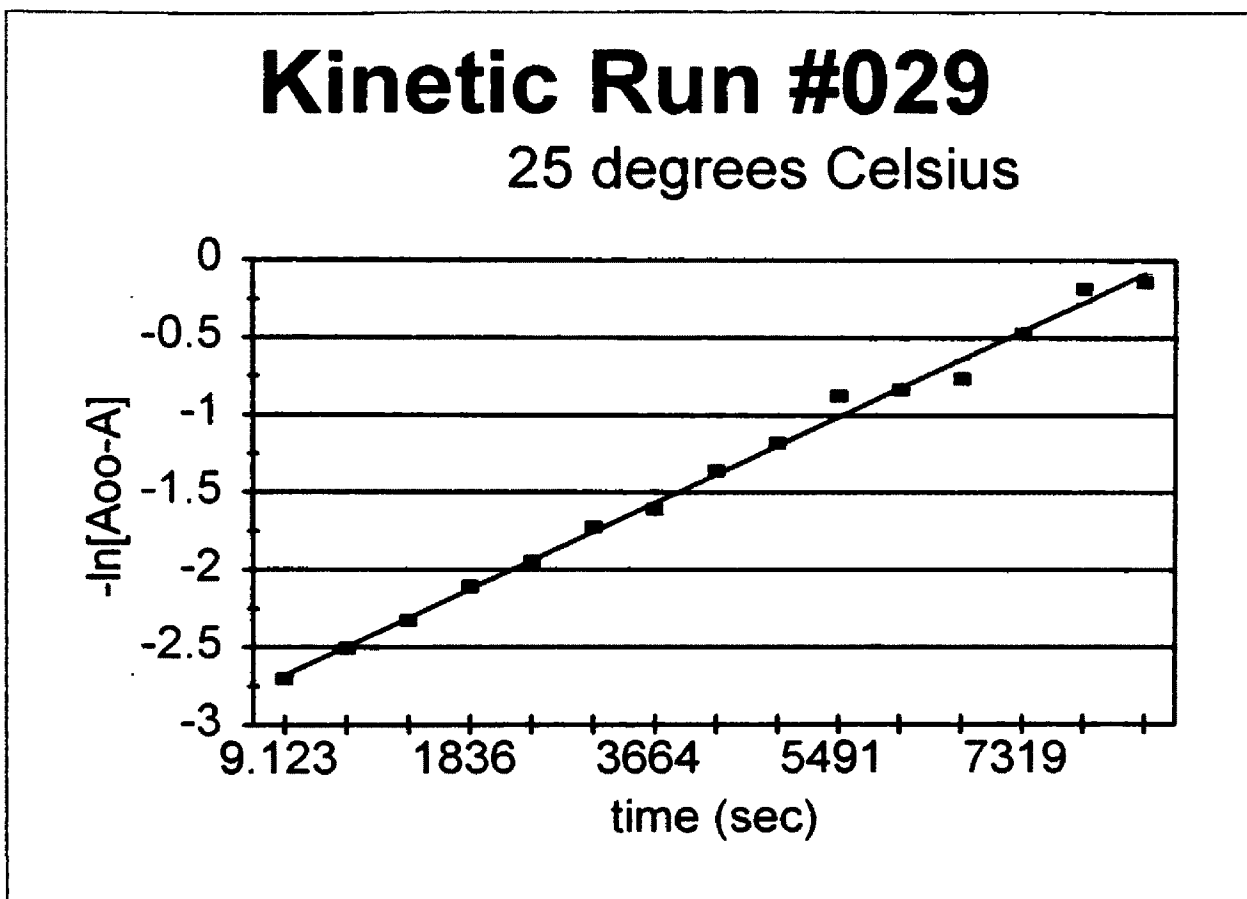


Figure 41: Deuterated kinetic plot of the formation of $\mathbf{4}$, $(\mu\text{-D})\text{Os}_3(\text{CO})_{10}$ ($\mu\text{-NC(D)CF}_3$) at 25°C.

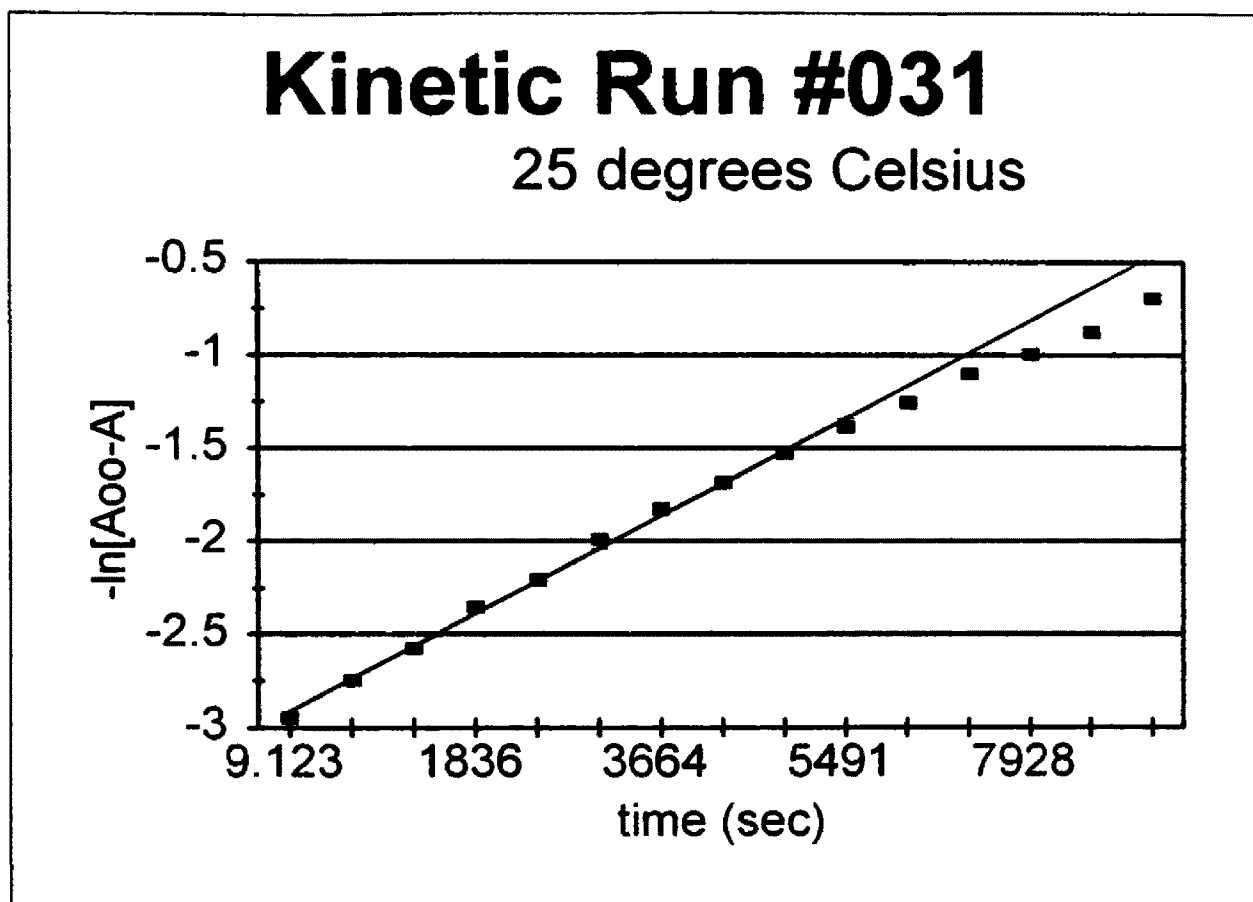


Figure 42: Deuterated kinetic plot of the formation of 4, (μ -D) $\text{Os}_3(\text{CO})_{10}$ (μ -NC(D)CF₃) at 25°C.

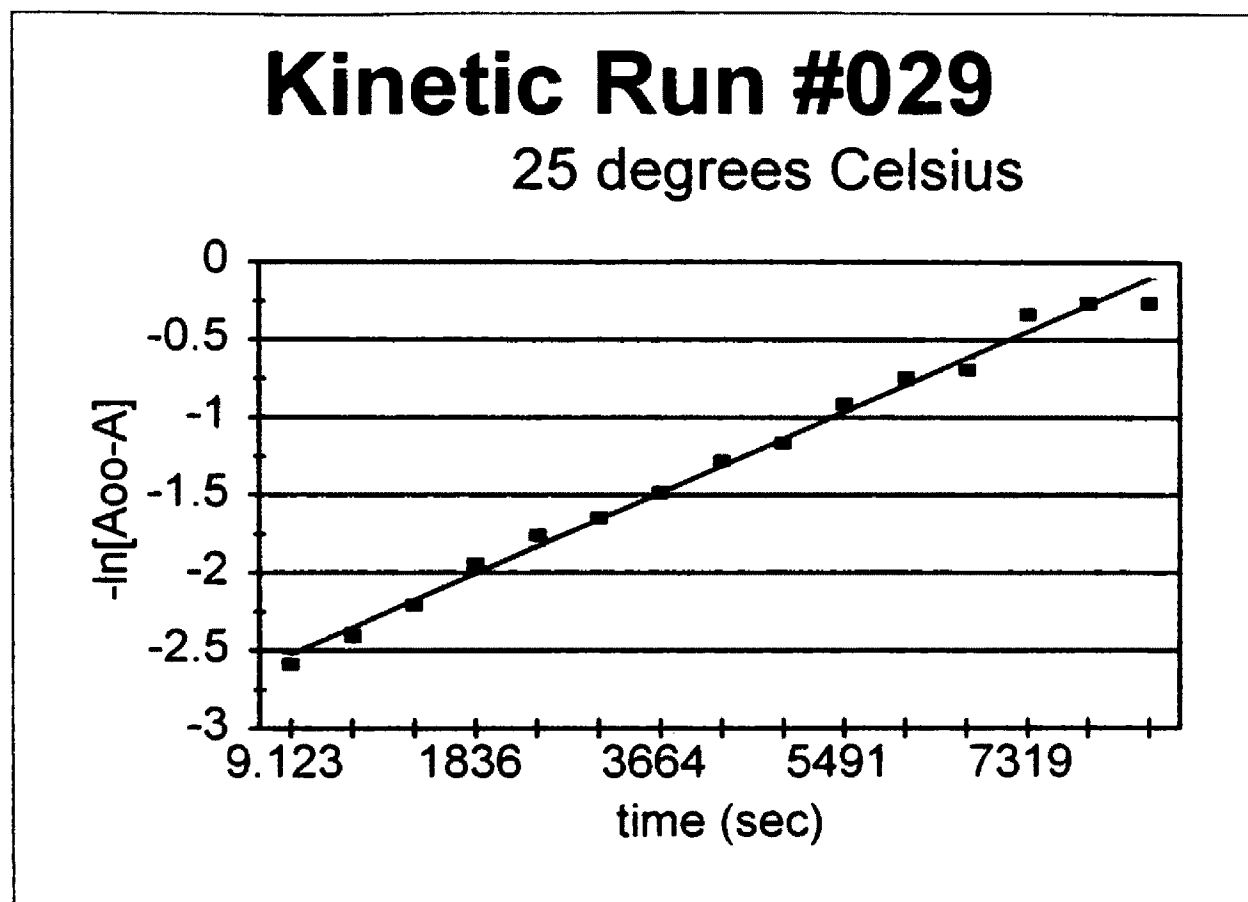


Figure 43: Deuterated kinetic plot of the formation of $\mathbf{5}$, $(\mu\text{-D})\text{Os}_3(\text{CO})_{10}$ ($\mu\text{-}\eta^2\text{-DNCCF}_3$) at 25°C.

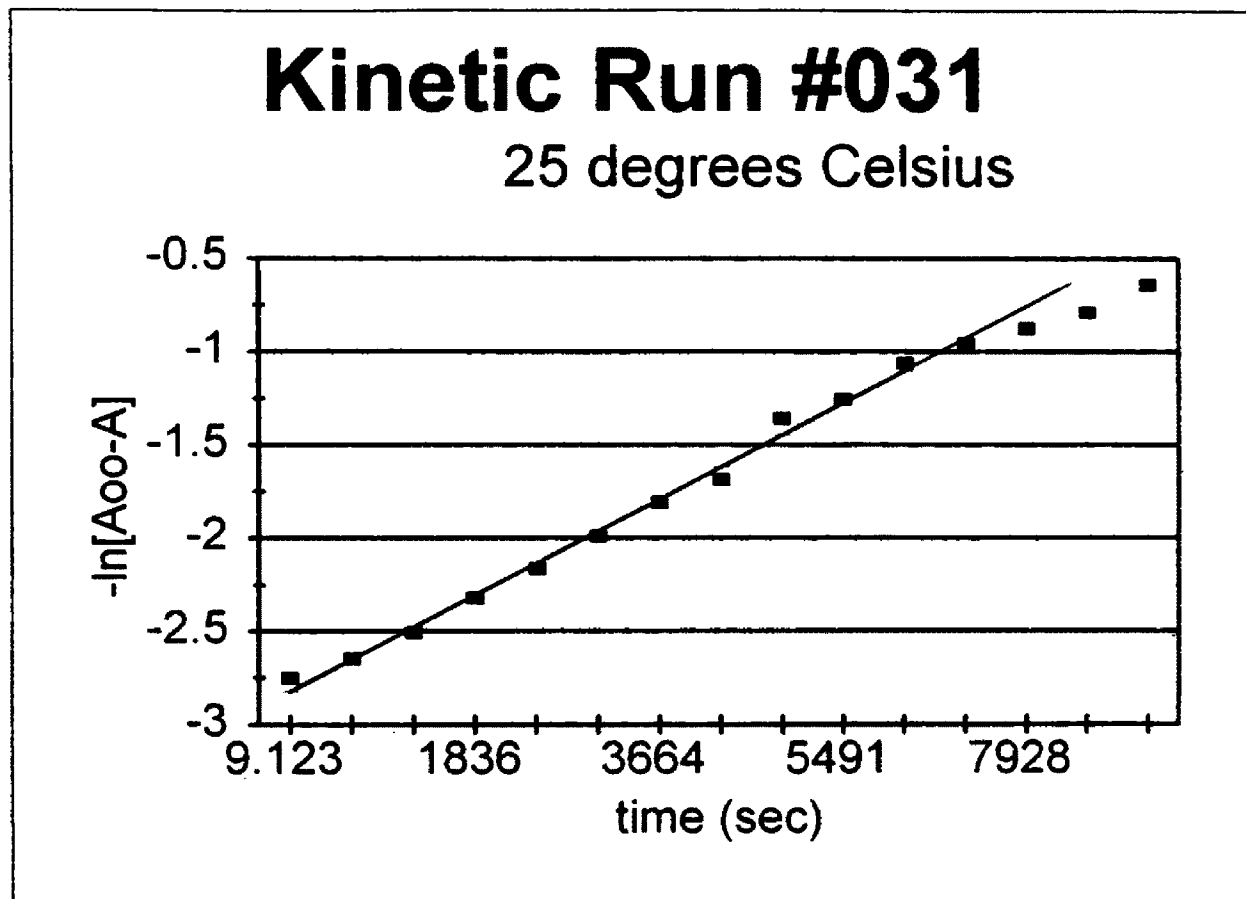


Figure 44: Deuterated kinetic plot of the formation of $\mathbf{5}$, $(\mu\text{-D})\text{Os}_3(\text{CO})_{10}$ ($\mu\text{-}\eta^2\text{-DNCCF}_3$) at 25°C.

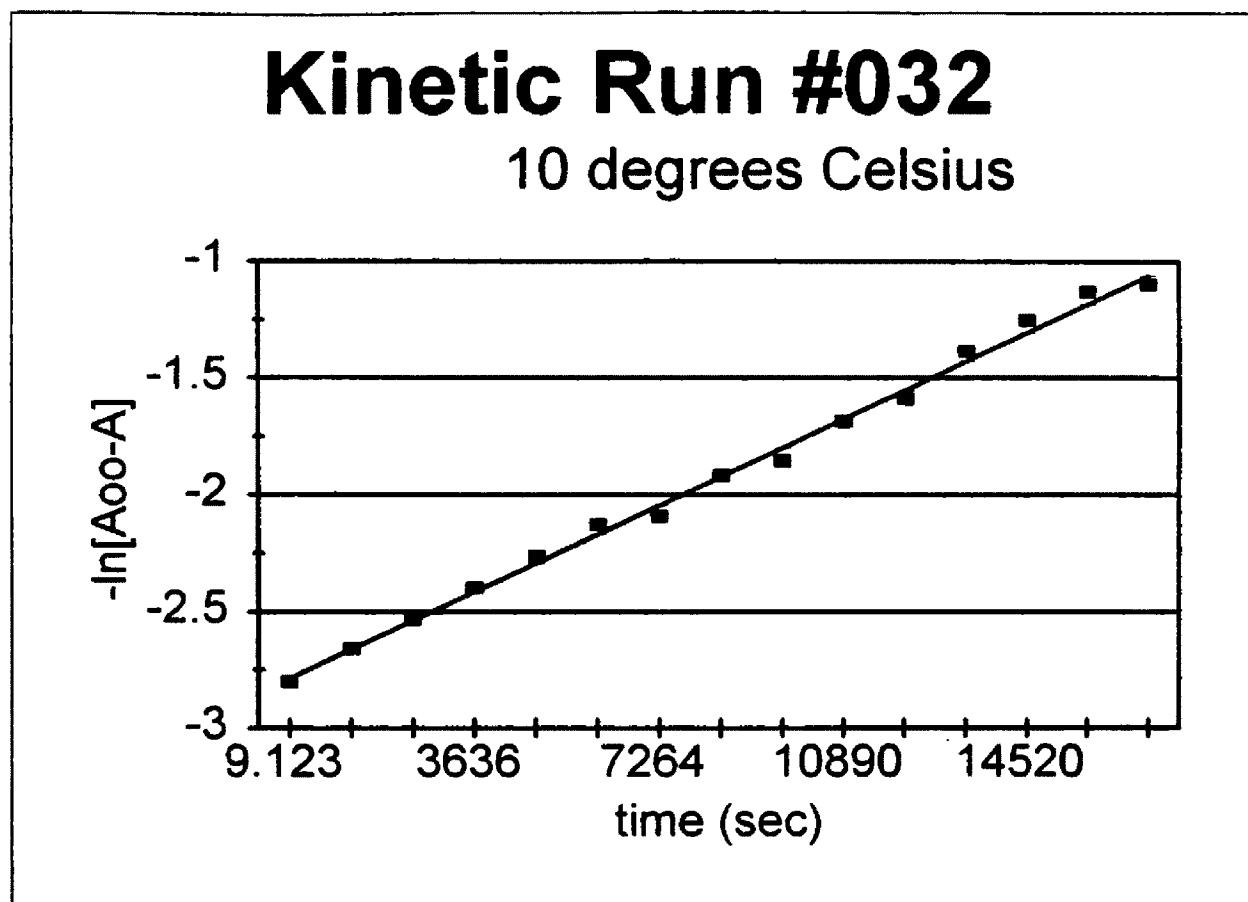


Figure 45: Deuterated kinetic plot of the formation of 4, (μ -D) $\text{Os}_3(\text{CO})_{10}$ (μ -NC(D)CF₃) at 10°C.

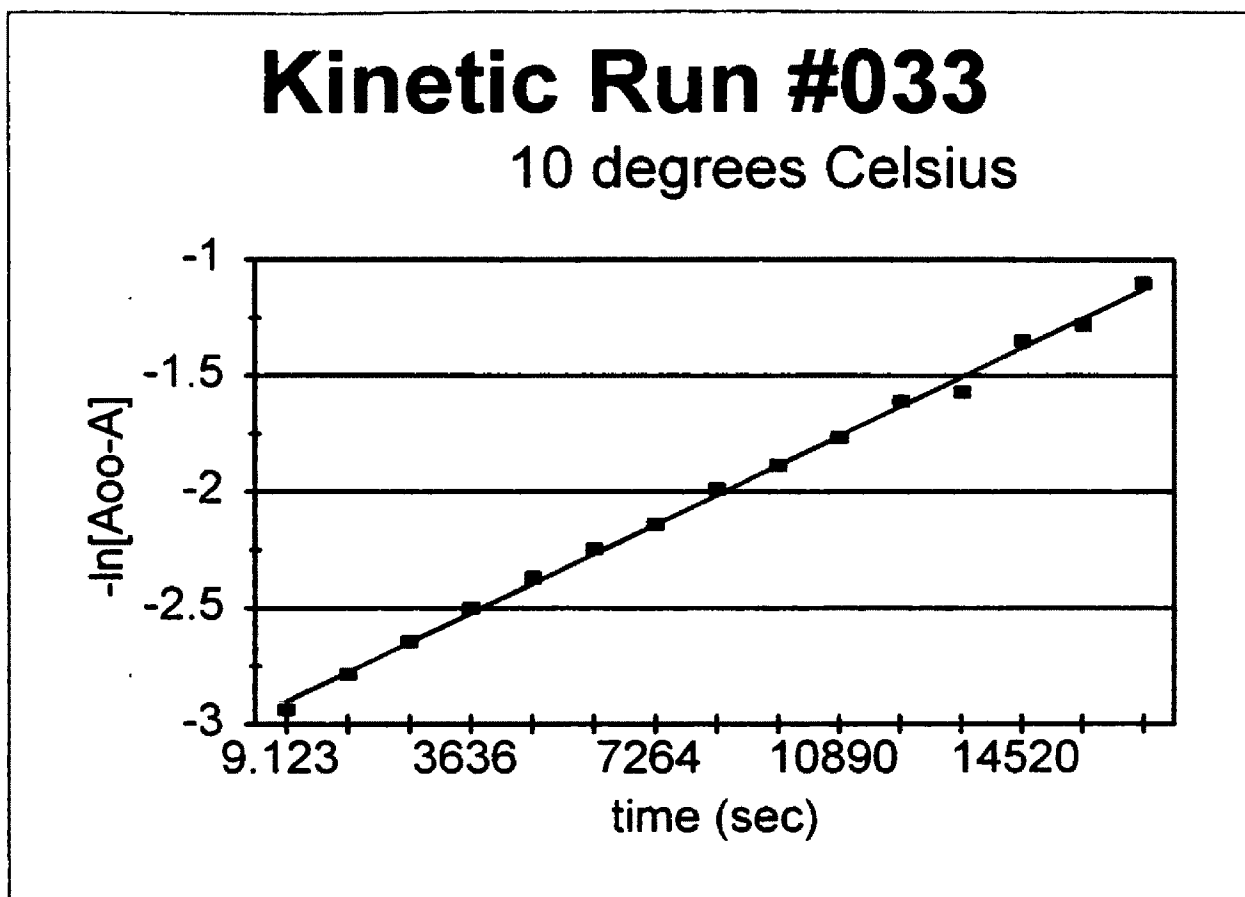


Figure 46: Deuterated kinetic plot of the formation of $\underline{4}$, $(\mu\text{-D})\text{Os}_3(\text{CO})_{10}$ ($\mu\text{-NC(D)CF}_3$) at 10°C.

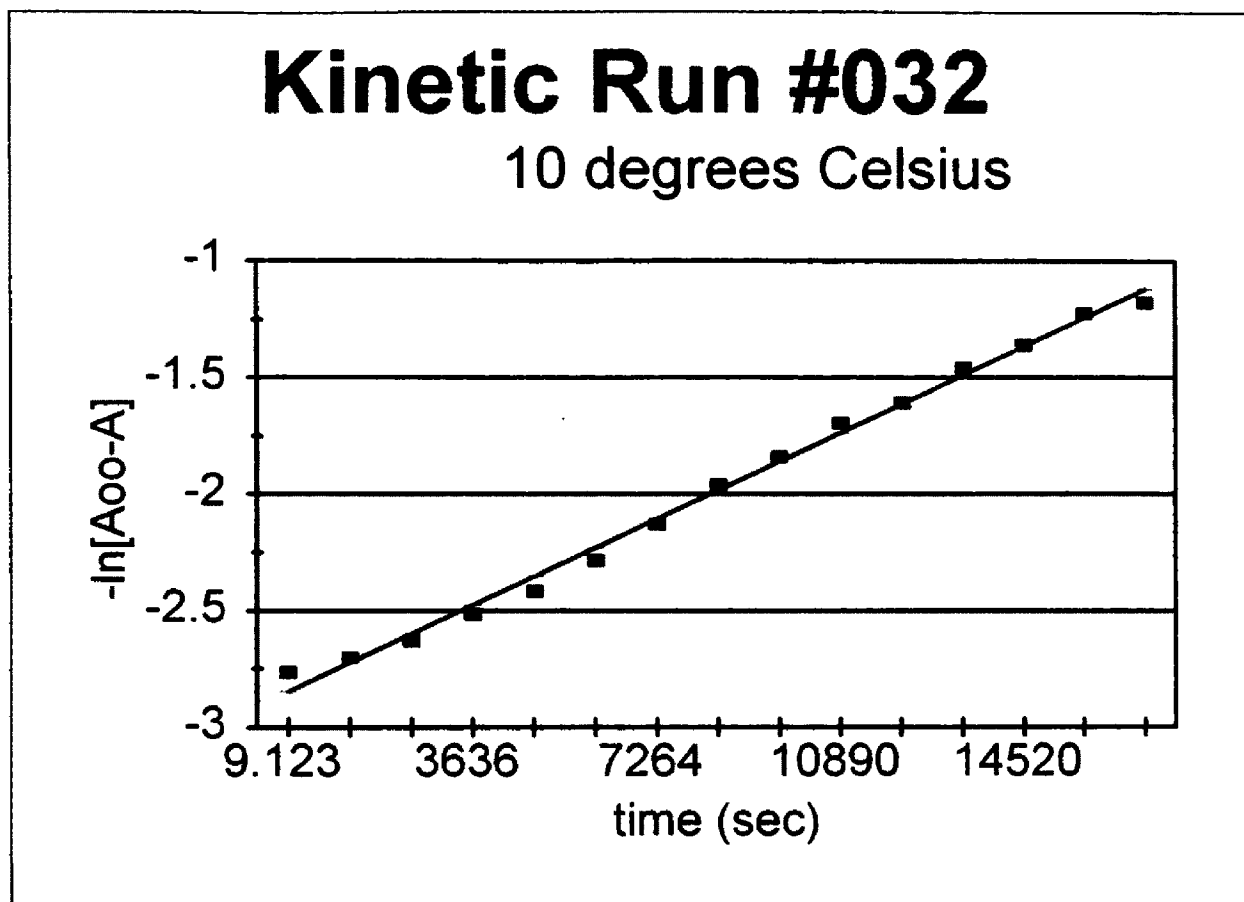


Figure 47: Deuterated kinetic plot of the formation of **5, $(\mu\text{-D})\text{Os}_3(\text{CO})_{10}$ ($\mu\text{-}\eta^2\text{-DNCCF}_3$) at 10°C.**

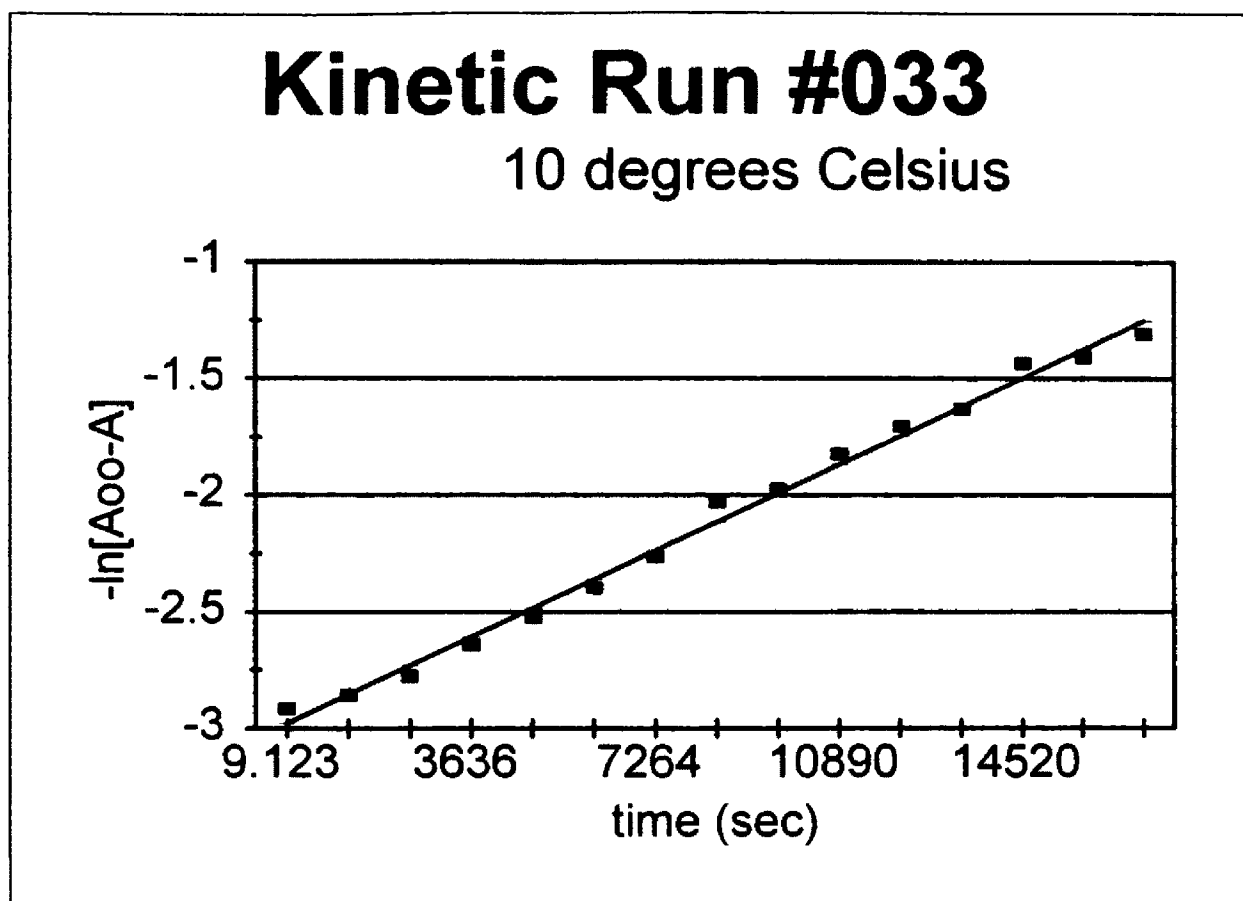


Figure 48: Deuterated kinetic plot of the formation of $\mathbf{5}$, $(\mu\text{-D})\text{Os}_3(\text{CO})_{10}$ ($\mu\text{-}\eta^2\text{-DNCCF}_3$) at 10°C .

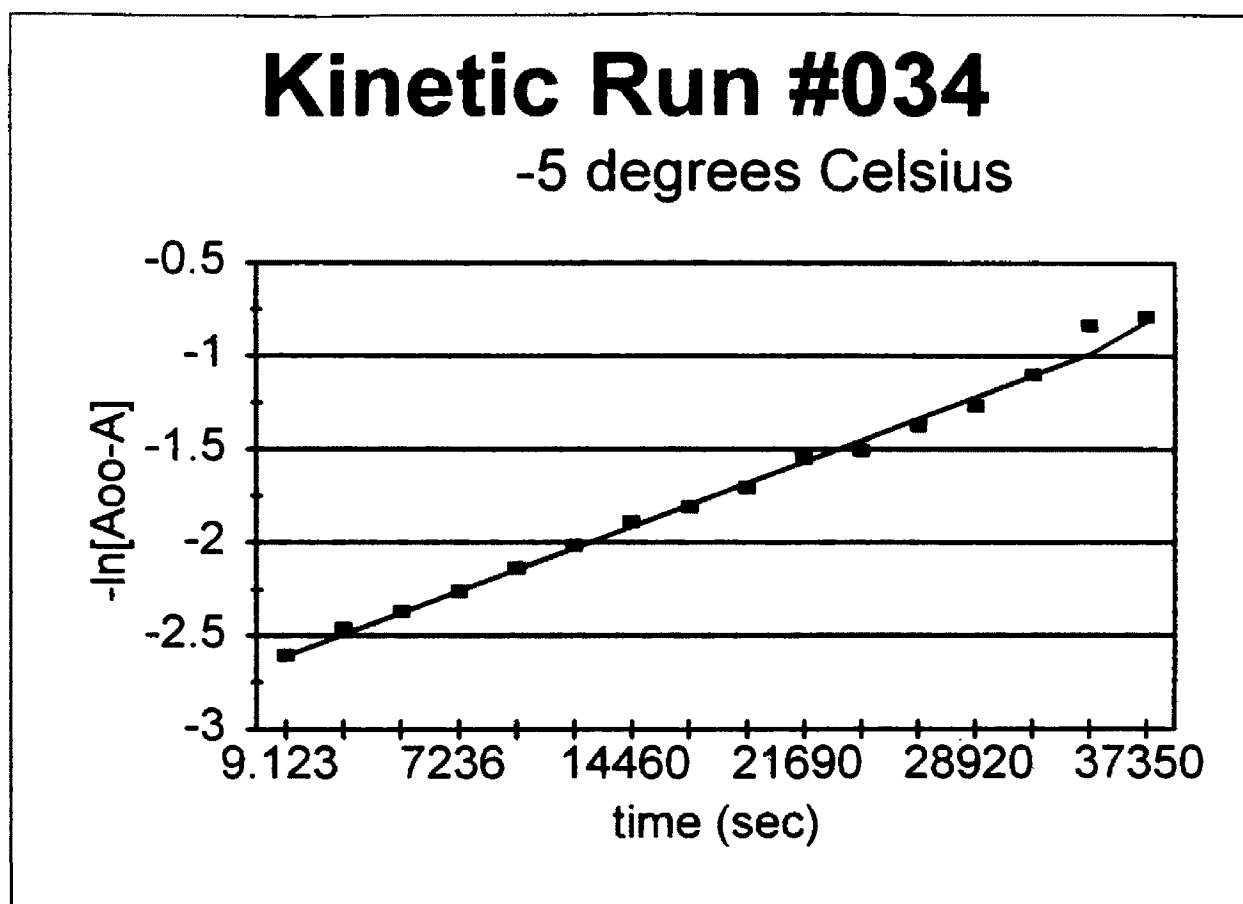


Figure 49: Deuterated kinetic plot of the formation of 4, (μ -D) $\text{Os}_3(\text{CO})_{10}$ (μ -NC(D)CF₃) at -5°C.

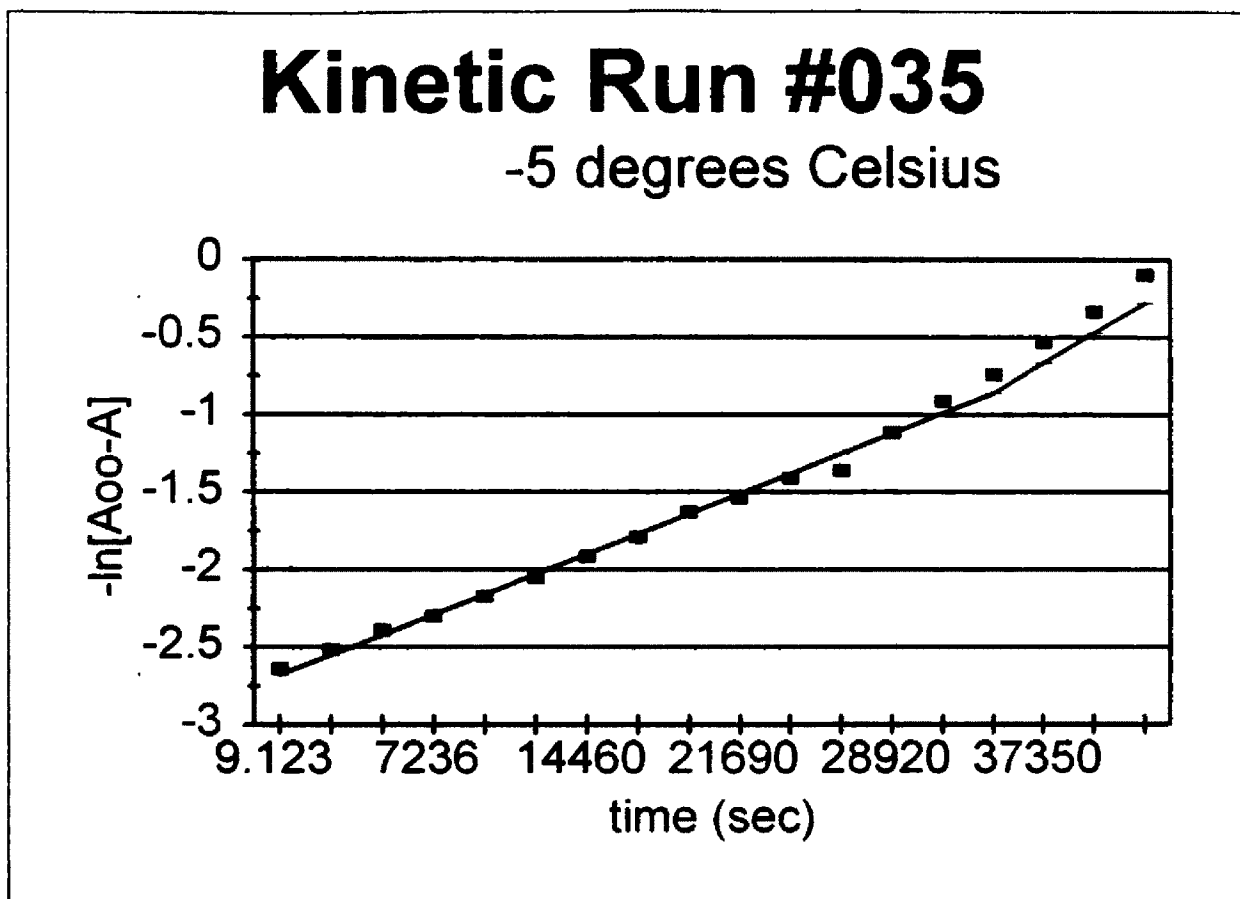


Figure 50: Deuterated kinetic plot of the formation of 4, $(\mu\text{-D})\text{Os}_3(\text{CO})_{10}$ ($\mu\text{-NC(D)CF}_3$) at -5°C .

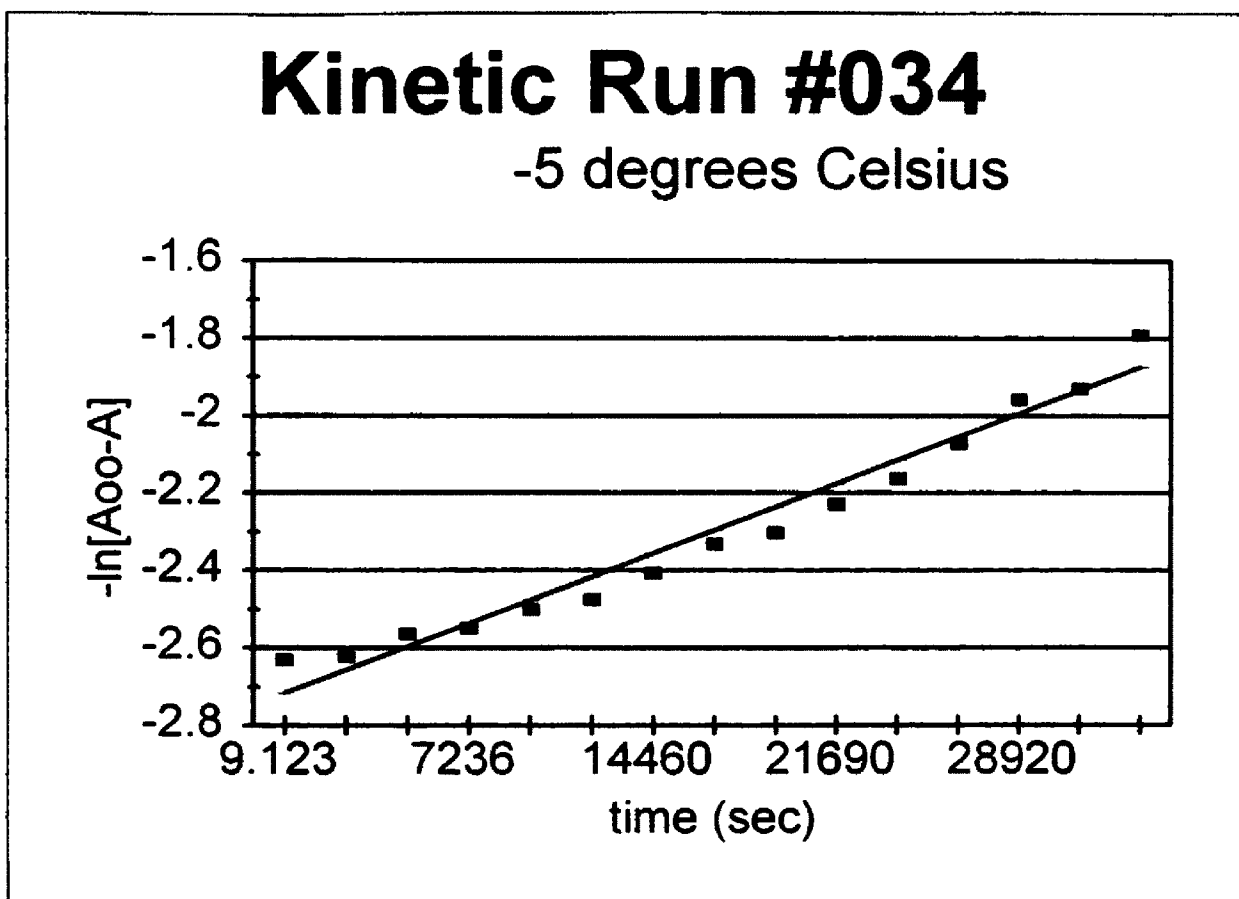


Figure 51: Deuterated kinetic plot of the formation of $\mathbf{5}$, $(\mu\text{-D})\text{Os}_3(\text{CO})_{10}$ ($\mu\text{-}\eta^2\text{-DNCCF}_3$) at -5°C .

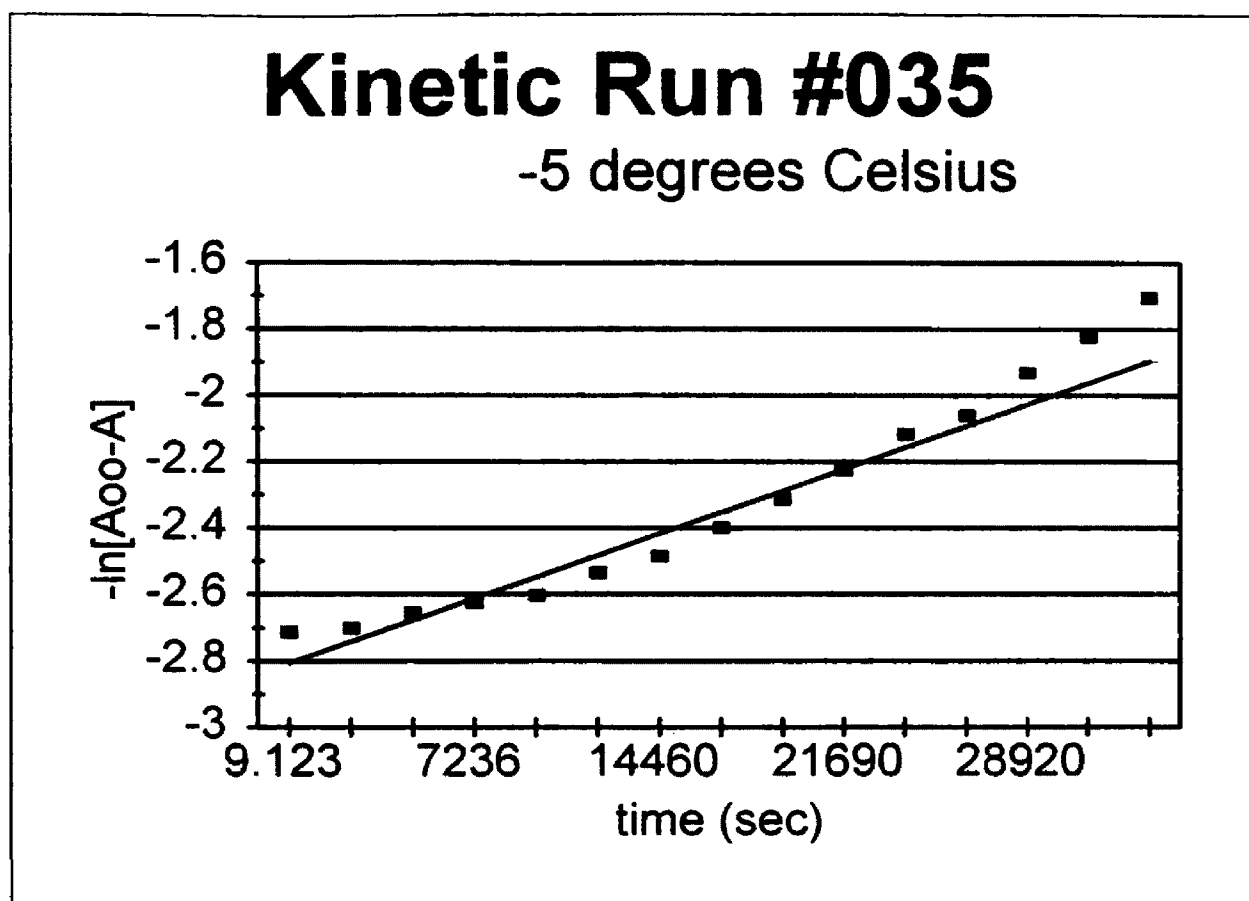


Figure 52: Deuterated kinetic plot of the formation of Σ , (μ -D)Os₃(CO)₁₀ (μ - η^2 -DNCCF₃) at -5°C.

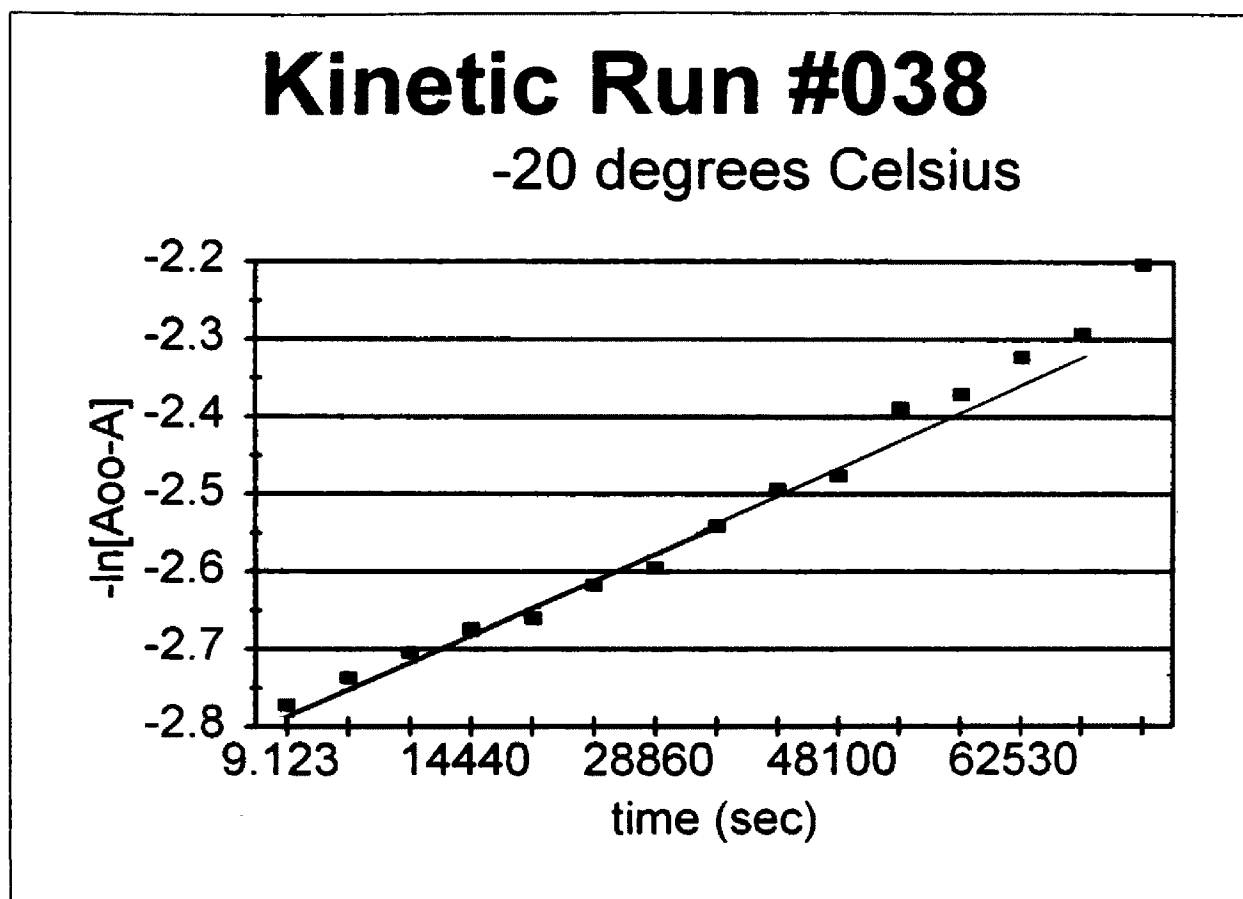


Figure 53: Deuterated kinetic plot of the formation of 4, (μ -D) $\text{Os}_3(\text{CO})_{10}$ (μ -NC(D)CF₃) at -20°C.

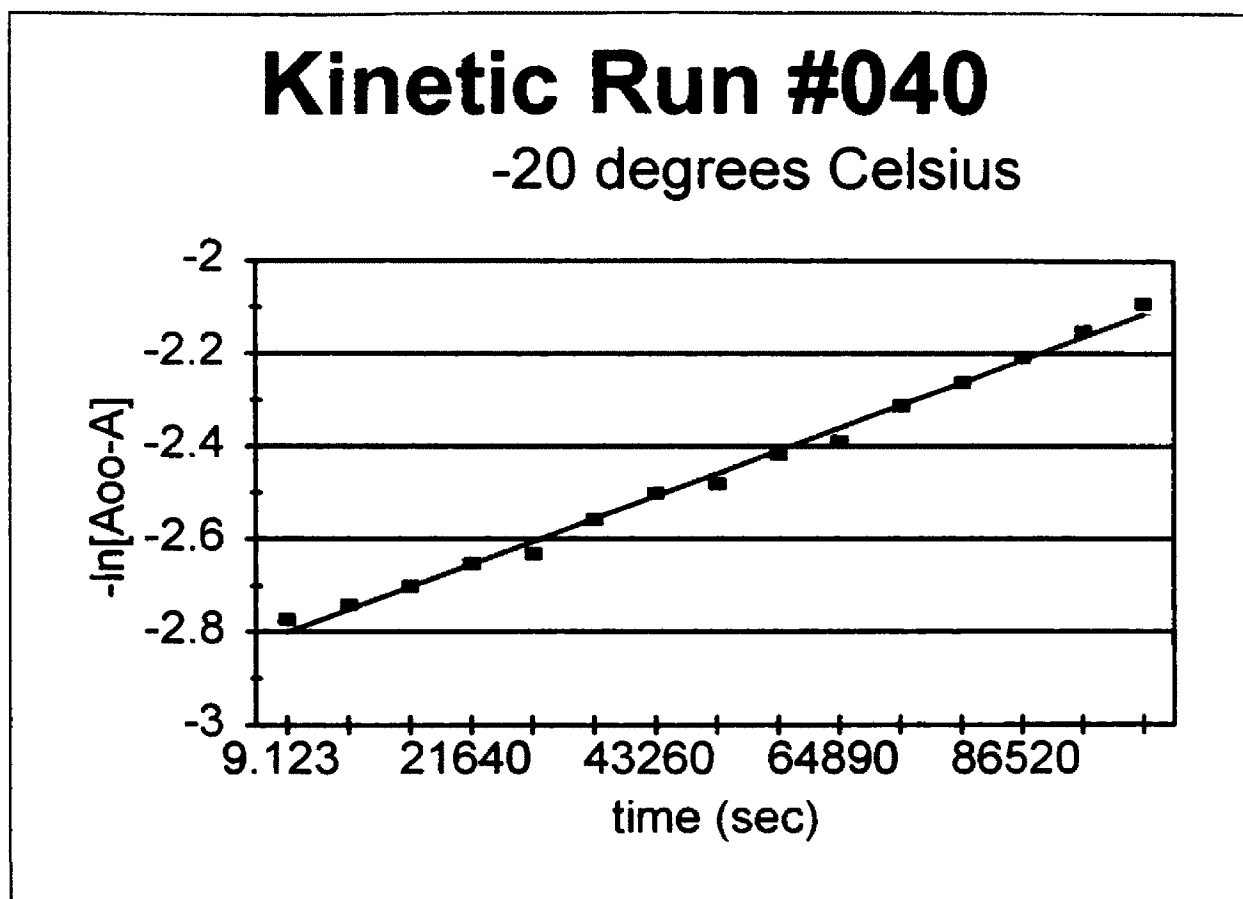


Figure 54: Deuterated kinetic plot of the formation of $\mathbf{4}$, $(\mu\text{-D})\text{Os}_3(\text{CO})_{10}$ ($\mu\text{-NC(D)CF}_3$) at $-20\text{ }^\circ\text{C}$.

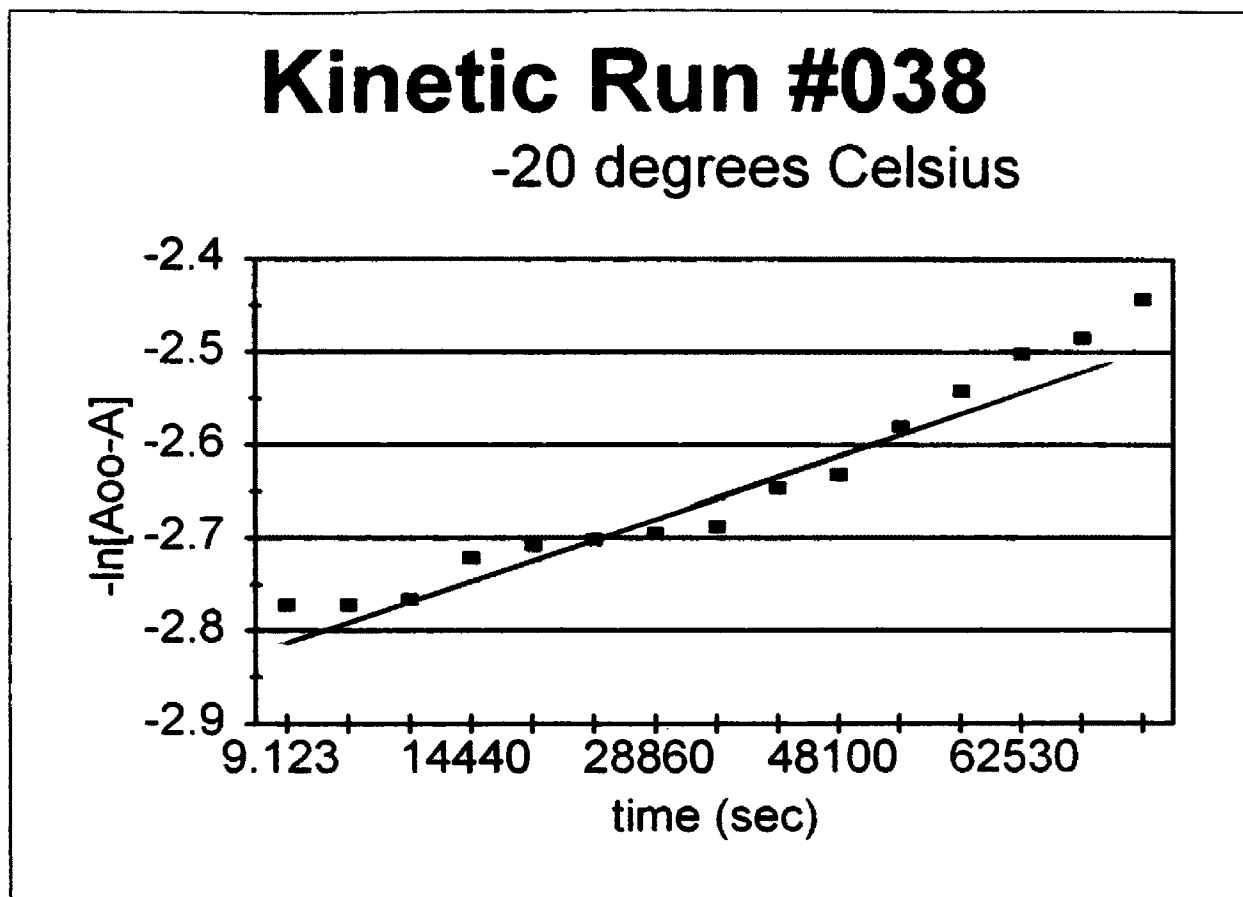


Figure 55: Deuterated kinetic plot of the formation of $\mathbf{5}$, $(\mu\text{-D})\text{Os}_3(\text{CO})_{10}$ ($\mu\text{-}\eta^2\text{-DNCCF}_3$) at -20°C .

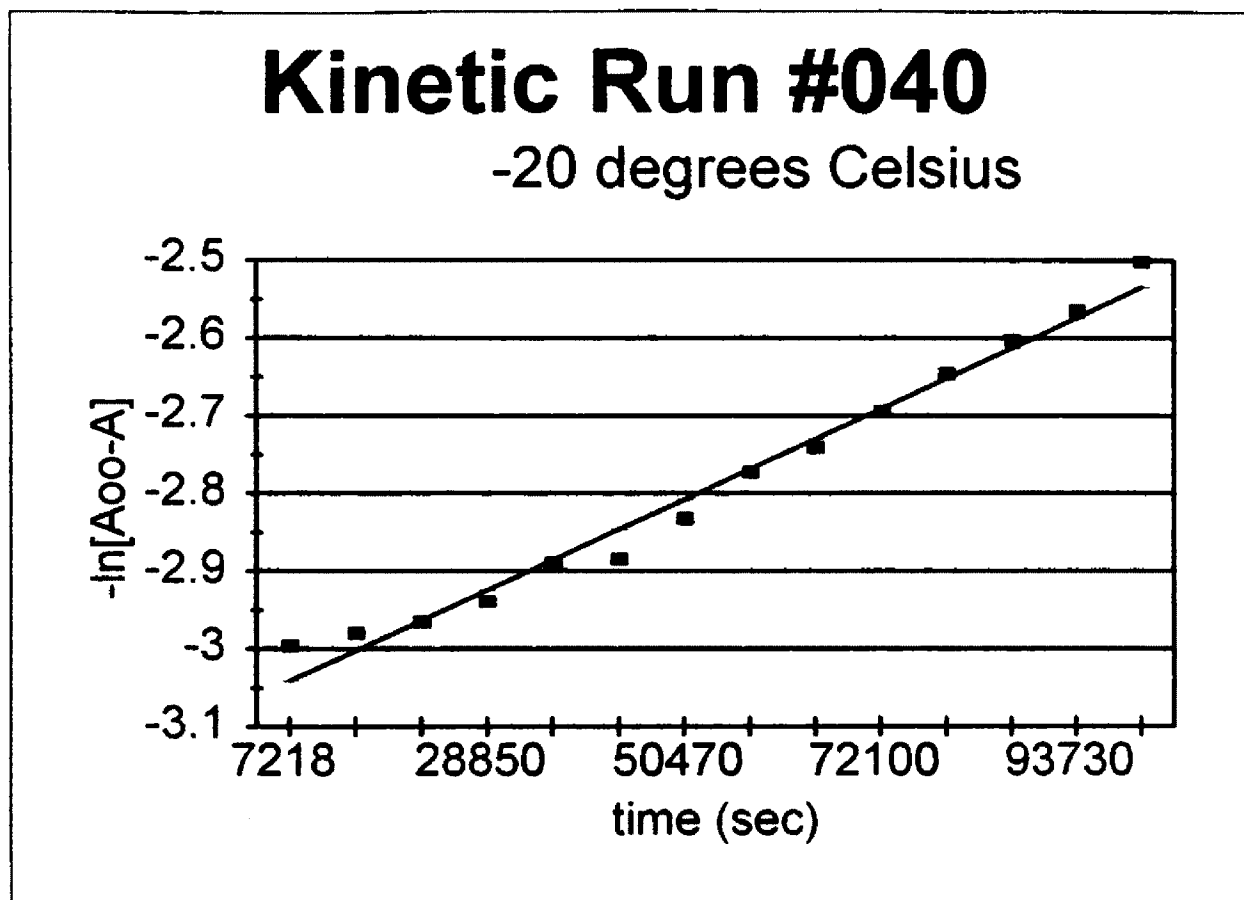


Figure 56: Deuterated kinetic plot of the formation of $\mathbf{5}$, $(\mu\text{-D})\text{Os}_3(\text{CO})_{10}$ ($\mu\text{-}\eta^2\text{-DNCCF}_3$) at -20°C .

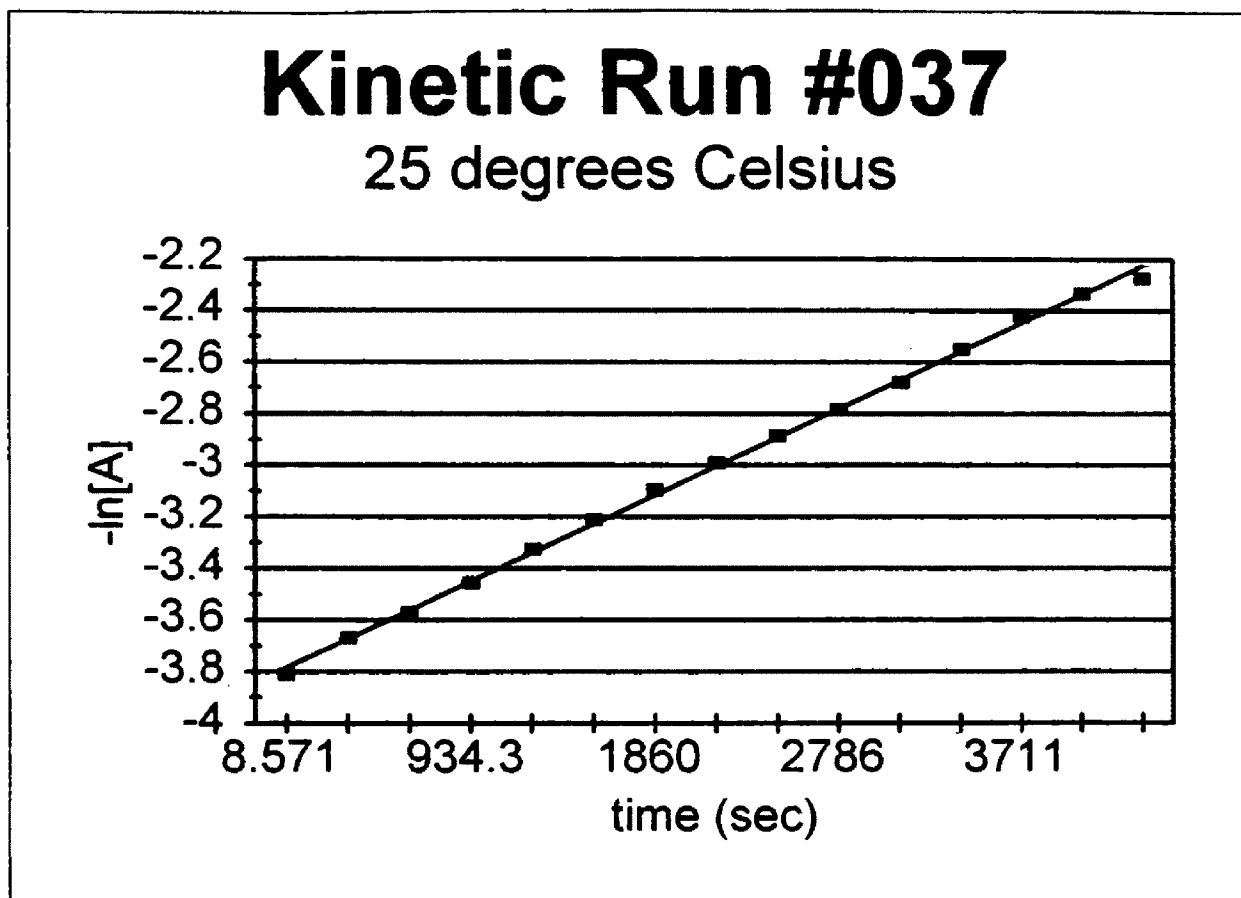


Figure 57: ^1H kinetic plot of the disappearance of the starting material, $\text{H}_2\text{Os}_3(\text{CO})_{10}$ at 25 °C.

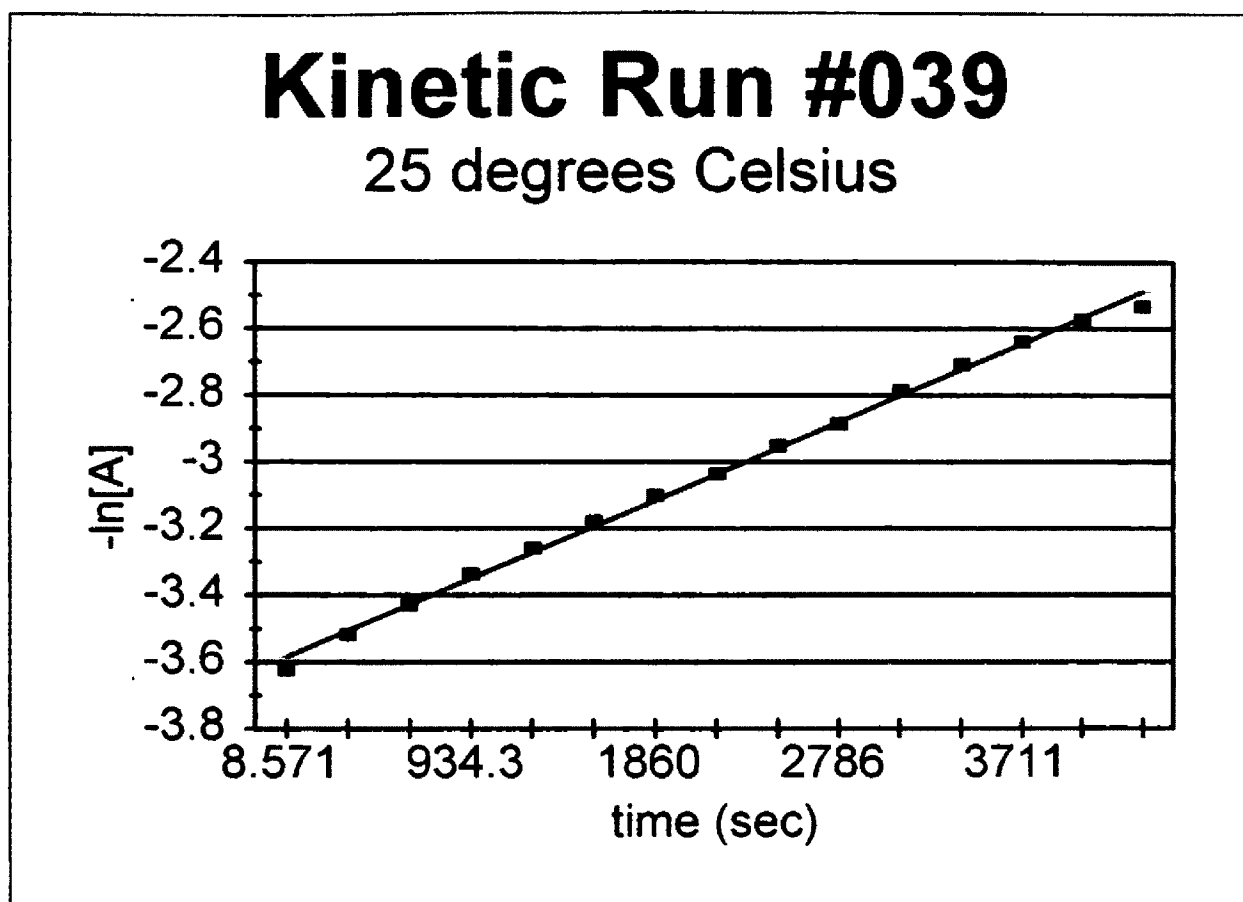


Figure 58: ^1H kinetic plot of the disappearance of the starting material, $\text{H}_2\text{Os}_3(\text{CO})_{10}$ at 25 °C.

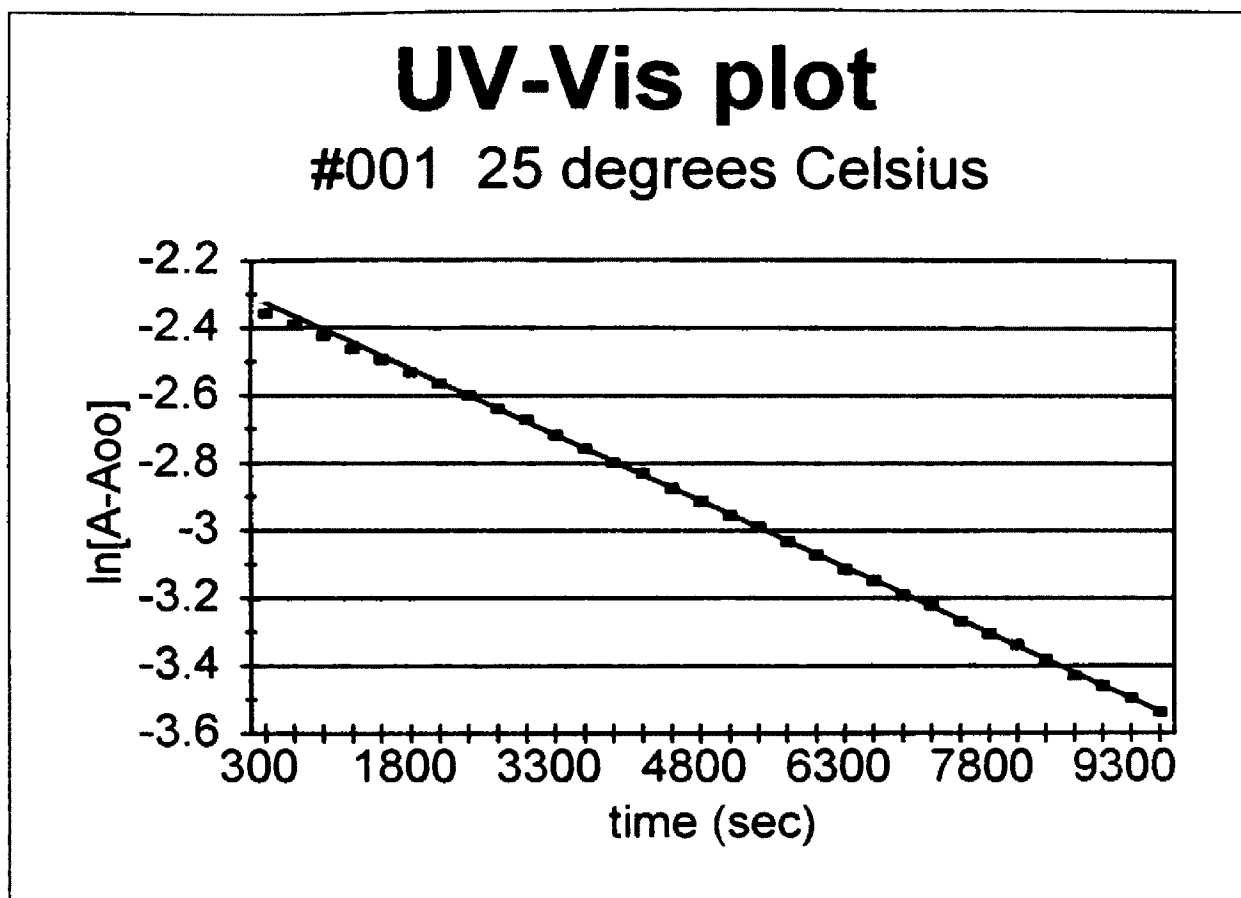


Figure 59: UV-Vis kinetic plot of the disappearance of the starting material, $\text{H}_2\text{Os}_3(\text{CO})_{10}$, at 25 °C, and 552 nm., with 4 ml of gas (CF_3CN).

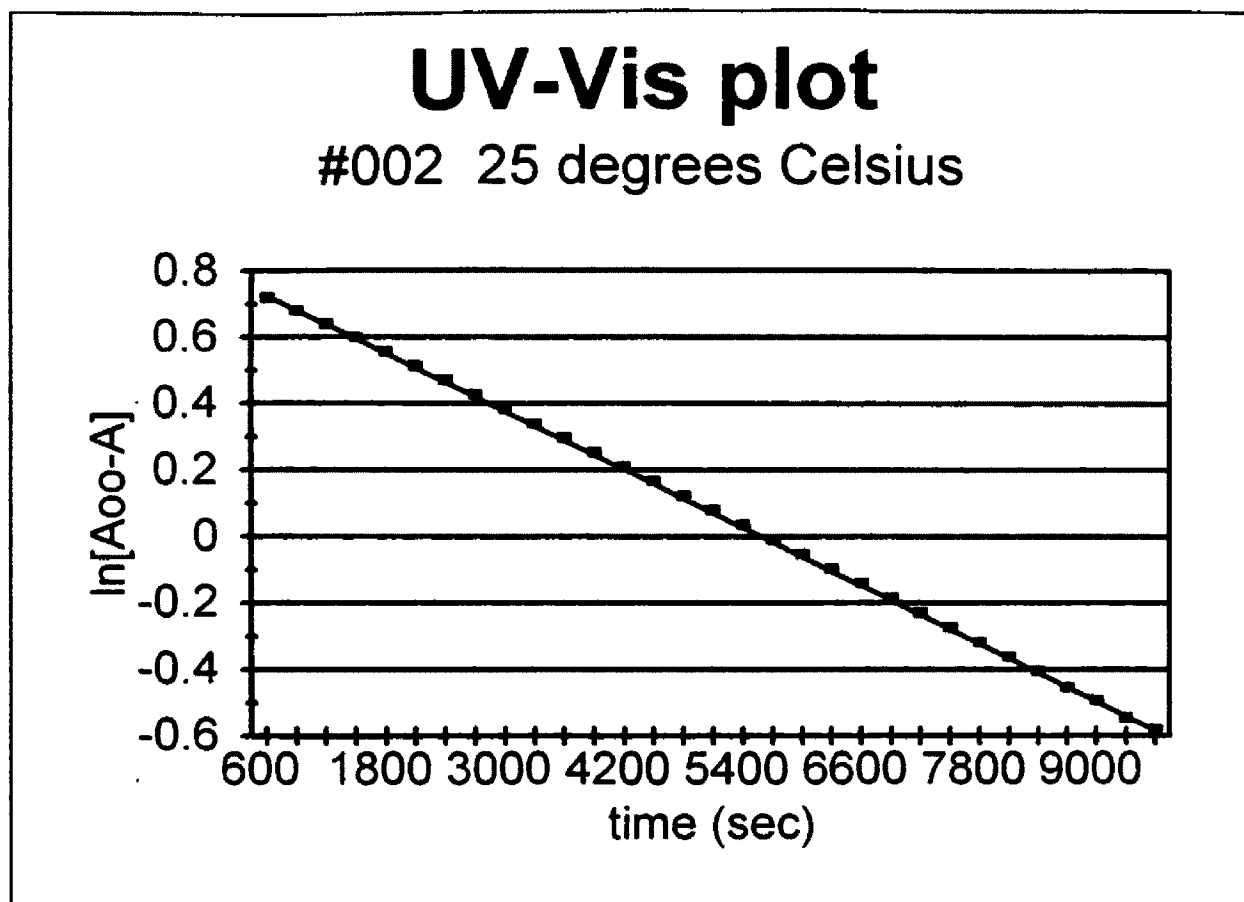


Figure 60: UV-Vis kinetic plot of the formation of 4, ($\mu\text{-H}$)Os₃(CO)₁₀ ($\mu\text{-NC(H)CF}_3$) and 5, ($\mu\text{-H}$)Os₃(CO)₁₀($\mu\text{-}\eta^2\text{-HNCCF}_3$) at 25 °C, and 390 nm., with 4 ml of gas (CF₃CN).

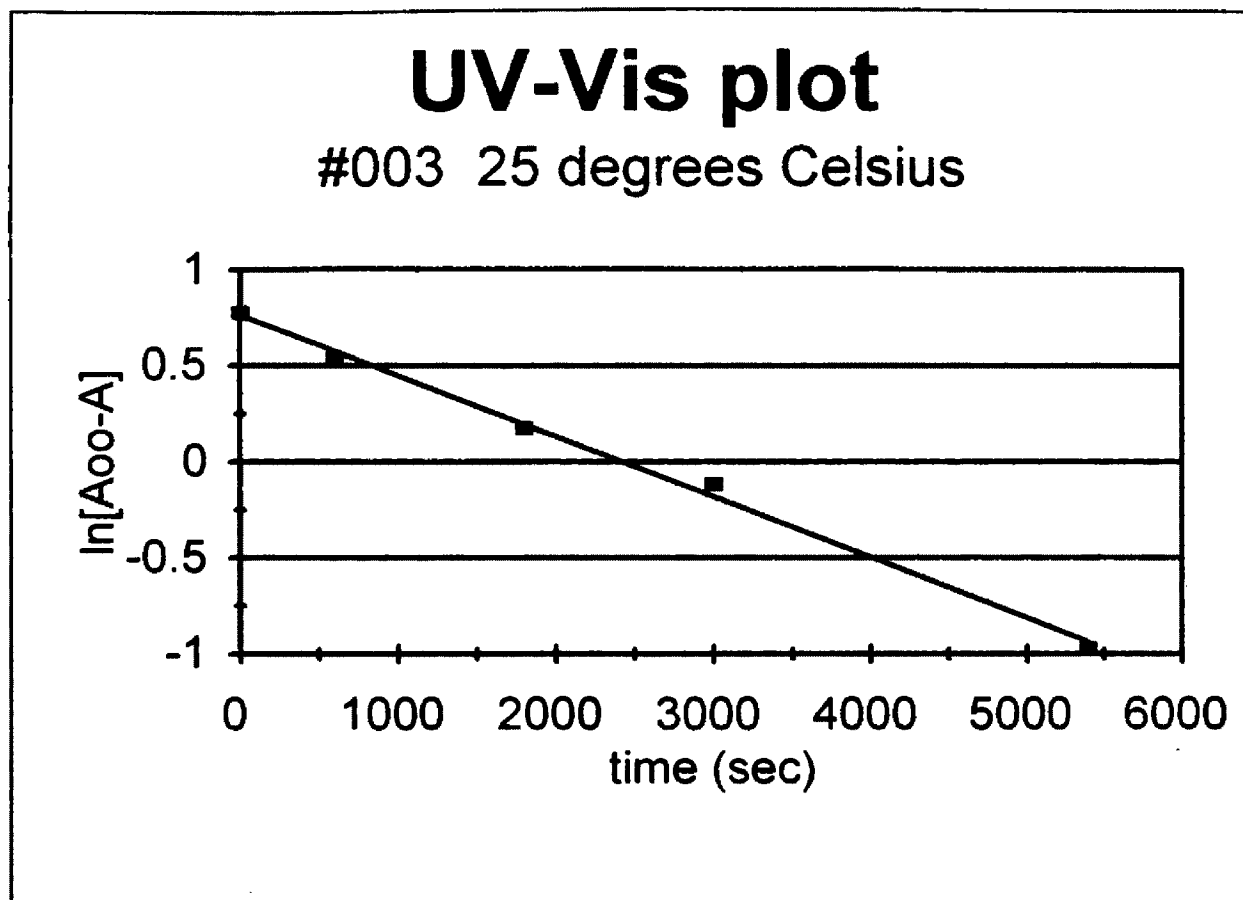


Figure 61: UV-Vis kinetic plot of the formation of 4, ($\mu\text{-H}$)Os₃(CO)₁₀ ($\mu\text{-NC(H)CF}_3$) and 5, ($\mu\text{-H}$)Os₃(CO)₁₀($\mu\text{-}\eta^2\text{-HNCCF}_3$) at 25 °C, and 392 nm., with 10 ml of gas (CF₃CN).

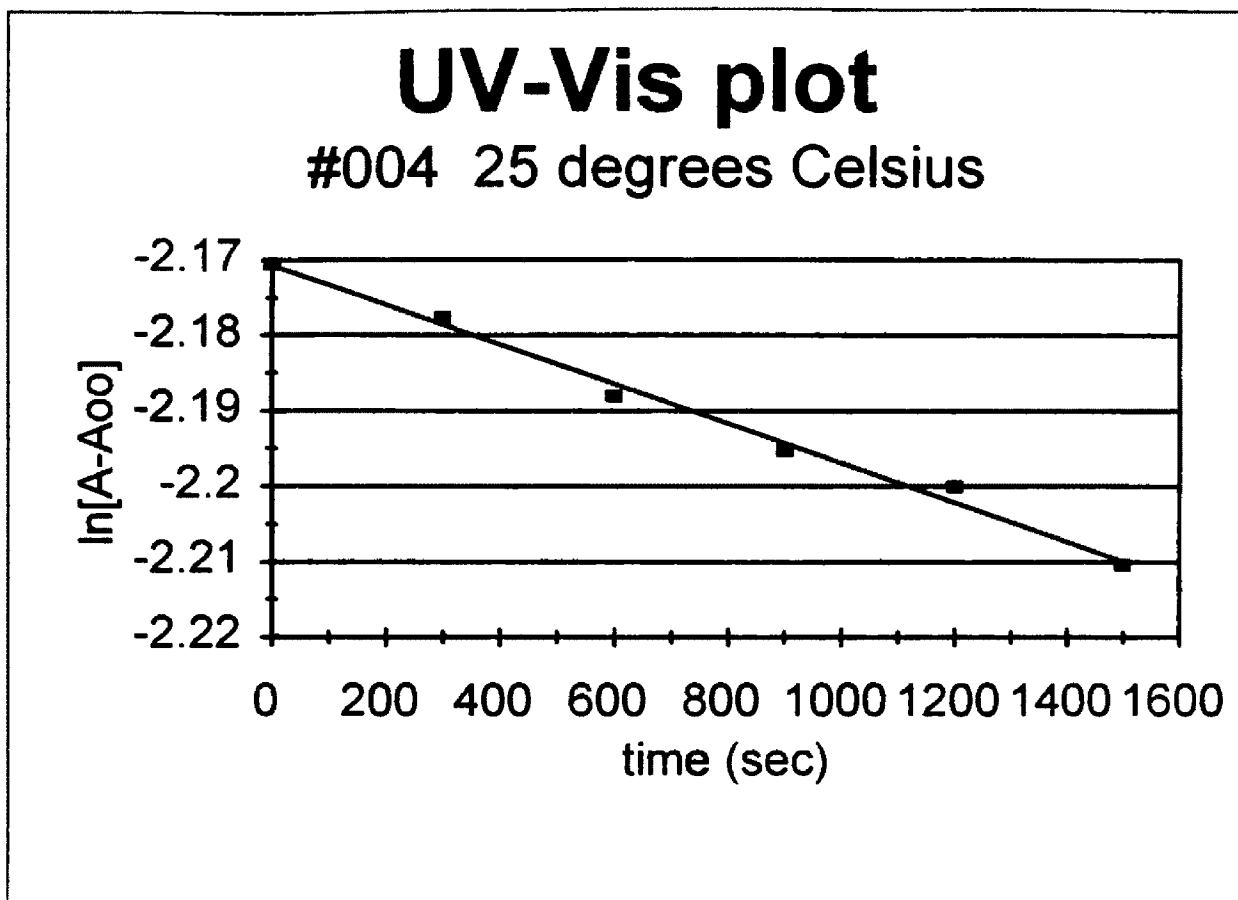


Figure 62: UV-Vis kinetic plot of the formation of 4, ($\mu\text{-H}$)Os₃(CO)₁₀ ($\mu\text{-NC(H)CF}_3$) and 5, ($\mu\text{-H}$)Os₃(CO)₁₀($\mu\text{-}\eta^2\text{-HNCCF}_3$) at 25 °C, and 392 nm., with 1ml of gas (CF₃CN).

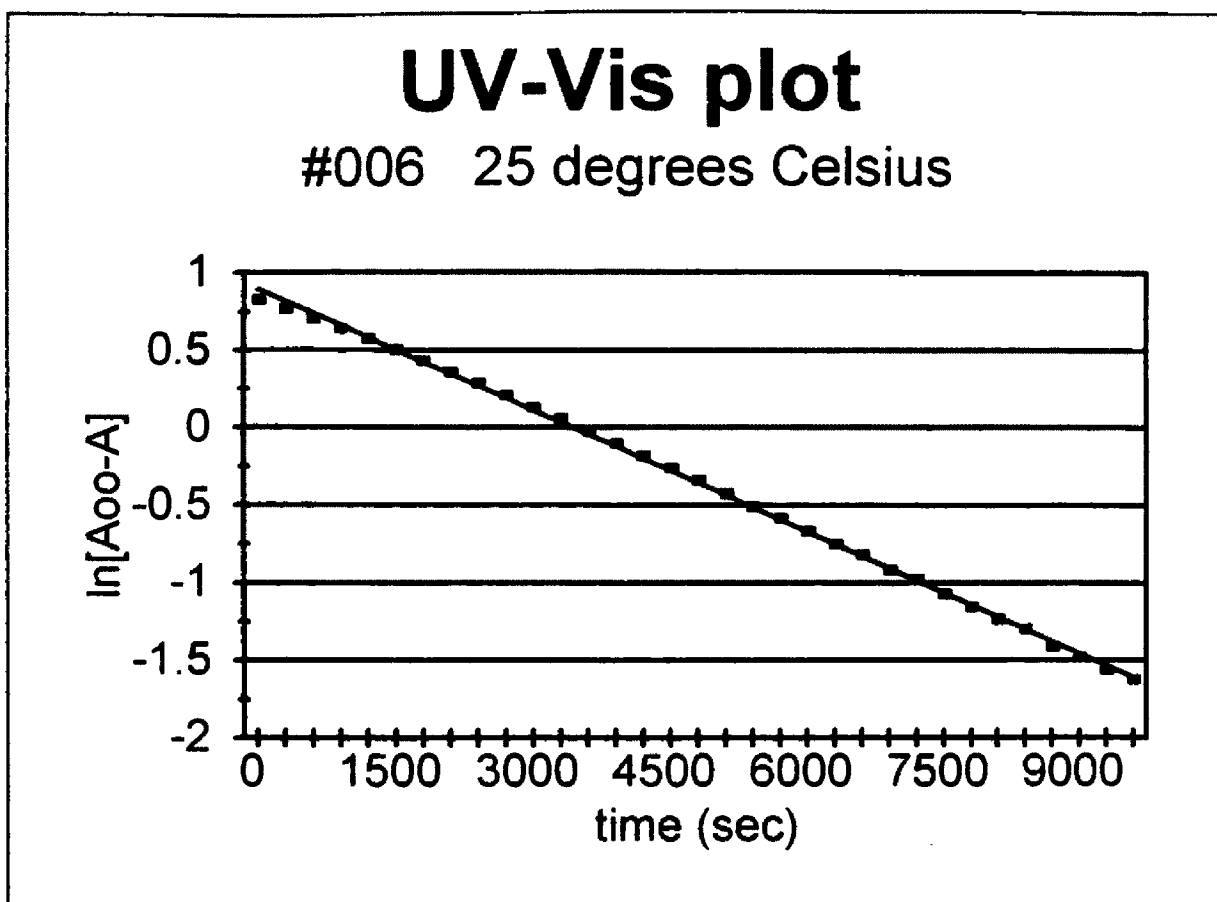


Figure 63: UV-Vis kinetic plot of the formation of **4**, $(\mu\text{-H})\text{Os}_3(\text{CO})_{10}$ ($\mu\text{-NC(H)CF}_3$) and **5**, $(\mu\text{-H})\text{Os}_3(\text{CO})_{10}(\mu\text{-}\eta^2\text{-HNCCF}_3)$ at 25 °C, and 392 nm., with 8 ml of gas (CF_3CN).

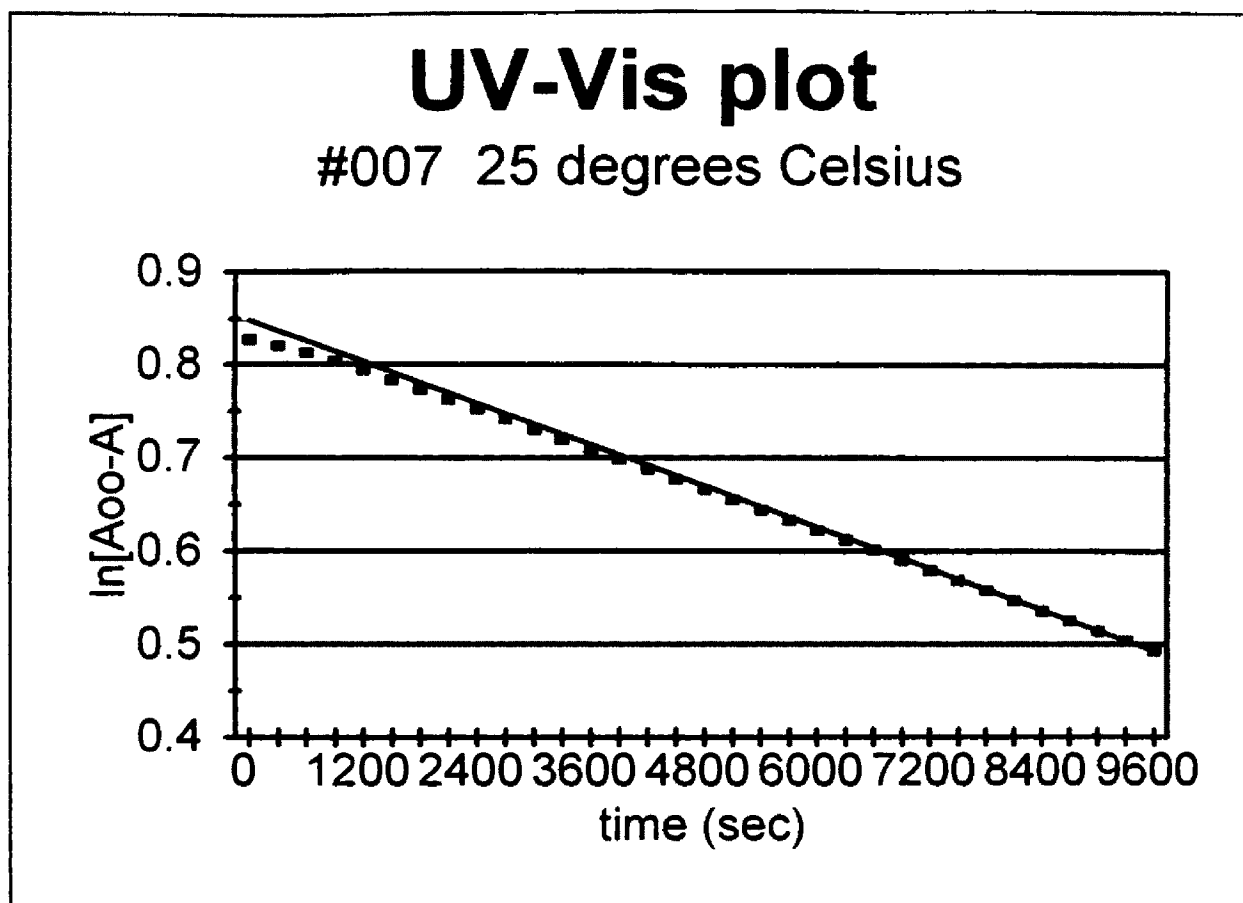


Figure 64: UV-Vis kinetic plot of the formation of **4**, $(\mu\text{-H})\text{Os}_3(\text{CO})_{10}$ ($\mu\text{-NC(H)CF}_3$) and **5**, $(\mu\text{-H})\text{Os}_3(\text{CO})_{10}(\mu\text{-}\eta^2\text{-HNCCF}_3)$ at 25 °C, and 390 nm., with 1 ml of gas (CF_3CN).

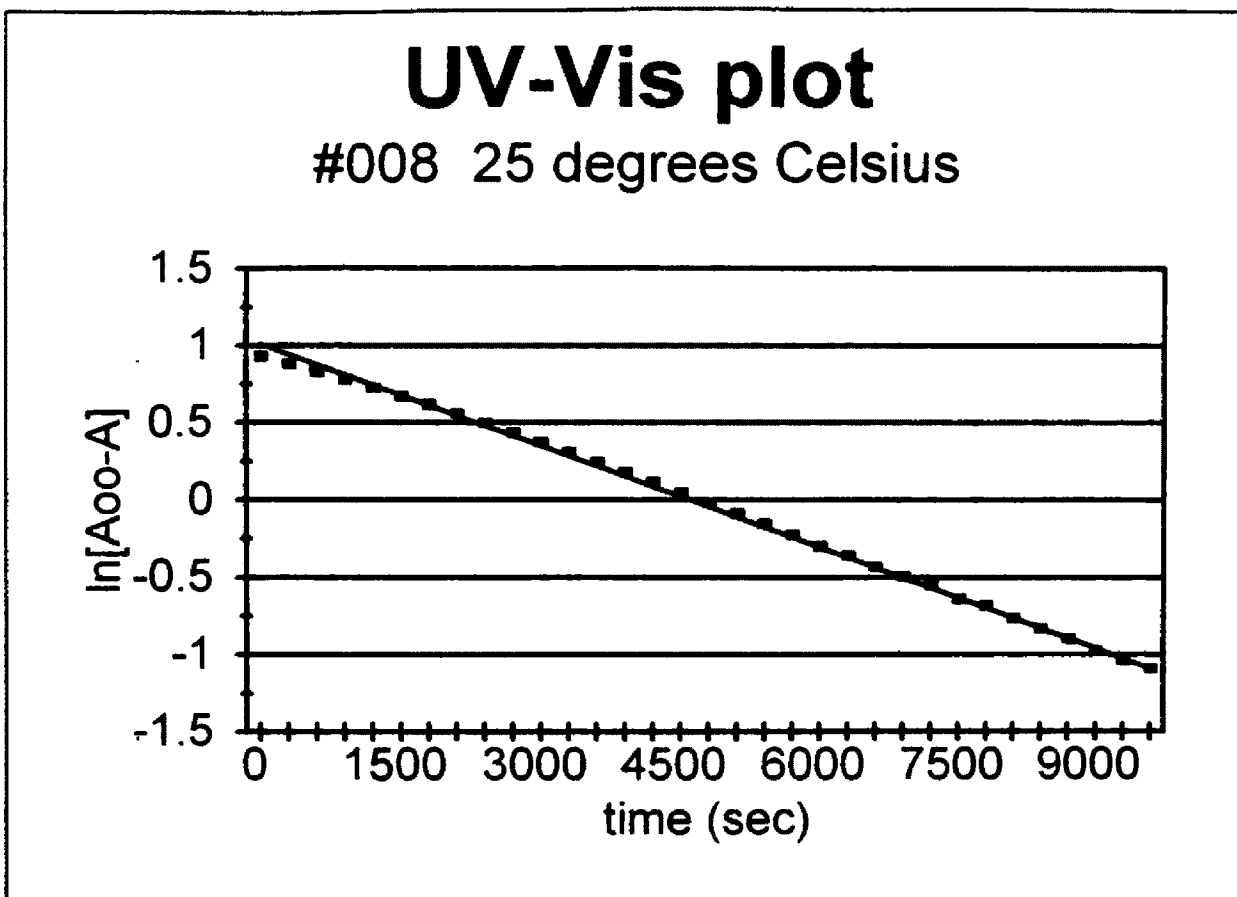


Figure 65: UV-Vis kinetic plot of the formation of **4**, $(\mu\text{-H})\text{Os}_3(\text{CO})_{10}$ ($\mu\text{-NC(H)CF}_3$) and **5**, $(\mu\text{-H})\text{Os}_3(\text{CO})_{10}(\mu\text{-}\eta^2\text{-HNCCF}_3)$ at 25 °C, and 392 nm., with 6 ml of gas (CF_3CN).

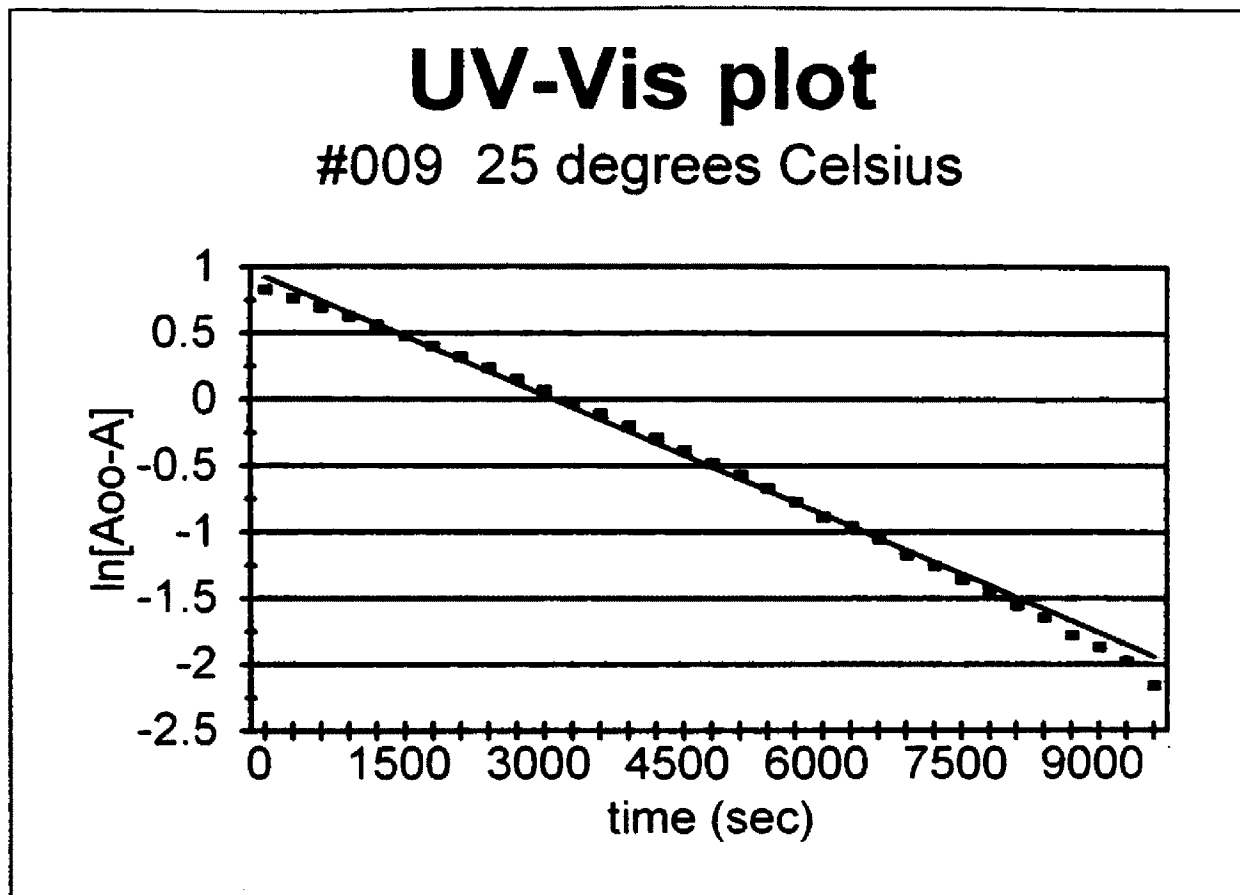


Figure 66: UV-Vis kinetic plot of the formation of 4, ($\mu\text{-H}$)Os₃(CO)₁₀ ($\mu\text{-NC(H)CF}_3$) and 5, ($\mu\text{-H}$)Os₃(CO)₁₀($\mu\text{-}\eta^2\text{-HNCCF}_3$) 25°C, and 392 nm., with 10 ml of gas (CF₃CN).

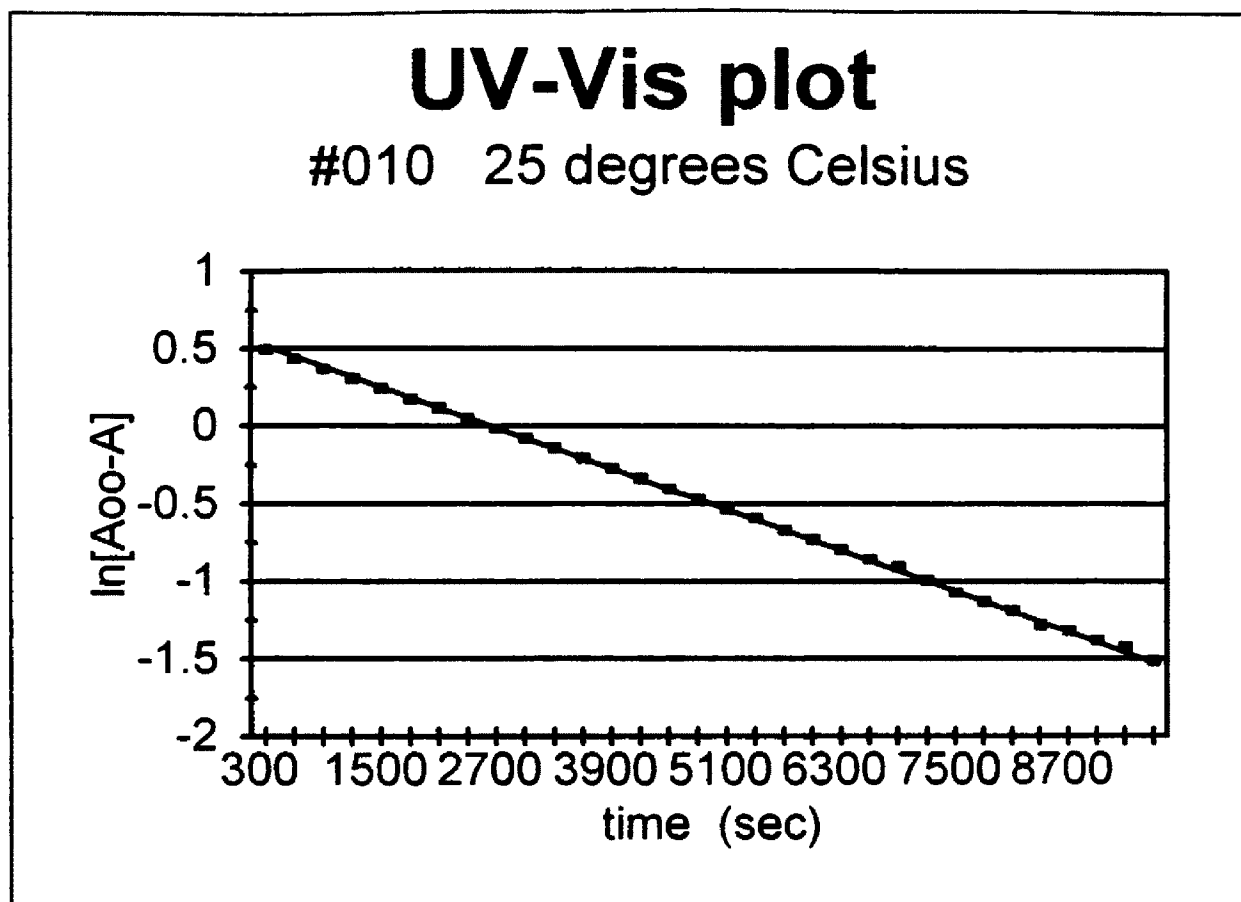


Figure 67: UV-Vis kinetic plot of the formation of **4**, $(\mu\text{-H})\text{Os}_3(\text{CO})_{10}$ ($\mu\text{-NC(H)CF}_3$) and **5**, $(\mu\text{-H})\text{Os}_3(\text{CO})_{10}(\mu\text{-}\eta^2\text{-HNCCF}_3)$ at 25°C, and 390 nm., with 6 ml of gas (CF_3CN).

References

1. Augustine, R.L. "Catalysis in Organic Reactions," Dekker, New York, 1985.
2. Pearce, R.; Patterson, W.R. "Catalysis and Chemical Processes," Halsted (Wiley), New York, 1981.
3. Moser, W.R.; Slocum, D.W. "Homogenous Transition Metal Catalyzed Reactions," ACS, Washington, 1992.
4. Nappa, M.J.; Santi, R.; Halprin, J. *Organometallics*, 1985, **4**, 34.
5. Edidin, R.T.; Norton, J.R. *J. Am. Chem. Soc.*, 1986, **108**, 948.
6. Jacobsen, E.N.; Bergman, R.G. *J. Am. Chem. Soc.*, 1984, **107**, 2023.
7. Jones, W.D.; Feher, F.J. *J. Am. Chem. Soc.*, 1985, **106**, 1650.
8. Collman, J.P.; Hegedus, L.S.; Norton, J.R.; Finke, R.G. "Principles and Applications of Organotransition Metal Chemistry", pp. 524-529 and references therein, University Science Books; Mill Valley, CA, 1987.
9. Shapley, J.R.; Calvert, R.B.; Schultz, A.J.; Williams, J.M.; Suib, S.L.; Stuckey, G.D. *J. Am. Chem. Soc.*, 1978, **100**, 6240.
10. Dutta, T.K.; Vites, J.C.; Jacobsen, G.B.; Fehlner, T.P. *Organometallics*, 1987, **6**, 842.
11. Keister, J.B.; Bower, D.K. *Organometallics*, 1990, **9**, 2321.
12. Carr, N.; Dunn, B.J.; Orpen, A.G.; Spencer, J.L. *J. Chem. Soc., Chem. Commun.*, 1988, **14**, 926.
13. Bulluck, R.M.; Headford, C.E.L.; Hennesy, K.M.; Kegley, S.E.; Norton, J.R. *J. Am. Chem. Soc.*, 1989, **111**, 3897.
14. Parkin, G.; Bercaw, J.E. *Organometallics*, 1989, **8**, 1172.
15. Muetterties, E.L. *Pure Appl. Chem.* 1982, **54**, 83.
16. Adams, R.D.; Golembeski, N.M. *J. Am. Chem. Soc.*, 1979, **101**, 2580.
17. Jones, W.D.; Feher, F.J. *Acc. Chem. Res.*, 1989, **22**, 91.
18. Brookhart, M.; Green, M.L.H.; Pardy, R.B.A. *J. Chem. Soc., Chem. Commun.*, 1983, **12**, 691.
19. Schmidt, G.F.; Brookhart, M. *J. Am. Chem. Soc.*, 1985, **107**, 1443.

20. Cracknell, R.B.; Orpen, A.G.; Spencer, J.L. *J. Chem. Soc., Chem. Commun.*, 1986, 1005.
21. Simpson, R.D.; Bergmann, R.G. *Organometallics*, 1993, **12**, 781.
22. Westheimer, F.H. *Chem. Revs.*, 1961, **61**, 265.
23. Bell, R.P. *Chem. Soc. Rev.*, 1974, **3**, 513.
24. Wiberg, K.B. *Chem. Revs.*, 1955, **55**, 713.
25. Melander, L.; Saunders, W.H. "Reaction Rates of Isotope Molecules", Wiley-Interscience: New York, 1980.
26. Rosenberg, E. *Polyhedron*, 1989, **8**, 383.
27. Bullock, R.M. in "Transition Metal Hydrides", Dedieu, A., Ed., VCH, New York, 1992.
28. Norton, J.R.; Sullivan, J.M.; Edidin, R.T. *J. Am. Chem. Soc.*, 1987, **109**, 3945.
29. Bigeleisen, J. *J. Chem. Phys.*, 1949, **17**, 675.
30. Bell, R.P. "The Proton in Chemistry", 2nd ed., pp.226-269, Cornell University Press: Ithaca NY, 1973.
31. Collman, J.P.; Finke, R.G.; Matlock, P.L.; Wahren, R.; Brauman, J.I. *J. Am. Chem. Soc.*, 1976, **98**, 4687.
32. Calvert, R.B.; Shapley, J.R.; Shultz, A.J.; Williams, J.M.; Suib, S.L.; Stucky, G.D. *J. Am. Chem. Soc.*, 1978, **100**, 6241.
33. Anslyn, E.V.; Green, M.; Nicola, G.; Rosenberg, E. *Organometallics*, 1991, **10**, 2600.
34. Wassink, B.; Thomas, M.J.; Wright, S.C.; Gillis, D.J.; Baird, M.C. *J. Am. Chem. Soc.* 1987, **109**, 1995.
35. Rosenberg, E.; Freeman, W.; Carlos, Z.; Hardcastle, K.I.; Yoo, Y.J.; Milone, L.; Gobetto, R. *J. Cluster Science*, 1992, **3**, 439.
36. Knight, J.; Mays, M.J.; *J. Chem. Soc. A.*, 1970, **5**, 711.
37. Cooke, C.G.; Mays, M.J.; *J. Organometallic Chem.*, 1974, **74**, 449.
38. Whitesides, T.H.; Neilen, J.P. *J. Am. Chem. Soc.*, 1975, **97**, 907.

39. Mayer, J.M.; Curtis, C.J.; Bercaw, J.E. *J. Am. Chem. Soc.*, 1983, **105**, 2651.
40. Rothwell, I.P. *Acc. Chem. Res.*, 1988, **21**, 153.
41. Fendrick, C.M.; Marks, T.J. *J. Am. Chem. Soc.*, 1986, **108**, 425.
42. Kwart, H. *Acc. Chem. Res.*, 1982, **15**, 401.
43. De La Vega, J.R. *Acc. Chem. Res.*, 1982, **15**, 185.
44. Bell, R.P. "The Tunnel Effect in Chemistry", Chapman and Hall: NY, 1980.
45. Jortner, J.; Pullman, B. "Tunneling", Reidel, Dorecht, Holland, 1986.
46. Heisenberg, W.K. *Z. Phys.*, 1927, **43**, 172.
47. Caldin, E.F. *Chem. Rev.*, 1969, **69**, 135.
48. Park, J.W.; Grubbs, R.H. personal communication.
49. Smith, K.T.; Tilset, M.; Kristjansdottir, S.S.; Norton, J.R. *Inorg. Chem.*, 1995, **34**, 6497.
50. Hodali, H.A.; Shriver, D.F.; Ammelung, C.A. *J. Am. Chem. Soc.*, 1978, **100**, 5240.
51. Keister, J.B. *J. Organomet. Chem.*, 1980, **190**, C36.
52. Rosenberg, E.; Pribich, D. *Organometallics*, 1988, **7**, 1741.
53. Adams, R.D.; Katahira, D.A.; Yang, L.W. *J. Organometallic Chem.*, 1981, **219**, 85.
54. Dawoodi, A.; Mays, M.J.; Raithby, P.R. *J. Organometallic Chem.*, 1981, **219**, 103.
55. Stevens, R.E.; Gladfelter, W.L. *J. Am. Chem. Soc.*, 1982, **104**, 6454.
56. Stevens, R.E.; Guettler, G.D.; Gladfelter, W.L. *Inorg. Chem.* 1990, **29**, 451.
57. Legzdins, P.; Nurse, C.R.; Rettig, S.J. *J. Amer. Chem. Soc.* 1983, **105**, 3727.
58. Noggle, J.H. "Physical Chemistry", Scott, Foresman and Company: Ill, 1989.
59. Bigeleisen, J. *J. Pure Appl. Chem.*, 1964, **8**, 217.
60. Eyring, H. *J. Chem. Phys.*, 1935, **3**, 107.
61. Eyring, H. *J. Chem. Phys.*, 1935, **3**, 492.
62. Laidler, K.J. "Chemical Kinetics", McGraw-Hill Book Company: NY, 1965.
63. Field, R.J. Personal Communication.

64. Rosenberg, E.; Espitia, D.; Hardcastle, K.I.; Kabir, S.E.; McPhillips, T.; Gobetto, R.; Milone, L.; Osella, D. *Organometallics*, 1993, **12**, 2390.
65. The μ_3 -CO in $\text{Ru}_3(\text{CO})_9(\mu_3\text{-CO})(\text{CC}(\text{OMe})\text{Me})$ is reported at 263 ppm (br); Sailor, M.J.; Brock, C.P.; Shriver, D.F. *J. Amer. Chem. Soc.* 1987, **109**, 6015.
66. Nevinger, L.R.; Keister, J.B. *Organometallics*, 1990, **9**, 1900.
67. Crabtree, R.H.; Siegbahn, P.E.M.; Eisenstein, O.; Rheingold, A.L.; Koetzle, T.F.; *Acc. Chem. Res.*, 1996, **29**, 348.
68. Kazarian, S.G.; Hamley, P.A.; Poliakoff, M. *J. Amer. Chem. Soc.*, 1993, **115**, 9069.
69. Kaesz, H.D.; Knox, S.A.R.; Koepke, J.W.; Saillant, R.B. *Chem. Commun.*, 1971, **10**, 477.
70. Knox, S.A.R.; Koepke, J.W.; Andrews, M.A.; Kaesz, H.D. *J. Am. Chem. Soc.*, 1975, **97**, 3942.
71. Martinsen, A.; Songstad, J. *Acta. Chem. Scand.*, 1977, **A31**, 645.